

<https://doi.org/10.14379/iodp.proc.382.106.2021>



## Contents

- 1 Background and objectives
- 1 Operations
- 4 Lithostratigraphy
- 11 Biostratigraphy
- 17 Paleomagnetism
- 27 Geochemistry
- 32 Physical properties
- 38 Stratigraphic correlation
- 41 Downhole measurements
- 42 Core-log-seismic integration
- 46 References

## Site U1537<sup>1</sup>

M.E. Weber, M.E. Raymo, V.L. Peck, T. Williams, L.H. Armbrecht, I. Bailey, S.A. Brachfeld, F.G. Cardillo, Z. Du, G. Fauth, M. García, A. Glüder, M.E. Guitard, M. Gutjahr, S.R. Hemming, I. Hernández-Almeida, F.S. Hoem, J.-H. Hwang, M. Iizuka, Y. Kato, B. Kenlee, Y.M. Martos, S. O'Connell, L.F. Pérez, B.T. Reilly, T.A. Ronge, O. Seki, L. Tauxe, S. Tripathi, J.P. Warnock, and X. Zheng<sup>2</sup>

Keywords: International Ocean Discovery Program, IODP, *JOIDES Resolution*, Expedition 382, Iceberg Alley and Subantarctic Ice and Ocean Dynamics, Site U1537, Dove Basin, Scotia Sea, Weddell Sea, sea ice, Antarctica, Antarctic Ice Sheet, sea level, ice-rafted debris, iceberg-rafted debris, iceberg, provenance, contourites, Weddell Sea Deep Water, Antarctic Circumpolar Current, Southern Hemisphere westerly winds, paleoceanography, paleoclimatology, mid-Pleistocene transition, Pliocene, interglacial climate, marine isotope stage, MIS 5, MIS 11

## Background and objectives

International Ocean Drilling Program (IODP) Site U1537 (proposed Site SCO-18) is located 265 km northwest of the South Orkney Islands at 59°6.65'S, 40°54.37'W in 3713 m of water. The site lies in the northeast part of Dove Basin in a ~1 km thick contourite drift and is situated at Shotpoint 4900 on Multichannel Seismic (MCS) Reflection Profile SCAN 2014/07 5 km west-northwest of Crossing Line SCAN 10/04. The objective at Site U1537 was to obtain a second sedimentary record in Dove Basin with a similar overall seismic structure (Seismic Units I–V) but with less stratigraphic disturbance than observed at Site U1536. Site U1537 was originally an alternate site but was selected for drilling because the upper ~150 m of the stratigraphy appeared to be uninterrupted by the thin slumped intervals observed at the other surveyed sites in Dove Basin (as seen in the seismic and echo sounder profiles). The goals were to reach Reflector b at ~350 meters below seafloor (mbsf) and to reconstruct the history of Pliocene–Pleistocene ice and ocean dynamics.

Sediments in the southern Scotia Sea are primarily deposited by contourite currents along the pathway of the Antarctic Circumpolar Current. Specifically in Dove Basin, contourite deposition is also assumed to be influenced by Weddell Sea Deep Water (WSDW) flowing from the south through bathymetric gaps around the South Orkney Plateau after exiting the Weddell Sea (Maldonado et al., 2003). The contourites at Site U1537 are lens shaped in seismic profiles, as thick as 800 m in the center of the trough, and thin toward the eastern edge.

Interpretation of Seismic Line 2004/07 identified Reflectors a–c (Pérez et al., 2017). In Dove Basin, three seismic lines indicate a basin-like structure with several small-scale ridges and continuous reflectors in the central to northern part of the basin. The seismic reflectors show overall parallel lamination with occasionally undulating structures that is likely indicative of minor synsedimentary downslope transport. This downslope movement is a fairly common feature in the basin, and none of the Expedition 382 proposed sites were able to avoid these disturbances completely.

At Site U1537, the main objective was to obtain a late Neogene record of ice and ocean dynamics from the center of “Iceberg Alley” in the more southerly of our two drilling areas in the Scotia Sea. Specific objectives included (1) the reconstruction of past variability in Antarctic Ice Sheet mass loss and the related sea level history, (2) a study of the water mass composition of the Drake Passage throughflow and WSDW inflow, and (3) a study of north–south shifts of the frontal systems in response to changing climate conditions, including changes in water mass properties, ocean temperature, and sea ice extent. An additional goal was to reconstruct changes in dust–climate couplings between Patagonia and Antarctica as well as related atmospheric circulation changes throughout the Pliocene–Pleistocene in a distal location relative to the main dust source, Patagonia.

## Operations

The 20 nmi transit north from Site U1536 to Site U1537 took 3.5 h. We arrived at Site U1537 at 0515 h local time on 26 April 2019.

<sup>1</sup> Weber, M.E., Raymo, M.E., Peck, V.L., Williams, T., Armbrecht, L.H., Bailey, I., Brachfeld, S.A., Cardillo, F.G., Du, Z., Fauth, G., García, M., Glüder, A., Guitard, M.E., Gutjahr, M., Hemming, S.R., Hernández-Almeida, I., Hoem, F.S., Hwang, J.-H., Iizuka, M., Kato, Y., Kenlee, B., Martos, Y.M., O'Connell, S., Pérez, L.F., Reilly, B.T., Ronge, T.A., Seki, O., Tauxe, L., Tripathi, S., Warnock, J.P., and Zheng, X., 2021. Site U1537. In Weber, M.E., Raymo, M.E., Peck, V.L., Williams, T., and the Expedition 382 Scientists, *Iceberg Alley and Subantarctic Ice and Ocean Dynamics*. Proceedings of the International Ocean Discovery Program, 382: College Station, TX (International Ocean Discovery Program). <https://doi.org/10.14379/iodp.proc.382.106.2021>

<sup>2</sup> Expedition 382 Scientists' affiliations.

MS 382-106: Published 20 May 2021

This work is distributed under the [Creative Commons Attribution 4.0 International](https://creativecommons.org/licenses/by/4.0/) (CC BY 4.0) license. 

Proposed Site SCO-18 was originally an alternate site but was selected as Site U1537 because the upper ~150 m of the stratigraphy appeared to be uninterrupted by thin slumped intervals compared to the other possible sites in the Dove Basin, as seen in the seismic and echo sounder profiles. We started to make up the bottom-hole assembly (BHA), but high heave and roll forced us to pause operations for ~7 h. Additionally, we had to move ~1 nmi northwest to allow an iceberg to pass over the site location. Operations resumed at 1430 h, and we lowered the drill string to the seafloor.

We started Hole U1537A at 0140 h on 27 April in relatively calm seas. The seafloor depth was 3712.9 meters below sea level (mbsl), as calculated from the mudline. Cores 382-U1537A-1H through 31F penetrated from the seafloor to 264.0 mbsf and recovered 268.9 m (102%) (Table T1). After Core 26H was difficult to pull out of the formation and had to be drilled over, we switched to the half-length

advanced piston corer (HLAPC) system for Core 27F at 240.0 mbsf. An iceberg moved into the red zone at 1830 h on 28 April, so we raised the drill string to 38 mbsf. At 2020 h after further encroachment of the iceberg, we ended Hole U1537A. Although we could not core at depth in Hole U1537A, we could take a mudline core because this operation does not require the drill string to be below the seafloor and the iceberg was not close enough to be within the termination zone.

Hole U1537B was started at 0010 h on 29 April and consisted of a single core taken for high-resolution interstitial water (IW) sampling. Core 382-U1537B-1H penetrated from the seafloor to 7.4 mbsf.

Hole U1537C was started at 0135 h on 29 April, and Cores 382-U1537C-1H and 2H penetrated from the seafloor to 15.3 mbsf and recovered 11.9 m (78%). After the Core 2H liner shattered and two

Table T1. Core summary, Site U1537. DRF = drilling depth below rig floor, DSF = drilling depth below seafloor, CSF = core depth below seafloor. NA = not applicable. H = advanced piston corer (APC), F = half-length APC (HLAPC). (Continued on next two pages.) [Download table in CSV format.](#)

Hole: U1537A		Hole U1537B	
Latitude: 59°6.6458'S	Longitude: 40°54.3725'W	Latitude: 59°6.6583'S	Longitude: 40°54.3516'W
Water depth (m): 3712.91	Date started (UTC): 0815 h; 26 April 2019	Water depth (m): 3712.01	Date started (UTC): 0015 h; 29 April 2019
Date finished (UTC): 0015 h; 29 April 2019	Time on hole (days): 2.67	Date finished (UTC): 0330 h; 29 April 2019	Time on hole (days): 0.14
Sea floor depth DRF (m): 3724	Sea floor depth est. method: APC calculated	Sea floor depth DRF (m): 3723.1	Sea floor depth est. method: APC calculated
Rig floor to sea level (m): 11.09	Penetration DSF (m): 264	Rig floor to sea level (m): 11.09	Penetration DSF (m): 7.4
Cored interval (m): 264	Recovered length (m): 268.86	Cored interval (m): 7.4	Recovered length (m): 7.4
Recovery (%): 101.84	Drilled interval (m): NA	Recovery (%): 100	Drilled interval (m): NA
Drilled interval (N): 0	Total cores (N): 31	Drilled interval (N): 0	Total cores (N): 1
APC cores (N): 26	HLAPC cores (N): 5	APC cores (N): 1	
<b>Hole U1537C</b>		<b>Hole U1537D</b>	
Latitude: 59°6.5197'S	Longitude: 40°54.0870'W	Latitude: 59°6.6597'S	Longitude: 40°54.3677'W
Water depth (m): 3713.61	Date started (UTC): 0330 h; 29 April 2019	Water depth (m): 3713.09	Date started (UTC): 0700 h; 29 April 2019
Date finished (UTC): 0700 h; 29 April 2019	Time on hole (days): 0.15	Date finished (UTC): 1430 h; 3 May 2019	Time on hole (days): 4.31
Sea floor depth DRF (m): 3724.7	Sea floor depth est. method: APC calculated	Sea floor depth DRF (m): 3724.2	Sea floor depth est. method: APC calculated
Rig floor to sea level (m): 11.09	Penetration DSF (m): 15.3	Rig floor to sea level (m): 11.11	Penetration DSF (m): 354.3
Cored interval (m): 15.3	Recovered length (m): 11.92	Cored interval (m): 354.3	Recovered length (m): 348.94
Recovery (%): 77.91	Drilled interval (m): NA	Recovery (%): 98.49	Drilled interval (m): NA
Drilled interval (N): 0	Total cores (N): 2	Drilled interval (N): 0	Total cores (N): 50
APC cores (N): 2		APC cores (N): 25	HLAPC cores (N): 25

Core	Date (2019)	Time on deck UTC (h)	Top depth drilled DSF (m)	Bottom depth drilled DSF (m)	Interval advanced (m)	Top depth cored CSF-A (m)	Bottom depth recovered CSF-A (m)	Recovered length (m)	Curated length (m)	Core recovery (%)	Sections (N)
382-U1537A-											
1H	27 Apr	0505	0.0	2.5	2.5	0.0	2.5	2.53	2.53	101	3
2H	27 Apr	0625	2.5	12.0	9.5	2.5	12.2	9.72	9.72	102	8
3H	27 Apr	0730	12.0	21.5	9.5	12.0	21.9	9.89	9.89	104	8
4H	27 Apr	0845	21.5	31.0	9.5	21.5	31.6	10.10	10.10	106	8
5H	27 Apr	1005	31.0	40.5	9.5	31.0	40.9	9.86	9.86	104	8
6H	27 Apr	1105	40.5	50.0	9.5	40.5	50.3	9.78	9.78	103	8
7H	27 Apr	1220	50.0	59.5	9.5	50.0	59.6	9.61	9.61	101	8

Table T1 (continued). (Continued next page.)

Core	Date (2019)	Time on deck UTC (h)	Top depth drilled DSF (m)	Bottom depth drilled DSF (m)	Interval advanced (m)	Top depth cored CSF-A (m)	Bottom depth recovered CSF-A (m)	Recovered length (m)	Curated length (m)	Core recovery (%)	Sections (N)
8H	27 Apr	1325	59.5	69.0	9.5	59.5	69.2	9.69	9.69	102	8
9H	27 Apr	1435	69.0	78.5	9.5	69.0	79.0	9.98	9.98	105	8
10H	27 Apr	1605	78.5	88.0	9.5	78.5	88.2	9.72	9.72	102	8
11H	27 Apr	1725	88.0	97.5	9.5	88.0	97.8	9.77	9.77	103	8
12H	27 Apr	1840	97.5	107.0	9.5	97.5	107.4	9.87	9.87	104	8
13H	27 Apr	2150	107.0	116.5	9.5	107.0	116.9	9.89	9.89	104	8
14H	27 Apr	2305	116.5	126.0	9.5	116.5	126.3	9.78	9.78	103	8
15H	28 Apr	0020	126.0	135.5	9.5	126.0	135.9	9.86	9.86	104	8
16H	28 Apr	0145	135.5	145.0	9.5	135.5	145.4	9.92	9.92	104	8
17H	28 Apr	0250	145.0	154.5	9.5	145.0	155.1	10.08	10.08	106	8
18H	28 Apr	0405	154.5	164.0	9.5	154.5	164.4	9.87	9.87	104	8
19H	28 Apr	0520	164.0	173.5	9.5	164.0	173.3	9.32	9.32	98	8
20H	28 Apr	0635	173.5	183.0	9.5	173.5	180.3	6.83	6.83	72	6
21H	28 Apr	0755	183.0	192.5	9.5	183.0	193.0	9.98	9.98	105	8
22H	28 Apr	0930	192.5	202.0	9.5	192.5	202.3	9.77	9.77	103	8
23H	28 Apr	1040	202.0	211.5	9.5	202.0	211.9	9.92	9.92	104	8
24H	28 Apr	1145	211.5	221.0	9.5	211.5	220.8	9.32	9.32	98	8
25H	28 Apr	1250	221.0	230.5	9.5	221.0	230.4	9.37	9.37	99	8
26H	28 Apr	1430	230.5	240.0	9.5	230.5	240.2	9.72	9.72	102	10
27F	28 Apr	1640	240.0	244.8	4.8	240.0	244.9	4.87	4.87	101	5
28F	28 Apr	1810	244.8	249.6	4.8	244.8	249.7	4.88	4.88	102	5
29F	28 Apr	1915	249.6	254.4	4.8	249.6	254.6	4.95	4.95	103	5
30F	28 Apr	2015	254.4	259.2	4.8	254.4	259.3	4.94	4.94	103	5
31F	28 Apr	2125	259.2	264.0	4.8	259.2	264.3	5.07	5.07	106	5
Hole U1537A totals:					264			268.86	268.86	101.84	
382-U1537B-											
1H	29 Apr	0335	0.0	7.4	7.4	0.0	7.4	7.40	7.40	100	6
Hole U1537B totals:					7.4			7.40	7.40	100	
382-U1537C-											
1H	29 Apr	0510	0.0	5.8	5.8	0.0	5.8	5.79	5.79	100	5
2H	29 Apr	0620	5.8	15.3	9.5	5.8	11.9	6.13	6.13	65	5
Hole U1537C totals:					15.3			11.92	11.92	77.91	
382-U1537D-											
1H	29 Apr	2315	0.0	6.3	6.3	0.0	6.3	6.30	6.30	100	6
2H	30 Apr	0035	6.3	15.8	9.5	6.3	15.6	9.25	9.25	97	8
3H	30 Apr	0145	15.8	25.3	9.5	15.8	25.4	9.58	9.58	101	8
4H	30 Apr	0305	25.3	34.8	9.5	25.3	34.7	9.42	9.42	99	8
5H	30 Apr	0415	34.8	44.3	9.5	34.8	44.6	9.80	9.80	103	8
6H	30 Apr	0610	44.3	53.8	9.5	44.3	54.1	9.78	9.78	103	8
7H	30 Apr	0715	53.8	63.3	9.5	53.8	63.7	9.85	9.85	104	8
8H	30 Apr	0820	63.3	72.8	9.5	63.3	72.8	9.53	9.53	100	8
9H	30 Apr	1035	72.8	82.3	9.5	72.8	81.9	9.05	9.05	95	7
10H	30 Apr	1255	82.3	91.8	9.5	82.3	91.1	8.81	8.81	93	8
11H	30 Apr	1430	91.8	101.3	9.5	91.8	99.9	8.10	8.10	85	7
12H	30 Apr	1650	101.3	110.8	9.5	101.3	110.7	9.40	9.40	99	8
13H	30 Apr	1845	110.8	120.3	9.5	110.8	120.1	9.30	9.30	98	8
14H	30 Apr	2000	120.3	129.8	9.5	120.3	130.1	9.84	9.84	104	8
15H	30 Apr	2125	129.8	139.3	9.5	129.8	137.2	7.43	7.43	78	6
16H	30 Apr	2250	139.3	148.8	9.5	139.3	148.1	8.79	8.79	93	11
17H	1 May	0005	148.8	158.3	9.5	148.8	158.6	9.82	9.82	103	8
18H	1 May	0120	158.3	167.8	9.5	158.3	167.8	9.45	9.45	99	8
19H	1 May	0235	167.8	177.3	9.5	167.8	177.5	9.65	9.65	102	8
20F	1 May	0355	177.3	182.1	4.8	177.3	182.3	5.00	5.00	104	5
21F	1 May	0505	182.1	186.9	4.8	182.1	186.4	4.28	4.28	89	4
22H	1 May	0625	186.9	196.4	9.5	186.9	196.9	9.99	9.99	105	8
23H	1 May	0800	196.4	205.9	9.5	196.4	204.8	8.42	8.42	89	7
24H	1 May	0920	205.9	215.4	9.5	205.9	215.8	9.89	9.89	104	8
25H	1 May	1040	215.4	224.9	9.5	215.4	225.1	9.68	9.68	102	8
26H	1 May	1250	224.9	234.4	9.5	224.9	232.6	7.72	7.72	81	9
27H	1 May	1420	234.4	243.9	9.5	234.4	243.7	9.28	9.28	98	8
28F	1 May	1535	243.9	248.7	4.8	243.9	248.6	4.69	4.69	98	4
29F	1 May	1635	248.7	253.5	4.8	248.7	253.7	5.04	5.04	105	5
30F	1 May	1745	253.5	258.3	4.8	253.5	258.5	4.98	4.98	104	5
31F	1 May	1850	258.3	263.1	4.8	258.3	263.4	5.06	5.06	105	5
32F	1 May	2020	263.1	267.9	4.8	263.1	268.1	4.98	4.98	104	5
33F	1 May	2140	267.9	272.7	4.8	267.9	272.8	4.92	4.92	103	5

Table T1 (continued).

Core	Date (2019)	Time on deck UTC (h)	Top depth drilled DSF (m)	Bottom depth drilled DSF (m)	Interval advanced (m)	Top depth cored CSF-A (m)	Bottom depth recovered CSF-A (m)	Recovered length (m)	Curated length (m)	Core recovery (%)	Sections (N)	
34F	1 May	2250	272.7	277.5	4.8	272.7	277.7	5.01	5.01	104	5	
35F	2 May	0045	277.5	282.3	4.8	277.5	282.5	4.95	4.95	103	5	
36F	2 May	0150	282.3	287.1	4.8	282.3	286.6	4.30	4.30	90	4	
37F	2 May	0255	287.1	291.9	4.8	287.1	291.8	4.73	4.73	99	5	
38F	2 May	0430	291.9	296.7	4.8	291.9	296.2	4.29	4.29	89	4	
39F	2 May	0535	296.7	301.5	4.8	296.7	301.7	5.00	5.00	104	5	
40F	2 May	0650	301.5	306.3	4.8	301.5	306.5	4.99	4.99	104	5	
41F	2 May	0800	306.3	311.1	4.8	306.3	311.4	5.09	5.09	106	5	
42F	2 May	0900	311.1	315.9	4.8	311.1	315.5	4.35	4.35	91	4	
43F	2 May	1015	315.9	320.7	4.8	315.9	320.9	5.03	5.03	105	5	
44F	2 May	1120	320.7	325.5	4.8	320.7	325.6	4.94	4.94	103	5	
45F	2 May	1240	325.5	330.3	4.8	325.5	330.6	5.07	5.07	106	5	
46F	2 May	1415	330.3	335.1	4.8	330.3	334.5	4.23	4.23	88	4	
47F	2 May	1525	335.1	339.9	4.8	335.1	340.1	5.00	5.00	104	5	
48F	2 May	1630	339.9	344.7	4.8	339.9	344.9	5.03	5.03	105	5	
49F	2 May	2015	344.7	349.5	4.8	344.7	349.7	4.96	4.96	103	5	
50F	2 May	2115	349.5	354.3	4.8	349.5	354.4	4.89	4.89	102	5	
					Hole U1537D totals:	354.3			348.94	348.94	98.49	
					Site U1537 totals:	641.0			637.12	637.12		

large icebergs entered the red zone at 0400 h, we decided to end Hole U1537C. We raised the drill string clear of the seafloor and moved aside in dynamic positioning mode to let the icebergs pass. By 1500 h, we were able to move back to the site location.

Hole U1537D was started at 1945 h on 29 April. Cores 382-U1537D-1H through 50F penetrated from the seafloor to 354.3 mbsf and recovered 349.0 m (99%). We took two HLAPC cores (20F and 21F) across a hard layer that was found in Hole U1537A at ~182 mbsf before returning to the full-length advanced piston corer (APC) system for Cores 22H–27H. Below 244 mbsf, the formation was too hard for full-length APC coring, so we used HLAPC coring from that point to the bottom of the hole. Icebergs were monitored on 30 April and 1 May, but none of them posed a hazard to operations. From 1345 to 1430 h on 2 May, we waited to monitor an iceberg that was at the edge of the red zone, but it turned away from the ship and we resumed coring. Because high winds and swell were forecast for 3 May, we decided to end Hole U1537D in the early evening of 2 May to leave enough time to raise the drill string to the ship and also to leave sufficient time for the coring and logging program at the next site (U1538) in the Pirie Basin region to the northwest. The bit cleared the seafloor at 2140 h and was raised to the ship by 1030 h on 3 May, which completed operations in Hole U1537D.

## Lithostratigraphy

Three lithostratigraphic units were identified based on sediment composition in smear slides and visual core description (Figure F1). Unit I contains three subunits. Most cores are relatively undisturbed. Drilling disturbance is most prevalent in the core tops, which commonly are soupy. Uparching and brecciated disturbance is rare. The dominant lithologies are diatom ooze (Figure F2) and silty clays (Figure F3).

## Unit descriptions

### Unit I

Intervals: 382-U1537A-1H-1 through 20H-CC; 382-U1537B-1H-1; 382-U1537C-1H-1 through 2H-CC; 382-U1537D-1H-1 through 20F-CC

Depths: Hole U1537A = 0–180.27 mbsf; Hole U1537B = 0–7.4 mbsf; Hole U1537C = 0–11.9 mbsf; Hole U1537D = 0–183.3 mbsf

Age: Holocene–mid-early Pleistocene

Unit I primarily consists of interbedded diatom ooze and silty clay. It is divided into three subunits because Cores 382-U1537A-1H through 9H are dominated by diatom ooze, Cores 9H–16H contain predominantly silty clay, and below Core 16H sediments again become rich in diatom ooze.

### Subunit IA

Intervals: 382-U1537A-1H-1 to 9H-7, 26 cm; 382-U1537B-1H-1; 382-U1537C-1H-1 through 2H-CC; 382-U1537D-1H-1 through 9H-4

Depths: Hole U1537A = 0–78.27; Hole U1537B = 0–7.4 mbsf; Hole U1537C = 0–11.9 mbsf; Hole U1537D = 0–78.80 mbsf

Lithostratigraphic Subunit IA consists of primarily diatom ooze with greenish gray to dark and very dark greenish gray (10Y 5/1 to 10Y 3/1 and 10Y 4/1) biosilica-rich silty clays. As estimated from smear slides, the terrigenous fraction is composed of >20% quartz with <10% feldspar and accessory opaque minerals. The biogenic fraction consists of biosilica (>50% diatoms and <10% spicules).

A few color bands (Figure F4), halo burrows, and pyrite-filled burrows (Figure F5) are found in the upper cores of this subunit. The transition between the lithologies is gradual.



Figure F1. Visual core description, Site U1537. CSF-A = core depth below seafloor, Method A. Pebble abundance >2 mm is semiquantitative visual assessment of concentration from 1 (no gravel or pebbles) to 5 (many gravel and pebble pieces) per core; pebble abundance >2 cm is semiquantitative count of >2 cm pebbles per core.

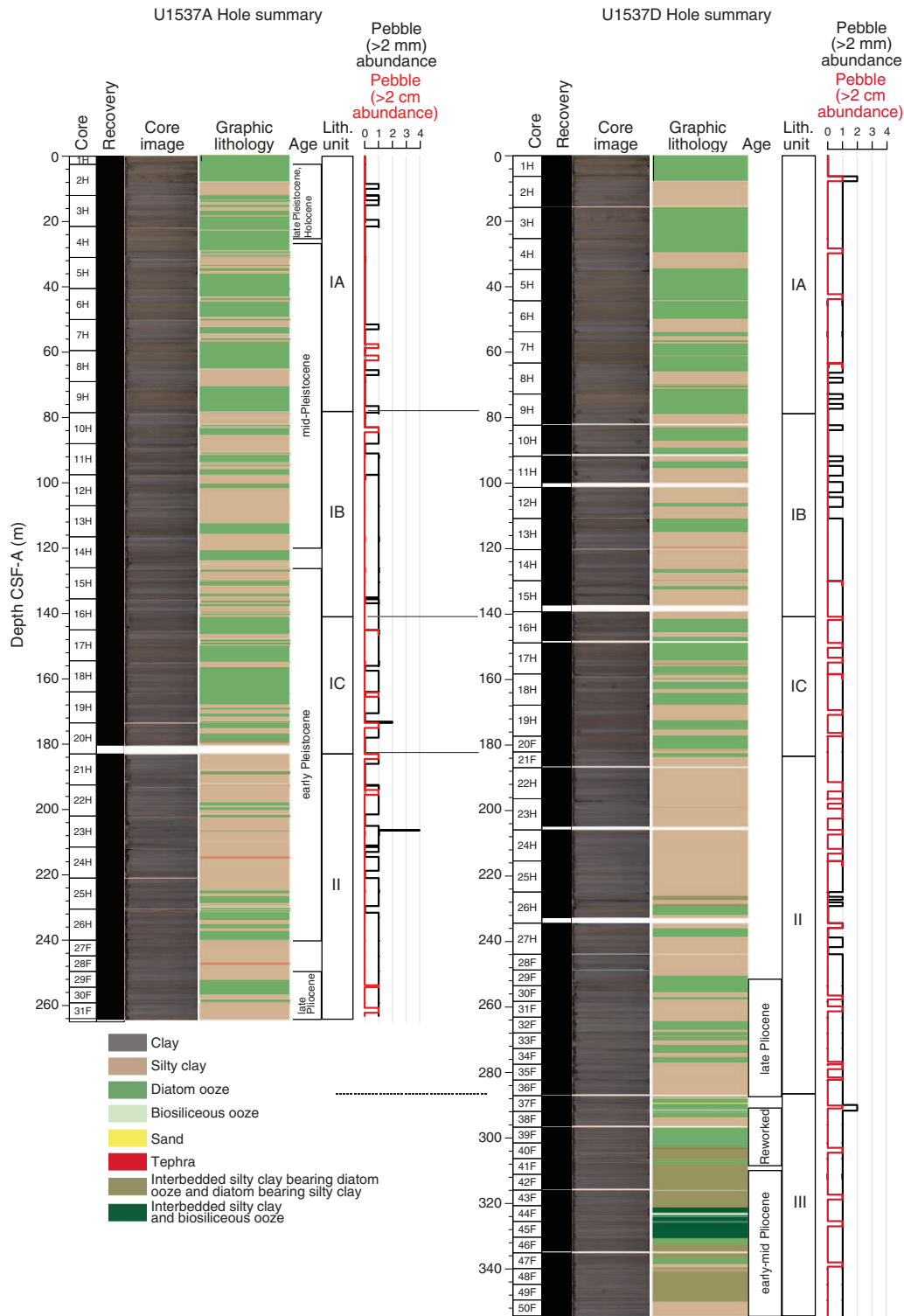


Figure F2. Diatom ooze (382-U1537D-7H-4, 26–56 cm).



Figure F3. Silty clay (382-U1537D-12H-5, 3–34 cm).



### Subunit IB

Intervals: 382-U1537A-9H-7, 26 cm, through 16H-4; 382-U1537D-9H-5 through 16H-1  
 Depths: Hole U1537A = 78.27–141.0 mbsf; Hole U1537D = 78.80–140.80 mbsf

Subunit IB contains interbedded greenish gray to dark greenish gray (10Y 5/1 to 10Y 3/1) silty clay and diatom ooze with biosilica-bearing silty clays. As estimated from smear slides, the terrigenous fraction is composed of >25% quartz. Feldspar and accessory

opaque minerals are <10%. The biogenic fraction consists of biosilica (>50% diatoms and <10% spicules).

Color banding, silt burrows, a few diatom mats, and pyritized burrows are found throughout this unit. Some minor glauconite layers were also seen in this unit. Sharp color boundaries were observed (Figure F6) in some of the cores. Few obvious dropstones are present in this subunit. Some of the cores show soft-sediment faults and exhibit slight drilling disturbance. A thin (~2–4 cm) carbonate layer with lithology is also present in this unit (Table T2).

Figure F4. Color banding (black arrows; incipient glauconite formation?) and burrow-rich layer (red arrow) (382-U1537A-7H-5, 37–60 cm).



#### Subunit IC

Intervals: 382-U1537A-16H-5 through 20H-CC; 382-U1537D-16H-2 through 20F-CC

Depths: Hole U1537A = 141.0–180.27; Hole U1537D = 140.80–183.30 mbsf

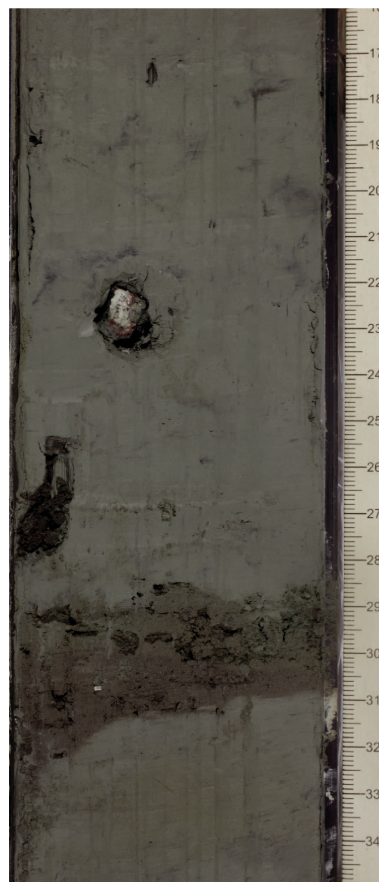
Subunit IC consists of dark greenish gray to very dark greenish gray (10Y 3/1 to 10Y 4/1) diatom ooze interbedded with silty clay. Most of the silty clays are biosilica rich. As estimated from smear slides, the terrigenous fraction is composed of >50% quartz, feldspar, and accessory opaque minerals. The biogenic fraction consists of biosilica (>50% diatoms and <10% spicules). Bioturbation is slight and best observed at color boundaries (Figure F7).

Some cores show drilling disturbance, such as uparching and soupy disturbance, at the core tops and at bioturbated contacts.

#### Unit II

Intervals: 382-U1537A-21H through 31F-CC; 382-U1537D-21F through 36F-CC

Figure F5. Granitic dropstone, pyrite-filled burrow, and pyrite-rich layer (382-U1537A-8H-5, 16–35 cm).



Depths: Hole U1537A = 183.0–264.2 mbsf; Hole U1537D = 183.1–286.53 mbsf

Age: mid-early Pleistocene–late Pliocene

Lithostratigraphic Unit II is dominated by interbedded biosilica-bearing silty clay, diatom-rich silty clay, and silty clay–rich diatom ooze. Sediments are dark greenish gray (5G 4/1 and 10Y 4/1). Quartz and feldspar are the dominant minerals of the terrigenous fraction.

Smear slide analyses also show rare to common occurrence of accessory minerals such as mica, amphiboles, glauconite, and opaques (probably pyrite). Boundaries between biosilica-bearing silty clay and silty clay diatom ooze are both abrupt and gradational (Figure F8). Very slight bioturbation is present throughout this unit and includes silt-filled burrows, pyrite clasts, and few pyritized burrows (Figure F9). Thin (2–4 cm) carbonate layers are also present in this unit. Some of the cores show coring-induced soft-sediment faults (Figure F10).

#### Unit III

Interval: 382-U1537D-37F-1 through 50F-CC

Depth: 287.1–354.34 mbsf

Age: late Pliocene–mid-early Pliocene

Lithostratigraphic Unit III is dominated by interbedded silty clay, diatom ooze, and biosiliceous ooze. Much of the sediment is folded, but between the folds the layers appear intact. Rare, thin



nannofossil ooze layers/laminations (Figure F11) were also observed in upper sections of this unit.

At more than 50%, quartz is the dominant mineral of the terrigenous fraction. Smear slide analyses also show common to abundant feldspar minerals in most core samples. Accessory minerals of mica, glauconite, and opaques (probably pyrite) form the minor component of the terrigenous fraction. A turbidite layer was observed in Section 382-U1537D-49F-3 (Figure F12). Very slight bioturbation is present throughout this unit and includes silt-filled burrows.

### X-radiographs

For Site U1537, X-ray images (5428 total) were taken from APC and HLAPC cores. The good quality of the images allows the classi-

fication of the background texture, presence of iceberg-rafted debris (IBRD), and other features such as pyritized burrows, carbonate or sandy layers, and the internal structure of slumps. For detailed studies, X-ray images from Hole U1537D have been visually analyzed.

The X-ray images of the two dominant lithologies (diatom ooze and silty clay) are similar to those from Site U1536, showing changes with depth in the background texture deeper in the hole (e.g., below Core 382-U1537D-9H [~80 mbsf]; Figure F13A, F13B). The appearance of diatom ooze changes from spotty to patchy, and silty clay changes from banded to homogeneous with intervals of millimeter- to centimeter-scale lamination. Interbedded sandy layers were identified in Cores 34F and 36F (Figure F13C).

IBRD occurs in variable concentrations along the entire sediment record but appears higher in distinct levels (Figure F13D). At

Figure F6. Sharp color boundary between varieties of silty clay (382-U1537A-12H-3, 126–144 cm).



Figure F7. Bioturbated contact (382-U1537D-19H-4, 25–42 cm).



Table T2. Carbonate layers with lithology, Site U1537. [Download table in CSV format.](#)

Hole, core, section, interval (cm)	Top depth (mbsf)	Bottom depth (mbsf)	Comment	Lithology
382-				
U1537A-21H-3, 22–24	186.22	186.24	Carbonate-rich clast	Biosilica-bearing silty clay
U1537A-21H-3, 47–49	186.47	186.49	Carbonate-rich layer	Biosilica-bearing silty clay
U1537A-24H-2, 136–150	214.36	214.50	Carbonate-rich layer	Biosilica-bearing silty clay
U1537A-24H-3, 0–2	214.50	214.52	Carbonate-rich layer	Biosilica-bearing silty clay
U1537A-28F-2, 52–66	246.82	246.96	Carbonate-rich layer	Biosilica-rich silty clay
U1537D-13H-7, 23–29	119.60	119.66	Carbonate-rich layer	Diatom-rich silty clay
U1537D-11H-4, 60–94	96.82	97.16	Carbonate-rich layer	Biosilica-bearing silty clay
U1537D-17H-4, 120–127	154.50	154.57	Carbonate-rich layer	Diatom-rich silty clay

greater depths, isolated larger IBRD clasts (as long as 3 cm in diameter) were identified in the X-ray images. Carbonate layers appear as blurred, structureless intervals in Cores 382-U1537D-13H and 17H. Undisturbed horizontal pyritized levels occur as dark layers below Core 19H.

Various types of burrows were frequently observed in the X-ray images at Site U1537, particularly in the silty clay lithologies. Thin pyritized burrows are typically less than 1 mm wide and 1–3 cm long and display a range of shapes from straight to curly. They are very common in the uppermost part of the sediment record from the seafloor to Core 382-U1537D-37F but are rare in cores below 300 mbsf (Figure F13E). Wide pyritized burrows are less frequent and are typically 1–5 mm wide and several centimeters long (Figure F13F). They occur with varying frequency between Cores 11H and 35F. Another type of wide burrow appears as a white feature in the images in silty clay levels. They are 3–5 mm wide and several centimeters long and have slightly curved shapes (Figure F13G). White burrows occur only in Cores 2H–7H, 22H, and 34F.

Postsedimentary deformation is revealed in detail by the X-ray images. The most remarkable deformation can be seen starting in

Core 382-U1537D-37F and is shown by a variety of textures (including deformed laminated layers, deformed banded and spotty textures, and grainy and mixed textures) to the bottom of the hole. Levels of undisturbed homogeneous, patchy background texture occur interbedded with the disturbed features (Figure F13H). Drilling disturbances appear as fluidized or broken-looking background textures and are common at the top of the first section of many cores. Soft and brittle deformation is also present, along with fault-like structures that usually present consistent angles and lengths along the core (which suggests another type of coring disturbance).

## Summary

The dominant lithologies at Site U1537 are alternating intervals of interbedded diatom ooze and diatom-rich silty clay, diatom-rich/bearing silty clay, and biosiliceous ooze/biosilica-bearing silty clay. Rare, thin layers of nannofossils were also observed in the upper sections of Unit III. Pyrite and silt-filled burrow and pyrite clasts occur throughout all depths at this site. Rare, thin beds of diagenetic carbonate are also present at irregular intervals in all units. A representative interval of the main lithologies is shown in Figure F1.

Figure F8. Interbedded silty clay and diatom ooze (382-U1537A-21H-7, 11–27 cm).

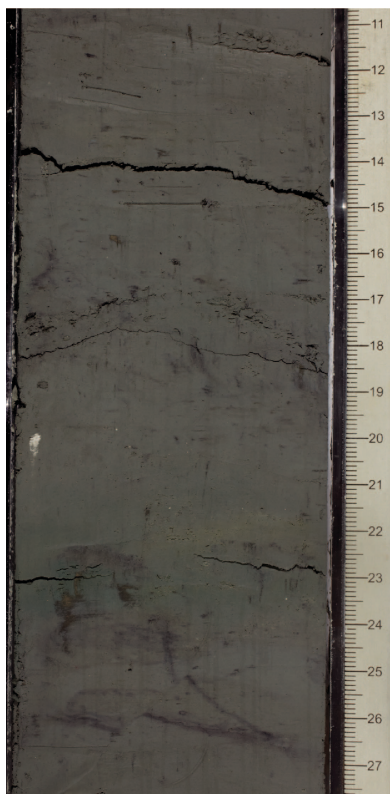


Figure F9. Pyrite nodule and pyritized burrows (black spots in the sediment) (382-U1537A-24H-5, 32–50 cm).

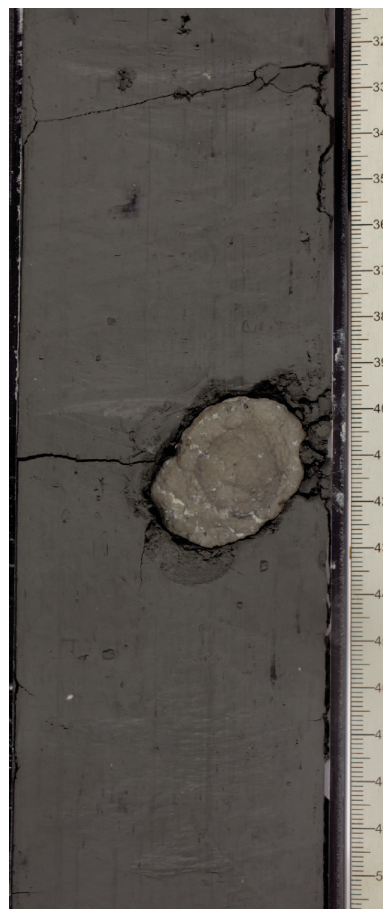




Figure F10. Coring-induced soft-sediment fault (382-U1537A-23H-4, 41–60).

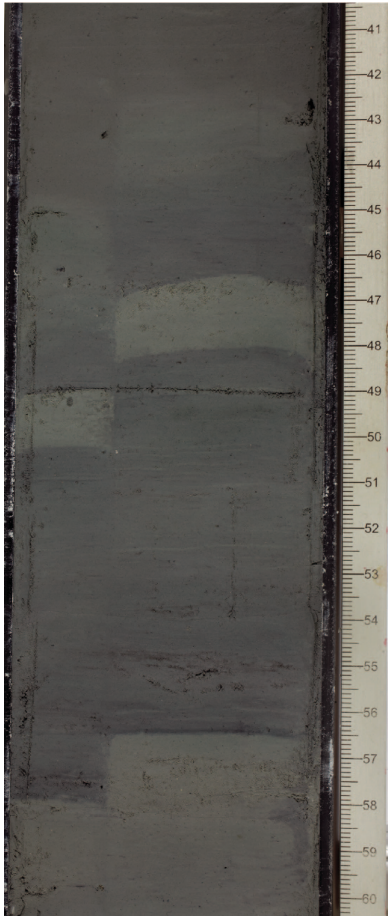


Figure F12. Turbidite (382-U1537D-49F-3, 101–130 cm).



Figure F11. Nannofossils (382-U1537D-41F-1).

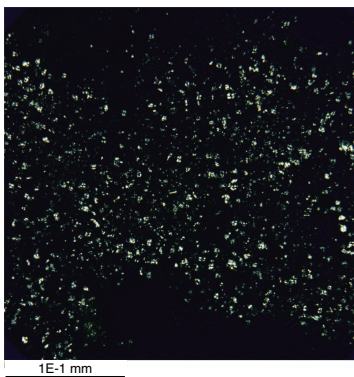
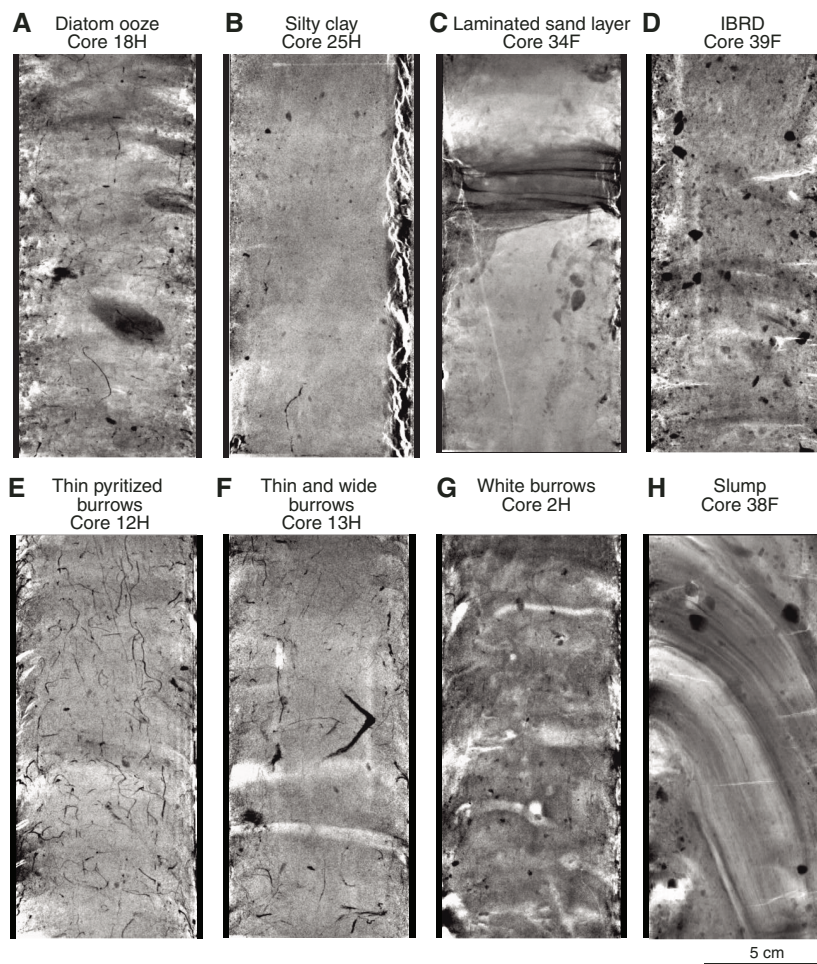




Figure F13. A–H. Examples of X-ray images showing most characteristic textures, Site U1537D. Dark colors correspond to higher density material.



## Biostratigraphy

Core catcher sediments primarily composed of diatomaceous oozes and fossiliferous muds were analyzed for diatoms, radiolarians, palynomorphs, and foraminifers. Selected additional samples were analyzed for diatoms and radiolarians. Preservation and abundance are variable throughout the analyzed intervals; however, diatoms, radiolarians, and palynomorphs were found in all analyzed sediments. Sediments range in age from Holocene to early Pliocene (Table T3). The specific age datums we used are given in Table T4. A biostratigraphically derived age-depth model is presented in Figure F14.

## Siliceous microfossils

### Diatoms

Diatoms are present in all analyzed samples. Specific species relative abundances, diatom overall abundance, and initial diatom preservation data are given in Table T5. Diatom dissolution increases downcore to Sample 382-U1537A-22H-CC. In deeper intervals, diatom dissolution is variable and not related to depth. Diatom fragmentation is variable throughout the analyzed samples. In general, fragmentation is more extreme than dissolution. Reworking of diatom fossils is persistent at Site U1537. Reworked Pliocene diatoms of the genus *Denticulopsis* were noted as high as Sample 4H-1, 75–76 cm, and continue to be present downcore. Reworked Miocene diatoms occur occasionally and are notably abundant in Sam-

ple 10H-CC. Reworked occurrences of the Pleistocene diatom *Rhizosolenia harwoodii* were noted as high as Sample 4H-2, 75–76 cm. Comparison with paleomagnetic reversal ages from Hole U1537D suggests that it is possible that reworking of early Pliocene diatoms into middle Pliocene age sediments has led to age estimates that are too old for Samples 382-U1537D-42F-CC to 50F-CC. However, the diatom communities found in these samples represent contemporaneous and not diachronous species groups. Furthermore, paleomagnetic data may be unreliable in the lowermost portions of Hole U1537D (see [Paleomagnetism](#)).

Samples 382-U1537A-1H-CC to 4H-3, 75–76 cm, contain an assemblage of extant Southern Ocean diatoms. This assemblage is dominated by the open-ocean-associated diatoms *Fragilariopsis kerguelensis* and *Thalassiosira lentiginosa*. Other diatoms found in this interval include *Actinocyclus actinochilus*, *Asteromphalus parvulus*, *Eucampia antarctica*, *Fragilariopsis curta*, *Fragilariopsis cylindrus*, *Fragilariopsis obliquecostata*, *Fragilariopsis rhombica*, *Fragilariopsis ritscheri*, *Fragilariopsis separanda*, *Fragilariopsis sublinearis*, *Porosira glacialis*, *Rhizosolenia antennata* var. *semispina*, *Shionodiscus gracilis*, *Shionodiscus oestrupii*, *Stellarima microtrias*, *Thalassiosira antarctica*, *Thalassiosira oliverana*, *Thalassiosira scotia*, and *Thalassiothrix antarctica*. This interval represents the Holocene and late Pleistocene.

Samples 382-U1537A-4H-4, 75–76 cm, to 14H-3, 50–51 cm, represent the late and middle Pleistocene. In addition to the dia-

Table T3. Summary of biostratigraphically assigned ages to sample ranges by microfossil group, Site U1537. [Download table in CSV format.](#)

Interval	Depth CSF-A (m)	Diatoms	Radiolarians	Palynomorphs
<b>382-U1537A-</b>				
1H-CC to 4H-3, 75–76 cm	2.48–25.25	Holocene, late Pleistocene	Holocene, late Pleistocene	
4H-4, 75–76 cm, to 14H-3, 50–51 cm	26.75–120.01	mid-Pleistocene	mid-Pleistocene	
14H-CC to 26H-CC	126.23–240.22	early Pleistocene	early Pleistocene	
28F-CC to 31F-CC	249.63–264.27	late Pliocene	early Pleistocene–late Pliocene	
<b>382-U1537D-</b>				
34F-CC to 37F-2, 75–75 cm	277.66–289.35	late Pliocene	late Pliocene	
37F-3, 74–75 cm, to 40F-CC	290.84–306.49	Reworked		
37F-3, 74–75 cm, to 42F-CC	290.84–315.45		Reworked	early Pleistocene–late Pliocene
41F-1, 75–76 cm, to 50F-CC	307.05–354.39	early-mid Pliocene		
41F-3, 75–76 cm, to 50F-CC	309.97–354.39		early-mid Pliocene	

Table T4. Biostratigraphic datums, Holes U1537A and U1537D. DIAT = diatom, RAD = radiolarian, PALY = palynomorph. LO = last occurrence, FO = first occurrence. (Continued on next page.) [Download table in CSV format.](#)

Type	Event	Published age (Ma)	Top core, section, interval (cm)	Bottom core, section, interval (cm)	Top depth (mbsf)	Bottom depth (mbsf)	Middepth (mbsf)
			382-U1537A-	382-U1537A-			
DIAT	LO <i>Rouxia leventerae</i>	0.14	4H-3, 75–76	4H-4, 75–76	25.26	26.76	26.01
DIAT	LO <i>Hemidiscus karstenii</i>	0.2	6H-1, 75–76	6H-CC	41.26	50.26	45.76
RAD	LO <i>Stylatractus univertus</i>	0.43	7H-CC	8H-CC	59.59	69.17	64.38
DIAT	LO <i>Rouxia constricta</i>	0.3	8H-CC	9H-CC	69.17	78.96	74.06
RAD	LO <i>Antarctissa cylindrica</i>	0.64	9H-CC	10H-CC	78.96	88.20	83.58
DIAT	LO <i>Actinocyclus ingens</i>	0.6	10H-CC	11H-1, 50–51	88.20	88.51	88.35
DIAT	LO <i>Rhizosolenia harwoodii</i>	0.6	10H-CC	11H-1, 50–51	88.20	88.51	88.35
DIAT	FO <i>Thalassiosira antarctica</i>	0.65	11H-2, 50–51	11H-3, 50–51	90.01	91.51	90.76
DIAT	FO <i>Porosira glacialis</i>	1.15	11H-3, 50–51	11H-CC	91.51	94.75	93.13
DIAT	LO <i>Thalassiosira elliptipora</i>	0.7	11H-CC	12H-CC	97.75	107.35	102.55
DIAT	LO <i>Thalassiosira fasciculata</i>	0.9	14H-1, 50–51	14H-3, 50–51	117.01	120.01	118.51
RAD	LO <i>Pterocanium trilobum</i>	0.86	14H-2, 120–121	14H-CC	120.25	126.26	123.25
DIAT	FO <i>Rouxia constricta</i>	1.4	15H-CC	16H-CC	135.84	145.40	140.62
DIAT	FO <i>Fragilariopsis rhombica</i>	1.4	16H-CC	17H-CC	145.40	155.06	150.23
DIAT	FO <i>Fragilariopsis separanda</i>	1.4	17H-CC	18H-CC	155.06	164.35	159.70
DIAT	LO <i>Fragilariopsis barronii</i>	1.3	19H-CC	20H-1, 50–51	173.30	174.01	173.65
DIAT	LO <i>Shionodiscus tetraoestrupii</i> var. <i>reimeri</i>	1.3	20H-2, 50–51	20H-3, 50–51	175.51	177.01	176.26
DIAT	LO <i>Rouxia antarctica</i>	1.5	20H-2, 50–51	20H-3, 50–51	175.51	177.01	176.26
DIAT	FO <i>Fragilariopsis obliquecostata</i>	1.7	21H-CC	22H-1, 50–51	192.96	193.01	192.98
RAD	LO <i>Cycladophora pliocenica</i>	1.81	21H-CC	22H-CC	192.96	193.01	192.98
RAD	FO <i>Phormospyris antarctica</i>	1.88	21H-CC	22H-CC	192.96	193.01	192.98
DIAT	LO <i>Fragilariopsis bohaty</i>	1.9	22H-5, 50–51	22H-6, 50–51	199.01	200.52	199.76
DIAT	LO <i>Thalassiosira kolbei</i>	1.9	22H-5, 50–51	22H-6, 50–51	199.01	200.52	199.76
DIAT	LO <i>Thalassiosira torokina</i>	1.9	22H-5, 50–51	22H-6, 50–51	199.01	200.52	199.76
DIAT	LO <i>Actinocyclus karstenii</i>	2.1	22H-5, 50–51	22H-6, 50–51	199.01	200.52	199.76
DIAT	LO <i>Thalassiosira inura</i>	1.8–2.0	22H-6, 50–51	22H-7, 50–51	200.52	202.02	201.27
DIAT	LO <i>Actinocyclus fasciculatus</i>	2.0	22H-6, 50–51	22H-7, 50–51	200.52	202.02	201.27
DIAT	LO <i>Thalassiosira vulnifica</i>	2.2	24H-CC	25H-CC	220.80	230.35	225.57
DIAT	FO <i>Fragilariopsis kerguelensis</i>	2.3	24H-CC	25H-CC	220.80	230.35	225.57
DIAT	FO <i>Shionodiscus tetraoestrupii</i> var. <i>reimeri</i>	2.3	24H-CC	25H-CC	220.80	230.35	225.57
DIAT	LO <i>Rouxia diploneides</i>	2.4	24H-CC	25H-CC	220.80	230.35	225.57
DIAT	FO <i>Shionodiscus gracilis</i>	2.3	25H-CC	26H-CC	230.35	240.20	235.27
DIAT	LO <i>Thalassiosira insigna</i>	2.6	25H-CC	26H-CC	230.35	240.20	235.27
DIAT	FO <i>Actinocyclus actinochilus</i>	2.75	25H-CC	26H-CC	230.35	240.20	235.27
DIAT	FO <i>Rouxia leventerae</i>	2.5	26H-CC	28F-CC	240.20	249.66	244.93
DIAT	FO <i>Actinocyclus fasciculatus</i>	2.7	26H-CC	28F-CC	240.20	249.66	244.93
DIAT	LO <i>Fragilariopsis weaveri</i>	2.7	26H-CC	28F-CC	240.20	249.66	244.93
DIAT	LO <i>Fragilariopsis interfrigidaria</i>	2.4	28F-CC	30F-CC	249.66	259.32	254.49
DIAT	LO <i>Thalassiosira complicata</i>	2.5	28F-CC	30F-CC	249.66	259.32	254.49
RAD	LO <i>Helotholus vema</i>	2.4	28F-CC	30F-CC	249.66	259.32	254.49
RAD	LO <i>Desmospyris spongiosa</i>	2.47	30F-CC	31F-CC	259.32	264.25	261.78
RAD	FO <i>Cycladophora davisiana</i>	2.61	30F-CC	31F-CC	259.32	264.25	261.78
			382-U1537D-	382-U1537D-			
PALY	LO <i>Operculodinium? erikianum</i>	2.34	34F-CC	36F-CC	277.685	286.575	282.13
DIAT	FO <i>Fragilariopsis bohaty</i>	3.1	34F-CC	36F-CC	277.69	286.58	282.13
DIAT	FO <i>Fragilariopsis weaveri</i>	3.5	34F-CC	36F-CC	277.69	286.58	282.13
DIAT	FO <i>Thalassiosira vulnifica</i>	3.2	36F-CC	37F-1, 75–75	286.58	287.85	287.21
RAD	LO <i>Larcopyle polyacantha titan</i>	3.48	38F-CC	40F-CC	296.17	306.47	301.32

Table T4 (continued).

Type	Event	Published age (Ma)	Top core, section, interval (cm)	Bottom core, section, interval (cm)	Top depth (mbsf)	Bottom depth (mbsf)	Middepth (mbsf)
DIAT	FO <i>Thalassiosira kolbei</i>	4.1	40F-CC	41F-1, 75-76	306.47	307.06	306.76
DIAT	LO <i>Fragilariopsis praeinterfrigidaria</i>	3.5	41F-1, 75-76	41F-2, 75-76	307.06	308.50	307.78
DIAT	FO <i>Rhizosolenia harwoodii</i>	3.6	41F-2, 75-76	41F-3, 75-76	308.50	309.98	309.24
RAD	LO <i>Lampromitra coronata</i>	3.72	41F-3, 75-76	41F-4, 75-76	309.98	311.07	310.52
DIAT	FO <i>Thalassiosira lentiginosa</i>	4.0	41F-4, 75-76	42F-CC	311.07	315.43	313.25
DIAT	LO <i>Fragilariopsis cylindrica</i>	4.3	41F-4, 75-76	42F-CC	311.07	315.43	313.25
DIAT	FO <i>Thalassiosira fasciculata</i>	4.5	41F-4, 75-76	42F-CC	311.07	315.43	313.25
DIAT	FO <i>Fragilariopsis interfrigidaria</i>	3.9	42F-CC	43F-CC	315.43	320.91	318.17
DIAT	LO <i>Fragilariopsis aurica</i>	4.2	43F-CC	44F-CC	320.91	325.62	323.26
DIAT	LO <i>Fragilariopsis praecurta</i>	4.2	43F-CC	44F-CC	320.91	325.62	323.26
DIAT	LO <i>Rouxia californica</i>	4.2	43F-CC	44F-CC	320.91	325.62	323.26
DIAT	LO <i>Denticulopsis delicata</i>	4.45	43F-CC	44F-CC	320.91	325.62	323.26
DIAT	FO <i>Fragilariopsis barronii</i>	4.4	48F-CC	50F-CC	344.91	354.37	349.64
DIAT	FO <i>Asteromphalus parvulus</i>	4.5	48F-CC	50F-CC	344.91	354.37	349.64

Figure F14. Biostratigraphic age-depth plot, Holes U1537A and U1537D. FO datums are plotted using the median depth between the upper sample where the fossil was observed and the lower sample where it was not observed (Table T4). LO datums are plotted using the median depth between the upper sample where a species was not seen and the lower sample where it was seen.

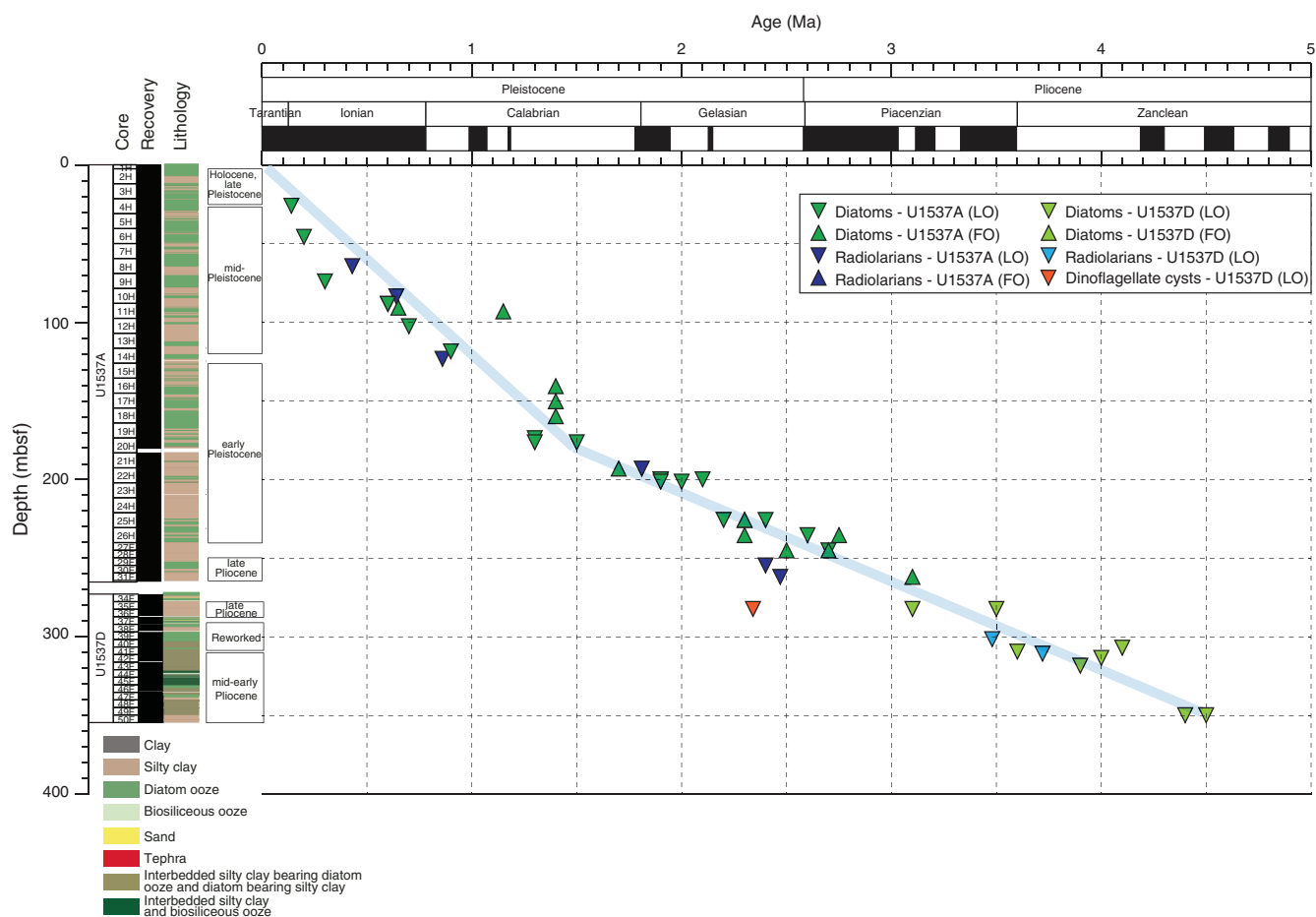


Table T5. Diatom occurrences, abundance, and preservation state, Site U1537. [Download table in CSV format.](#)

toms contained in the interval above, this interval contains the extinct species *Rouxia leventerae* (highest stratigraphic occurrence in Sample 4H-4, 75-76 cm), *Hemidiscus karstenii* (highest stratigraphic occurrence in Sample 6H-CC), and *Rouxia constricta* (high-

est stratigraphic occurrence in Sample 9H-CC). Although they were noted as reworked in the samples above, the last occurrence (LO) datums of *Actinocyclus ingens* and *R. harwoodii* (0.6 Ma) were recorded between Samples 10H-CC and 11H-1, 50-51 cm. These depths are considered the true LO intervals of these species based on their stratigraphic position relative to the first occurrence (FO) datum of *Thalassiosira antarctica* (0.65 Ma). The lowest strati-



graphic instance of *Thalassiosira antarctica* was recorded in Sample 11H-2, 50–51 cm. *Thalassiosira elliptipora* was identified in Samples 4H-3, 75–76 cm; 9H-CC; and 10H-CC. However, they are considered to be reworked because they occur above the FO of *Thalassiosira antarctica*. The true LO of *T. elliptipora* (0.7 Ma) was identified between Samples 11H-CC and 12H-CC. *Rouxia naviculoides* has its highest stratigraphic occurrence in Sample 14H-1, 50–51 cm. This sample also contains the highest stratigraphic occurrence of *Rouxia antarctica*. The LO of *Thalassiosira fasciculata* (0.9 Ma) was found between Samples 14H-1, 50–51 cm, and 14H-3, 50–51 cm. Finally, the lowest stratigraphic occurrence of *P. glacialis* was found in Sample 11H-3, 50–51 cm. Given the stratigraphic position relative to other species, this occurrence does not likely represent a true FO for this species.

Samples 382-U1537A-14H-CC to 26H-CC represent the early Pleistocene and contain many significant biostratigraphic events. The FO of *R. antarctica* (1.4 Ma) occurs between Samples 20H-2, 50–51 cm, and 20H-3, 50–51 cm. *F. rhombica* has an FO (1.4 Ma) between Samples 16H-CC and 17H-CC, and *F. separanda* has an FO (1.4 Ma) between Samples 17H-CC and 18H-CC. The LO of *Fragilariopsis barronii* (1.3 Ma) occurs between Samples 19H-CC and 20H-1, 50–51 cm. *F. obliquecostata* has an FO (1.7 Ma) between Samples 21H-CC and 22H-1, 50–51 cm. *Actinocyclus karstenii*, *Fragilariopsis bohattyi*, and *Thalassiosira kolbei* all have LO events between Samples 22H-5, 50–51 cm, and 22H-6, 50–51 cm. Although it was noted stratigraphically above this sample, the co-occurrence with *T. kolbei* implies an LO of *Thalassiosira torokina* in the same interval. *Actinocyclus fasciculatus* occurs only in Samples 22H-7, 50–51 cm, to 26H-CC. Similarly, *Shionodiscus tetraoestrupii* var. *reimeri* is exclusive to this early Pleistocene section, occurring in Samples 20H-3, 50–51 cm, to 24H-CC. The FO of *F. kerguelensis* (2.3 Ma) was identified between Samples 24H-CC and 25H-CC. The LOs of *Rouxia diploneides* (2.4 Ma) and *Thalassiosira vulnifica* (2.2 Ma) are between Samples 24H-CC and 25H-CC. In addition, the FOs of *A. actinochilus* (2.75 Ma), *S. gracilis* (2.3 Ma), and *Thalassiosira insigna* (2.6 Ma) were recognized between Samples 25H-CC and 26H-CC. Finally, *R. leventerae* has an FO (2.5 Ma) at the base of this interval between Samples 26H-CC and 28F-CC.

The remaining samples in Hole U1537A (382-U1537A-28F-CC to 31F-CC) and all analyzed samples from Hole U1537D (382-U1537D-34F-CC to 50F-CC) represent the Pliocene. Samples 382-U1537A-28F-CC to 31F-CC and 382-U1537D-34F-CC to 41F-2, 75–76 cm, contain assemblages of late Pliocene age. Notably, Sample 382-U1537D-38F-CC contains only reworked Miocene diatoms. The surrounding interval (Samples 37F-1, 75–76 cm, to 41F-2, 75–76 cm) also contains a higher frequency of reworked Miocene and early Pliocene diatoms than was observed in other samples from this site. These diatoms are mainly Miocene, but early Pliocene species were also observed. The top of this interval is defined by the LO of *Fragilariopsis weaveri* between Samples 382-U1537A-26H-CC and 28F-CC; the FO of *F. weaveri* was identified between Samples 382-U1537D-34F-CC and 36F-CC. The LOs of *Fragilariopsis interfrigidaria* (2.4 Ma) and *Thalassiosira complicata* (2.5 Ma) were found between Samples 382-U1537A-28F-CC and 30F-CC. The FO of *F. bohattyi* (3.1 Ma) was identified between Samples 382-U1537D-34F-CC and 36F-CC, and the FO of *T. vulnifica* (3.2 Ma) was subsequently found between Samples 36F-CC and 37F-1, 75–75 cm. *Fragilariopsis praeinterfrigidaria* has an LO (3.5 Ma) between Samples 41F-1, 75–75 cm, and 41F-2, 75–76 cm. The FO of *T. kolbei* (4.1 Ma) is between Samples 40F-CC and 41F-1, 75–76 cm. Sample 41F-

2, 75–76 cm, contains the lowest stratigraphic occurrences of *Fragilariopsis fossilis*, *T. elliptipora*, and *T. torokina*. The FO event of *R. harwoodii* (3.6 Ma) was recognized between Samples 41F-2, 75–76 cm, and 41F-3, 75–76 cm. Finally, the lowest stratigraphic occurrence of *F. curta* was found in Sample 382-U1537A-30F-CC. However, because the timing of the FO of this species is uncertain, we cannot use it to assign an age to this depth.

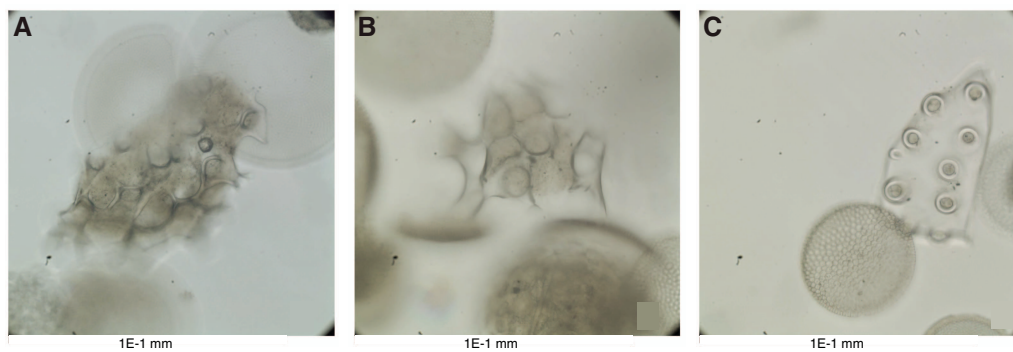
The final studied interval at Site U1537 (Samples 382-U1537D-41F-3, 75–76 cm, to 50F-CC) contains a middle Pliocene assemblage. The uppermost sample contains the lowest stratigraphic occurrence of *A. ingens*. The FOs of *T. fasciculata* (4.0 Ma) and *T. lentiginosa* (4.5 Ma) were observed between Samples 41F-4, 75–76 cm, and 42F-CC. The FO of *F. interfrigidaria* (3.9 Ma) is between Samples 42F-CC and 43F-CC. The LOs of *Denticulopsis delicata* (4.45 Ma), *Fragilariopsis aurica* (4.2 Ma), *Fragilariopsis praecurta* (4.2 Ma), and *Rouxia californica* (4.2 Ma) were observed between Samples 43F-CC and 44F-CC. The FO events of *F. barronii* (4.4 Ma) and *A. parvulus* (4.5 Ma) are between Samples 48F-CC and 50F-CC. *A. karstenii*, *D. delicata*, *Denticulopsis simonsenii*, *F. aurica*, *F. fossilis*, *F. praecurta*, *R. diploneides*, *Rouxia heteropolara*, *S. oestrupii*, *T. complicata*, *Thalassiosira inura*, and *Thalassiosira striata* all occur in the lowermost sample; therefore, true FO events cannot be determined for these taxa.

### Radiolarians

Radiolarian fauna in samples from Holes U1537A and U1537D are well to moderately well preserved, and abundance varies mostly between common and abundant (Table T6). Samples 382-U1537A-1H-CC to 3H-CC contain very few radiolarians, likely diluted by the high number of diatoms. Seven radiolarian biostratigraphic events were identified in Hole U1537A, and two were identified in Hole U1537D. The FO of *Stylatractus universus* (0.43 Ma) falls between Samples 382-U1537A-7H-CC and 8H-CC and marks the Omega/Psi Zone boundary. The LO of *Antarctissa cylindrica* (0.64 Ma) is constrained between Samples 9H-CC and 10H-CC. The LO of *Pterocanium trilobum* (0.86 Ma) occurs between Samples 14H-2, 120–121 cm, and 14H-CC and represents the top of the Chi Zone. The FO of *Cycladophora pliocenica* (1.81 Ma) and the LO of *Phormospyris antarctica* (1.87 Ma) indicate the transition from the Chi Zone to the Phi Zone and occur between Samples 21H-CC and 22H-CC. The LO of *Helotholus vema* (2.4 Ma) occurs between Samples 28F-CC and 30F-CC. Deeper samples to the bottom of Hole U1537A are assigned to the Upsilon Zone based on the almost constant occurrence of *H. vema* throughout that interval.

The LO of *Desmospyris spongiosa* (2.47 Ma) and the FO of *Cycladophora davisiana* (2.61 Ma) occur between Samples 382-U1537A-30F-CC and 31F-CC. Several Miocene species, such as *Acrosphaera murrayana*, *Acrosphaera vesuvius*, *Acrosphaera australis*, and *Actinomma golownini*, which are interpreted to be reworked, occur between Samples 382-U1537D-37F-3, 74–75 cm, and 41F-2, 75–77 cm (Figure F15). Despite containing older material, Sample 38F-CC also contains some typical Pliocene biostratigraphic markers, such as the LO of *Larcopele polyacantha titan* (3.48 Ma), and thus needs to be interpreted with caution. This interval will be subject to further analysis after the expedition. The LO of *Lampromitra coronata* (3.72 Ma) occurs between Samples 41F-3, 75–77 cm, and 41F-4, 75–77 cm.

Table T6. Radiolarian occurrences, preservation, and abundance, Site U1537. [Download table in CSV format.](#)

Figure F15. Miocene radiolarian species (between 382-U1537D-37F-3, 74–75 cm, and 41F-2, 75–77 cm). A, B. *Acrosphaera australis*. C. *Siphonosphaera vesuvius*.

## Palynology

A total of 23 core catcher samples from Holes U1537A ( $N = 15$ ) and U1537D ( $N = 8$ ) were processed and analyzed for palynological content (Table T7). Palynomorphs (dinoflagellate cysts [dinocysts], acritarchs, prasinophytes, pollen, spores, and copepod and fungi remains) were identified in all samples processed.

Dinocyst diversity is generally low with varying relative abundance. Assemblages normally consist of the heterotrophic proto-peridinioid genera *Brigantedinium* spp. and *Selenopemphix* spp., which are typically long ranging genera with little biostratigraphic significance in the time frame of the recovered material. The LO of *Operculodinium? eirikianum* in Sample 382-U1537D-38F-CC indicates an age older than 2.34 Ma, which is in agreement with the ages derived from the other microfossil groups. Dinocyst abundance is relatively high in Samples 382-U1537A-1H-CC to 17H-CC. Samples 23H-CC and 28F-CC have low dinocyst abundance. Samples 382-U1537D-34F-CC and 36F-CC and those below Sample 44F-CC are barren of dinocysts. Poorly preserved, thermally matured, and broken pieces of palynomorphs were also recorded throughout the samples, indicating reworking.

Terrestrial (sporomorphs and phytoclasts) components are relatively common in every sample processed, although most appear to be reworked. Well-preserved and less thermally matured *Nothofagidites* spp. and *Podocarpidites* spp. and other saccate (windblown) pollen were recorded sporadically throughout Site U1537. Prasinophyte algae were observed in low abundance in intervals in Samples 382-U1537A-5H-CC to 19H-CC and between Samples 382-U1537D-38F-CC and 44F-CC. Other palynofacies such as acritarchs, foraminifer test linings, copepod remains, and amorphous organic matter were also commonly recorded throughout Site U1537. Pyritized siliceous microfossils were observed in certain intervals, in particular below Sample 382-U1537A-25H-CC. Figures F16 and F17 show selected palynomorphs and dinocyst taxa.

## Marine sedimentary ancient DNA

### Ancient DNA

Samples for ancient DNA (aDNA) analysis were collected from Holes U1537A and U1537C. A single sample was collected from Hole U1537A, more specifically an organic plant-like fossil specimen that was found well preserved in clay material in Sample 382-U1537A-10H-CC. Limited sampling from Hole U1537C was undertaken to investigate spatial variability in aDNA between the two closely located Sites U1536 and U1537 (only 20 km apart) and followed the catwalk sampling methodology (see [Biostratigraphy](#) in the Expedition 382 methods chapter [Weber et al., 2021a]). One

Table T7. Palynomorph occurrences, preservation, and abundance, Site U1537. [Download table in CSV format.](#)

mudline sample (~12 mL) was taken, two sediment samples were collected from Section 382-U1537C-1H-1 (top and bottom of the section), and one sample each was taken from Sections 1H-2, 1H-3, and 2H-3 (bottom of each section). All samples were immediately stored at  $-80^{\circ}\text{C}$  and will be analyzed at the home laboratory, Australian Centre for Ancient DNA (ACAD), Adelaide (see [Biostratigraphy](#) in the Expedition 382 methods chapter [Weber et al., 2021a]).

### Contamination control

An air control sample (empty tube) and a drilling fluid control with perfluoromethyl decaline (PFMD) tracer (12 mL) were collected after aDNA sampling for Hole U1537C. Because chemical tracer (PFMD) concentrations were below the detection limit for most samples taken at previous Expedition 382 sites, the flow rate was doubled to 1 ppm at Site U1537 to test whether PFMD infusion was too low to be detectable or drilling fluid/PFMD did not reach the core. Inner and outer sediment samples for PFMD testing were collected at the same depths as aDNA samples for Hole U1537C. Samples were stored at  $4^{\circ}\text{C}$  and analyzed approximately 7 days after collection. PFMD concentrations were above the detection limit for one sample collected at the periphery of the core (Section 382-U1537C-2H-3; 0.4 ng/mL) and one sample from the core center (Section 1H-1; 0.4 ng/mL). Results from the aDNA sample collected at the same depth as the latter sample will be interpreted with caution.

## Summary

Diatom, radiolarian, foraminifer, and palynomorph biostratigraphic results are consistent for all samples from Holes U1537A and U1537D. These analyses showed 61 biostratigraphic events (Table T4). Based on these events, we estimate sedimentation rates of ~148 m/My between the seafloor and 180 mbsf followed by ~61 m/My from 180 mbsf to the base of the cored section (Figure F14). Estimated sedimentation rate changes may indicate variations in past ocean current strength, ice-rafted debris (IRD) delivery, taphonomic processes, and/or paleoproductivity. Considerable reworking was observed, especially between Samples 382-U1537D-37F-3, 74–75 cm, and 41F-1, 75–76 cm. Our analyses suggest that an extended Pleistocene record was recovered in Hole U1537A with a transition into Pliocene age sediment in the bottommost samples (below Sample 382-U1537A-25H-CC). In Hole U1537D, a further extension of the Pliocene was captured, and the bottommost sediments date back to about 4.45–4.6 Ma.

Figure F16. Palynomorphs, Hole U1537A. All scale bars = 20 µm. 1. *Lycopodium* spore (25H-CC). 2. Foraminiferal lining (21H-CC). 3. *Nothofagus* pollen (19H-CC). 4. *Tasmanites* (30F-CC). 5. *Brigantidium* spp. (30F-CC). 6. *Cyathidites* (trilete spore) (50F-CC). 7. *Selenopemphix antarctica* (25H-CC).

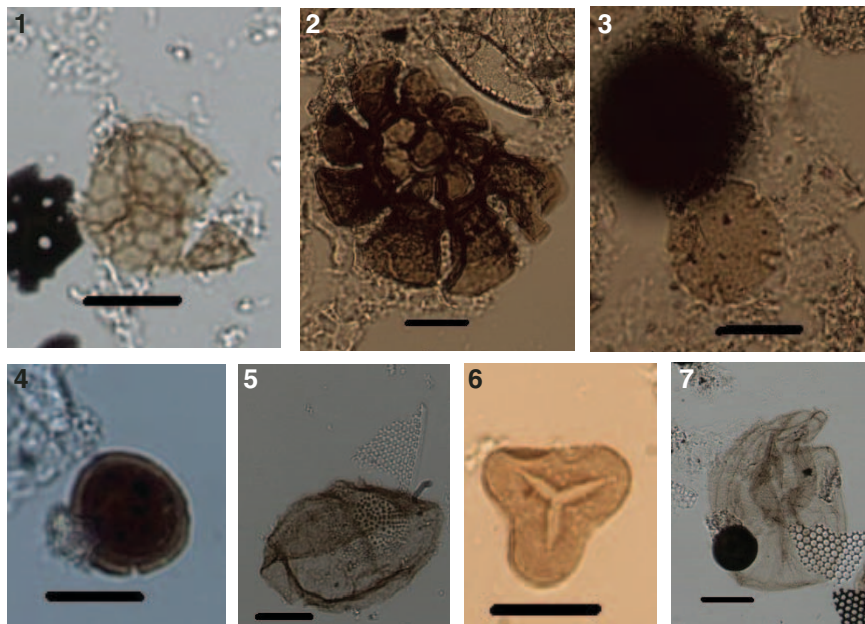
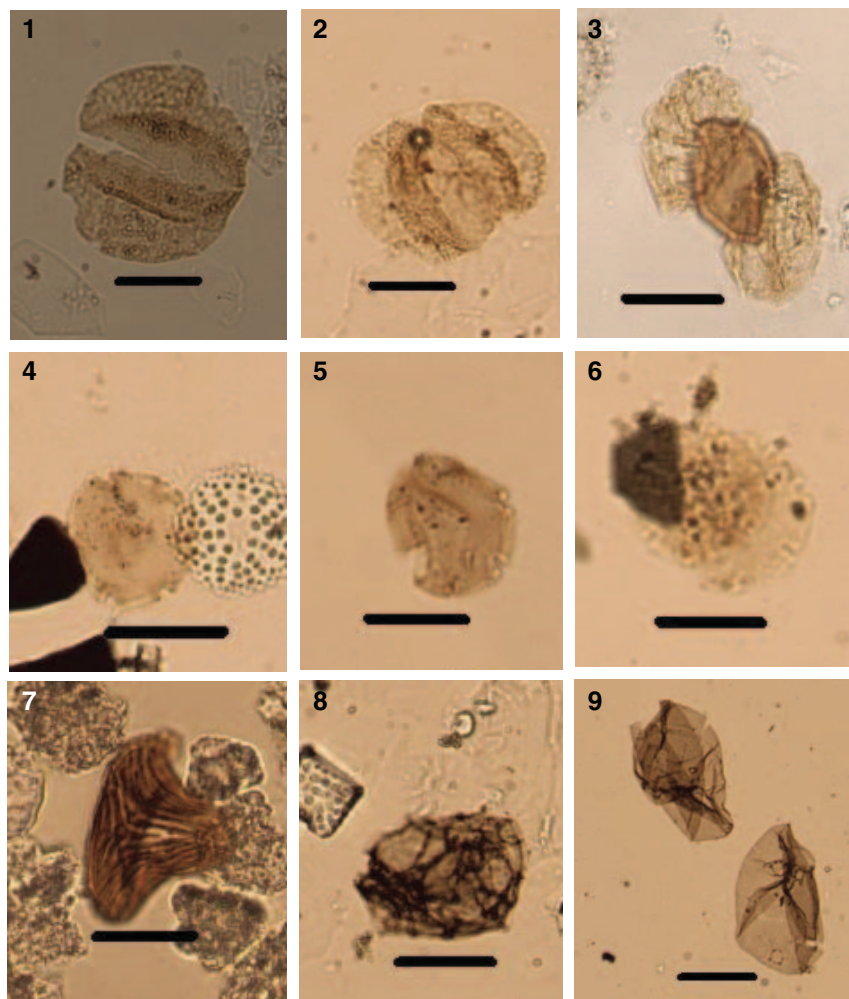


Figure F17. Palynomorphs, Hole U1537D. All scale bars = 20 µm. 1. Bisaccate pollen (38F-CC). 2. Bisaccate pollen (42F-CC). 3. Bisaccate pollen (44F-CC). 4–6. *Nothofagus* pollen (42F-CC). 7. *Cicatricosisporites australiensis* (reworked cretaceous) (44F-CC). 8. *Cymatiosphaera* sp. (40F-CC). 9. *Brigantidium* spp. (40F-CC).





## Paleomagnetism

Paleomagnetic measurements were made on 357 APC and 112 HLAPC core sections from Holes U1537A ( $N = 176$  APC/20 HLAPC), U1537B ( $N = 5$  APC), U1537C ( $N = 8$  APC), and U1537D ( $N = 168$  APC/92 HLAPC) to investigate the natural remanent magnetization (NRM). Orientation data were collected using the Ice-field MI-5 core orientation tool for Cores 382-U1537A-1H through 26H and 382-U1537D-1H through 18H (see [Paleomagnetism](#) in the Expedition 382 methods chapter [Weber et al., 2021a]). No archive-half measurements were made on core catcher samples. All archive-half measurements were made on the initial magnetization and the magnetization following peak alternating field (AF) demagnetization at 10 and 15 mT. Cores 382-U1537A-1H through 19H were also demagnetized using a 20 mT peak AF to assess what fields were needed to remove the drill string overprint. The 20 mT step was discontinued to keep up with core flow after observing the drill string overprint was generally removed by the 10 mT step.

A total of 228 discrete cube samples were taken from the working halves from Holes U1537A (all cores) and U1537D (Cores 382-U1537D-32F through 50F only). In general, we took one sample per section, avoiding visually disturbed or slumped intervals. We measured the NRMs of all cubes on the superconducting rock magnetometer (SRM) using the discrete sample tray, followed by stepwise demagnetization at peak AF steps of 5, 10, and 15 mT. A subset of 12 cubes selected to cover a range of depth intervals and lithologies was stepwise demagnetized up to 50 mT at 5 mT increments to further investigate the demagnetization behavior of the NRM. For this set of samples, an anhysteretic remanent magnetization (ARM) was imparted using a 100 mT peak AF and 0.05 mT direct current bias field. The ARMs were measured and stepwise demagnetized using the same steps as the NRM. For the NRM at 10 mT and subsequent steps, we demagnetized and measured the specimens in three orthogonal positions (top-away, top-right, and away-bottom settings in the SRM measurement program) and averaged the three measurements to insure data quality.

### Natural remanent magnetization

The data from the 15 mT step prior to any editing for Holes U1537A, U1537B, U1537C, and U1537D are shown as black dots in Figures [F18](#), [F19](#), [F20](#), and [F21](#), respectively. Cyan dots show the data after editing (see below), averaging core declinations, and adjusting each core to have a mean normal declination of  $90^\circ$  for purposes of plotting. We assess the reliability of polarity determinations in several ways:

- Examination of lithologic descriptions and X-ray images for disturbance,
- Stepwise AF demagnetization of discrete samples,
- Examination of histograms of inclinations (which should be bimodal at the expected geocentric axial dipole [GAD] inclinations at the site; see [Paleomagnetism](#) in the Expedition 382 methods chapter [Weber et al., 2021a]) and declinations (which should be uniformly distributed owing to presumably random orientations of core double lines), and
- Agreement of the interpreted magnetostratigraphy with available biostratigraphic constraints.

### Editing of archive-half measurements for coring disturbance

Editing of archive-half measurements was automated using Jupyter notebooks. These data were systematically filtered as follows:

- We deleted all measurements within 10 cm of the section ends to remove the edge effect inherent in all pass-through measurement systems such as the SRM.
- We deleted all measurements in the upper 80 cm of Section 1 of all APC and HLAPC cores because they are the most susceptible to the accumulation of fall-in material during coring. Additionally, the strong vertical drilling overprint in these intervals often appeared to be more difficult to remove.
- We deleted all data from intervals that were assigned the “high” drilling disturbance intensity code entered during core description (see [Lithostratigraphy](#)) to remove data in intervals affected by coring-induced disturbance such as fall-in and flow-in.

Tables [T8](#), [T9](#), [T10](#), and [T11](#) are adapted from the DESClogik tables used to perform the editing for disturbance noted in visual core description.

We next inspected core composite photographs and X-radiographs for evidence of coring or sedimentary disturbance as described in [Paleomagnetism](#) in the Expedition 382 methods chapter (Weber et al., 2021a). We removed data from two intervals composed of thick sand layers at the bases of turbidites, which give the false appearance of shallow inclinations. In addition to the X-ray disturbance textures previously described, we observed recumbent folds in the slumped sediment recovered in Cores 382-U1537D-37F through 50F (Figure [F22A](#), [F22B](#)). The slump also contains numerous intervals that we characterize as inclined layers. However, the dips of the layers are variable with values ranging from  $10^\circ$  to  $70^\circ$  (Figure [F22C–F22E](#)). For consistency with previous X-ray characterization, all layers that deviate from horizontal have been flagged as “inclined” and removed from the paleomagnetic data set. However, at a high-latitude site with a steep GAD inclination ( $-73.4^\circ$  at Site U1537), a low angle of deviation from horizontal bedding would still allow identification of polarity zones for in situ sediment, although this would compromise paleosecular variation studies. The polarity in some of the deleted intervals might still be resolved, although additional consultation is needed with the sedimentology and biostratigraphy groups to ensure these intervals represent original in situ sedimentation as opposed to emplacement of an allochthonous block of slump material. Tables [T12](#) and [T13](#) were used to edit data from Holes U1537A and U1537D based on X-ray images. Hole U1537B and U1537C data were not edited using X-ray images.

### Discrete sample data

We selected a set of 12 discrete samples for stepwise AF demagnetization experiments up to an AF of 50 mT. Representative examples of the behavior during demagnetization are shown in Figure [F23](#), including examples from high and low magnetic susceptibility (MS) intervals. Typical behavior for a normal polarity (inclination up) specimen is shown in Figure [F23A](#), and a reversed polarity is shown in Figure [F23B](#). An example of a poorly behaved specimen of indeterminate (but presumably reversed) polarity is shown in Figure [F23C](#). In the first two figures, we observed smooth decay to the origin and removal of a very minor drilling overprint in a positive downward direction, which is generally removed by the 10 mT step. In Figure [F23C](#), the magnetization bypasses the origin and no characteristic direction was found. Based on these data and observations from Site U1536, we subjected the remaining cube samples to demagnetization up to 15 mT. Discrete sample data measured after demagnetization at 15 mT are shown as red stars in Figures [F18](#), [F19](#), [F20](#), and [F21](#). Nearly all of these data agree well with the archive-half measurements. Note that the declinations of the discrete

Figure F18. Intensity of remanence, declination, and inclination of NRM at 15 mT AF demagnetization level, Hole U1537A. Horizontal dashed lines = section breaks, black dots = original (unedited) data, large cyan dots = edited and adjusted values as described in text, red stars = discrete samples, vertical dashed lines in inclination = GAD predicted values. (Continued on next page.)

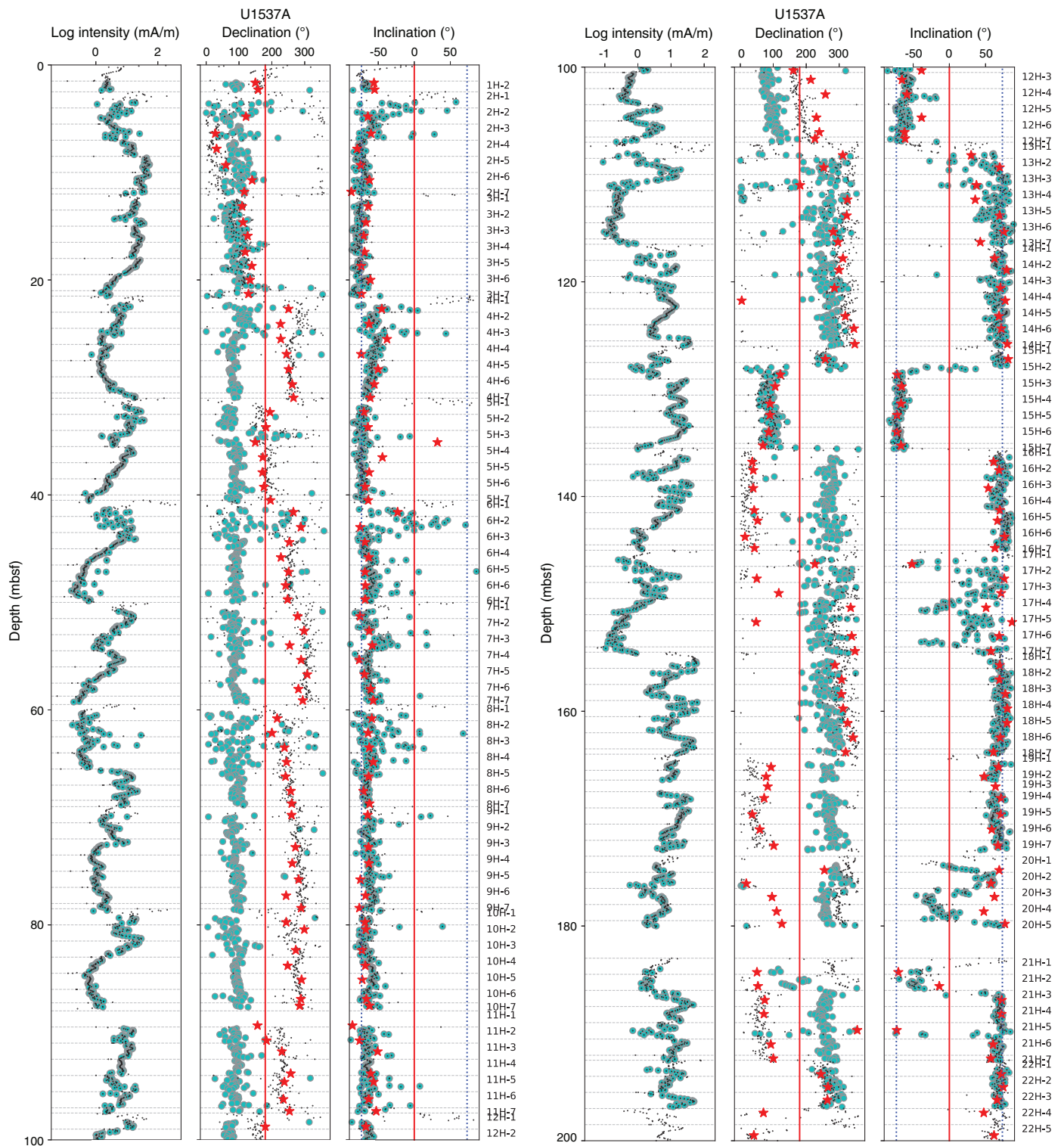
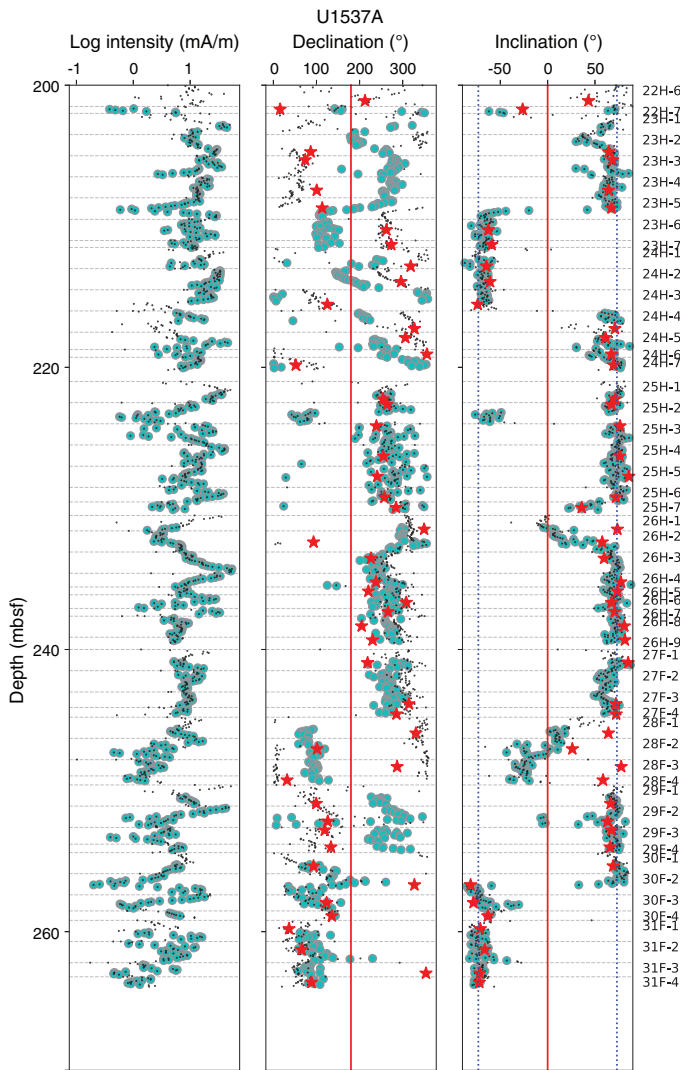


Figure F18 (continued).



samples were not adjusted, so they should be compared with the small black dots and not the adjusted cyan dots from the archive-half measurements.

After demagnetization and measurement to 50 mT (and subsequent demagnetization of the three axes at 100 mT), we imparted an ARM to the subset of 12 discrete samples and then AF demagnetized the ARMs at the same peak fields (Figure F24). Ratios of the ARM after demagnetization at 30 mT to the initial ARM (a proxy for the ARM coercivity) range from 0.28 to 0.49. There does not appear to be a systematic relationship between ARM coercivity and ARM intensity; the extremes in the range of ARM coercivity are found in the weaker half of the samples, and the stronger half of the samples fall mostly in the intermediate range around 0.4. Two weaker samples appeared to acquire a magnetization during demagnetization of the NRM (Figures F23C, F24A, F24E); however, they do not share similar ARM coercivities ( $ARM_{30mT}/ARM = 0.42$  and  $0.28$ ), suggesting different magnetic mineral assemblages. Although most samples appear consistent with detrital (titano)magnetite as the primary remanence carrier, postcruise work using multiple experiments in a more controlled environment will be needed to fully characterize the magnetic mineral assemblages.

Figure F19. Intensity of remanence, declination, and inclination of NRM at 15 mT AF demagnetization level, Hole U1537B. Horizontal dashed lines = section breaks, black dots = original (unedited) data, large cyan dots = edited and adjusted values as described in text, vertical dashed lines in inclination = GAD predicted values.

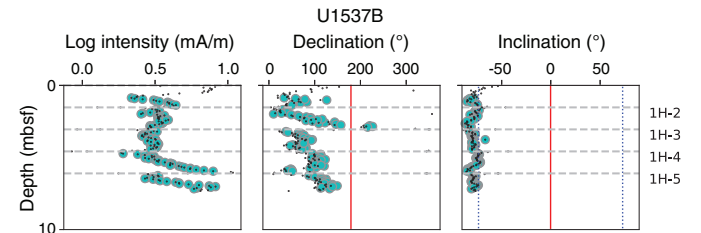
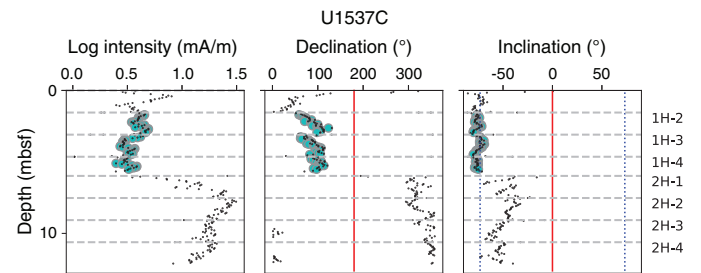


Figure F20. Intensity of remanence, declination, and inclination of NRM at 15 mT AF demagnetization level, Hole U1537C. Horizontal dashed lines = section breaks, black dots = original (unedited) data, large cyan dots = edited and adjusted values as described in text, vertical dashed lines in inclination = GAD predicted values.



### Distributions of inclinations and declinations

We plotted histograms of inclination values separated by coring type in Figure F25. Both coring types (APC and HLAPC) show two distinct groups with steep directions generally spanning  $\pm 45^\circ$ – $90^\circ$ . However, the inclination distribution for the HLAPC measurements includes a greater proportion of intermediate values than the APC measurements, perhaps due to greater coring deformation or the presence of slumped sediments (see [Lithostratigraphy](#)). The number of normal polarity observations (negative inclinations) is greater than the number of reversed observations (positive inclinations) in the APC cores, which is expected because these are the youngest cores and they are dominated by Brunhes age (normal) sediments. The older records sampled by the HLAPC system are more or less equally distributed between the two polarities.

Histograms and quantile-quantile plots for the declination data are shown in Figure F26. We noted a slight tendency for declinations to be preferentially distributed near the fiducial line (the double line inscribed along the working half of the core liner and whose azimuth defines the  $+X$  direction) of the cores at Site U1536, but a uniform distribution (as expected in unoriented cores) could not be rejected at the 95% confidence level. The same appears to be true at Site U1537. However, when considering the declinations before editing for sedimentary and coring disturbances, the declinations for at least the HLAPC cores are not uniformly distributed and, as shown by the blue symbols in Figure F26D, have subtly different behavior, leading to the ability to reject a uniform distribution at the 95% confidence level.

To explain the concentration of directions toward the fiducial line in the disturbed cores, we hypothesized that the drilling distur-



Figure F21. Intensity of remanence, declination, and inclination of NRM at 15 mT AF demagnetization level, Hole U1537D. Horizontal dashed lines = section breaks, black dots = original (unedited) data, large cyan dots = edited and adjusted values as described in text, red stars = discrete samples, vertical dashed lines in inclination = GAD predicted values. (Continued on next page.)

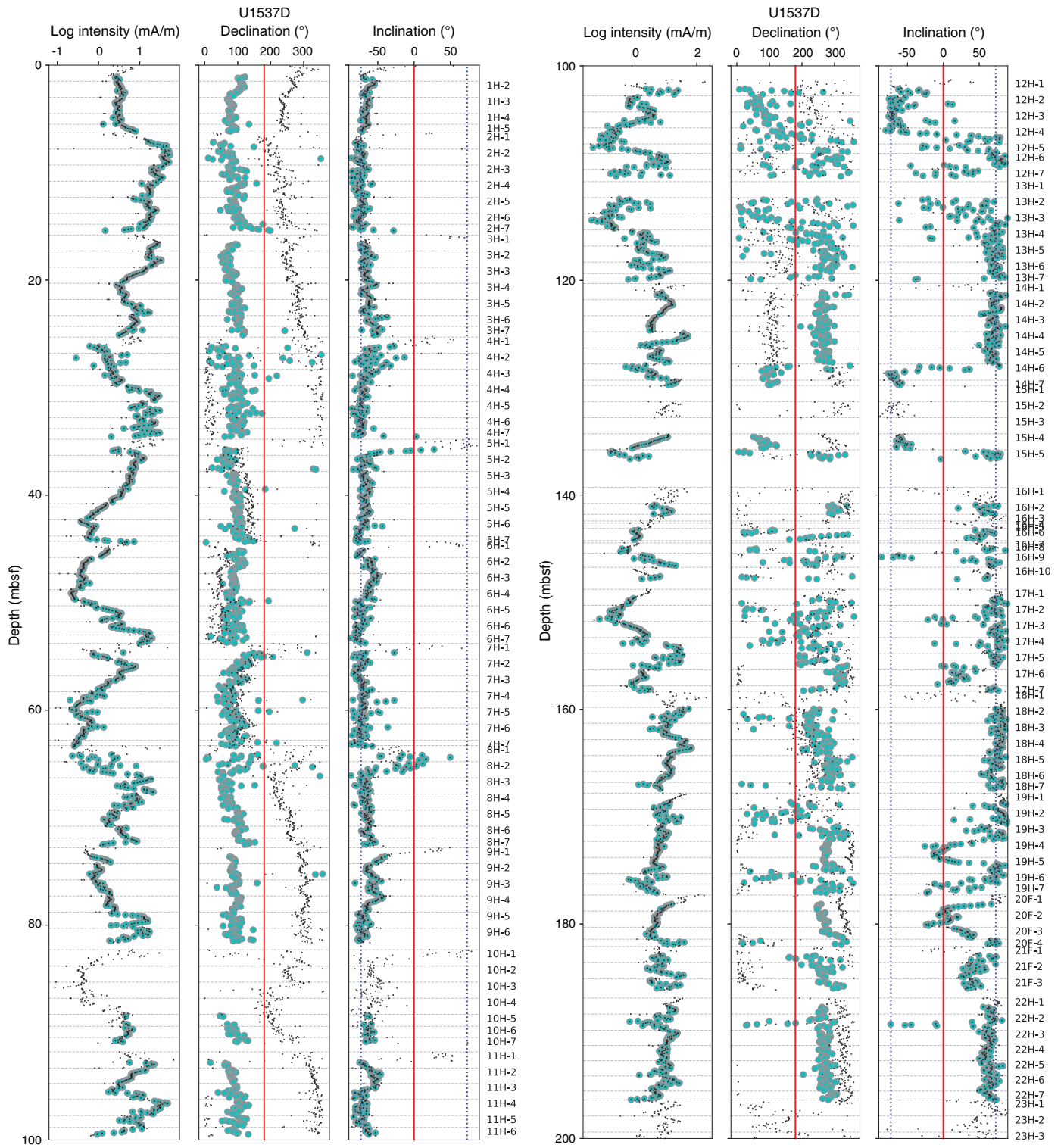
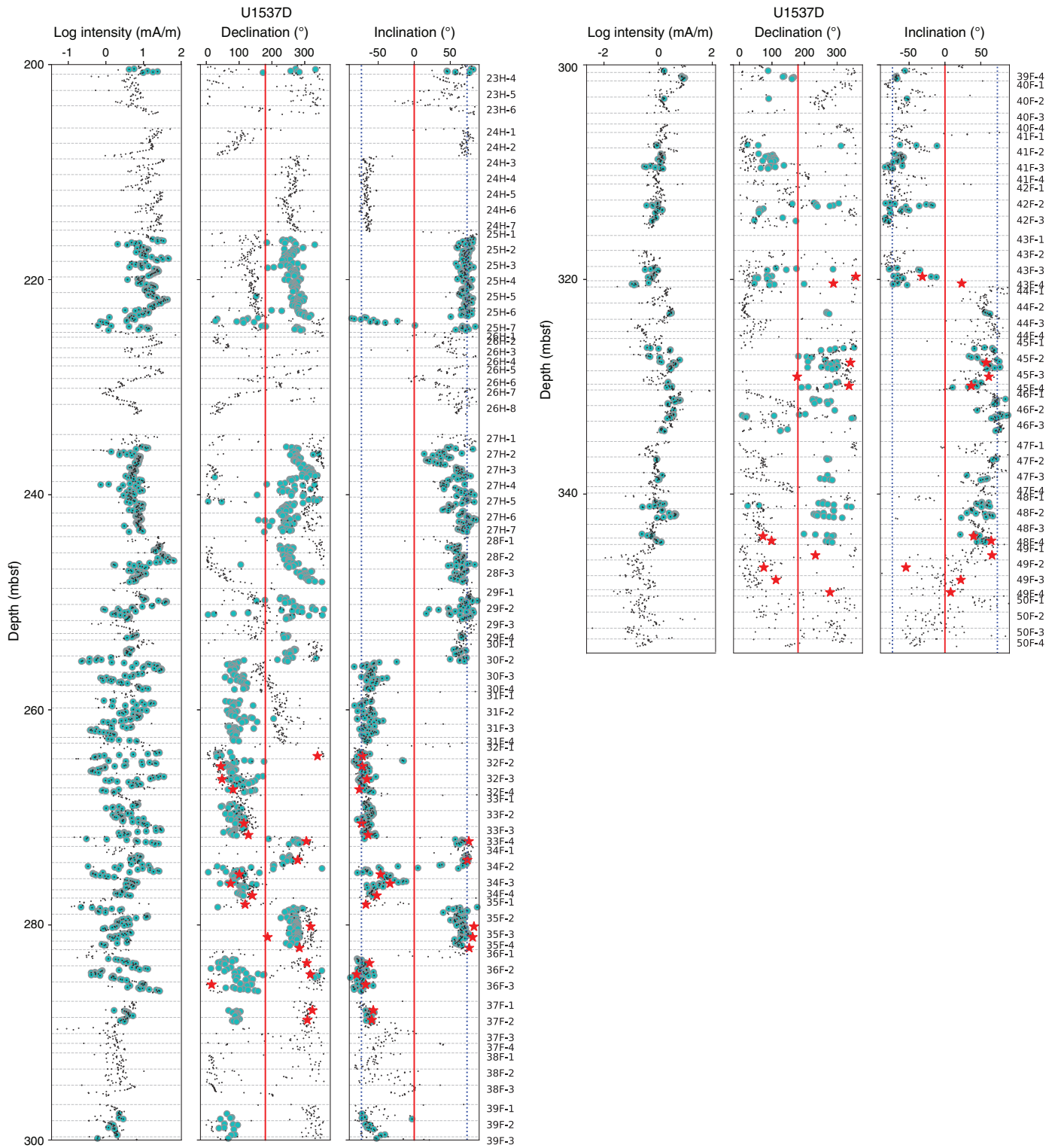


Figure F21 (continued).



bance described as “uparching” and noted in many cores could cause a bias in inclinations toward shallower directions and a declination bias toward the double line if the archive halves are measured. To test this, we generated a set of 100 field directions

Table T8. Intervals of high-intensity core disturbance as determined by visual inspection during core description, Hole U1537A. [Download table in CSV format.](#)

Table T9. Intervals of high-intensity core disturbance as determined by visual inspection during core description, Hole U1537B. [Download table in CSV format.](#)

Table T10. Intervals of high-intensity core disturbance as determined by visual inspection during core description, Hole U1537C. [Download table in CSV format.](#)

Table T11. Intervals of high-intensity core disturbance as determined by visual inspection during core description, Hole U1537D. [Download table in CSV format.](#)

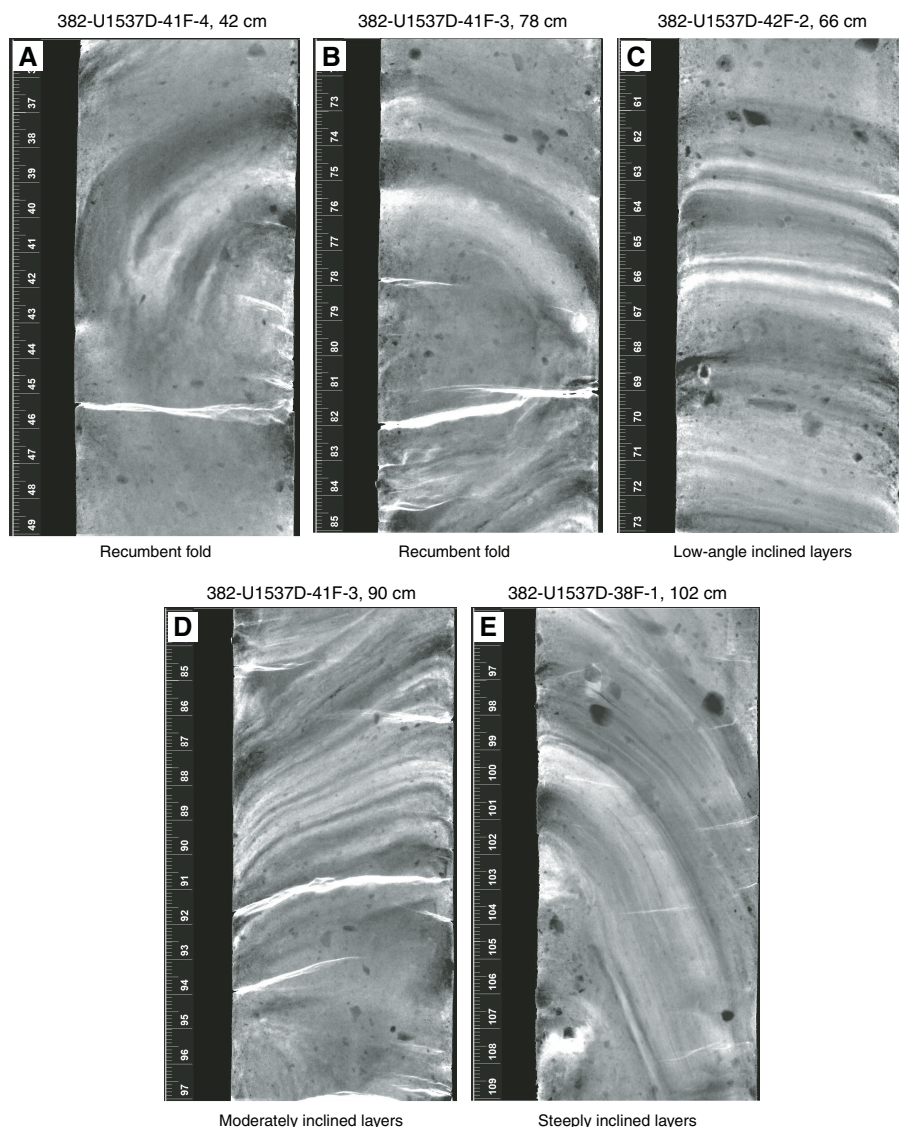
observed at this location (GAD field of  $-74^\circ$  inclination) and a random declination for a particular unoriented core (in this case  $45^\circ$  declination and  $-74^\circ$  inclination) from a Fisher distribution (Fisher, 1953; Figure F27A). Then we chose a set of “bedding” azimuths and dips that would arise from a cone of uparched distortions after the core is split (Figure F27B). After rotation about this bedding, we saw the resulting directions in Figure F27C. The resulting directions show a clear bias toward the fiducial line as found in the declination data set. The polarities are not obscured during this process, and our editing procedure appears to have mitigated the problem.

**Icefield MI-5 core orientation tool orientation results**

Three Icefield MI-5 tools were deployed during the collection of full-length APC cores (Table T14). Tool 2043 was used to orient Cores 382-U1537A-1H through 9H and 382-U1537D-11H through 18H. Tool 2007 was used to orient Cores 382-U1537A-10H through 18H and 382-U1537D-1H through 10H. Tool 2052 was used to orient Cores 382-U1537A-19H through 26H.

The results of attempted core orientation are shown in Figure F28. As in previous holes, the tools performed inconsistently be-

Figure F22. A–E. X-ray textures from slumped interval, Hole U1537D. Dips of (C)  $8^\circ$ – $14^\circ$ , (D)  $20^\circ$ – $30^\circ$ , and (E)  $>60^\circ$ .





tween the two holes and different tools behaved differently in the same hole. After using the tools to measure controlled fields in the laboratory (G. Messé, unpubl. data), we are confident that the tools themselves are accurately measuring the magnetic field. However, we hypothesize that there must be some stray magnetic field during the coring process that results in poor performance of the tool for the purposes of core orientation. Accordingly, we were unable to use the Icefield MI-5 data for core orientation during Expedition 382 (see **Paleomagnetism** in the Expedition 382 methods chapter [Weber et al., 2021a]).

### Magnetic polarity stratigraphy

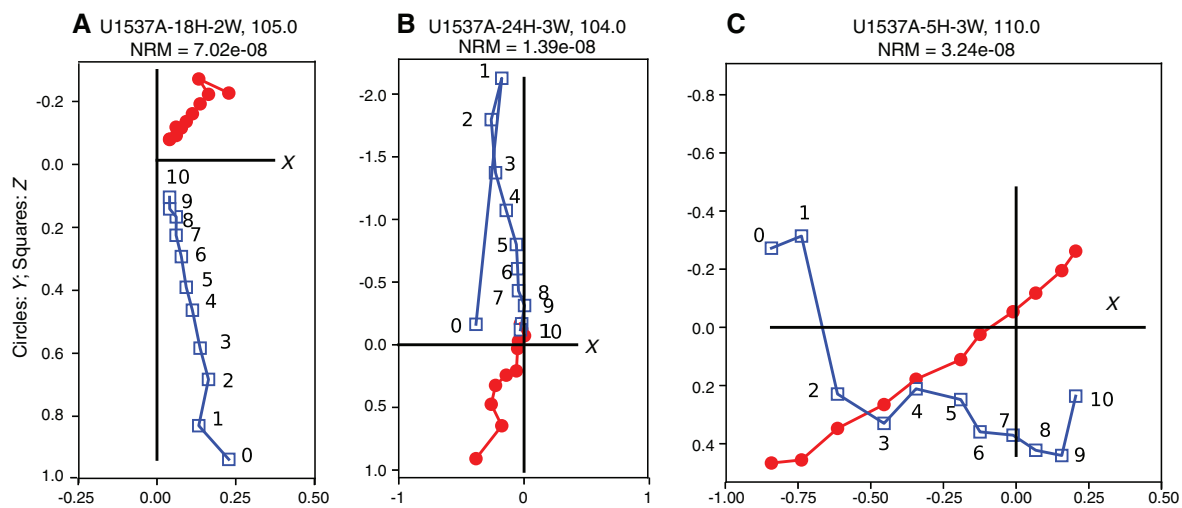
The preliminary magnetostratigraphic interpretations are based on inclinations from archive-half and discrete sample measurements from the 15 mT AF demagnetization step (Figures F18, F19, F20, F21) and are shown again in Figure F29. We defined polarity transition intervals as described in **Paleomagnetism** in the Site U1536 chapter (Weber et al., 2021b).

The magnetostratigraphic interpretations of Holes U1537A and U1537D are shown in Figure F29A and F29B in meters below seafloor. The data were transformed to the core composite depth below seafloor, Method A (CCSF-A), scale using the affine table in Table T20 (Figure F29C). Densities of inclination data versus depth are shown as density maps where brighter colors (in this case blue) indicate a higher density of data points. This process visually minimizes stray data points and highlights data that are consistent. Data were grouped into 5 m bins and treated with kdeplot (a function in

Table T12. Intervals of disturbed sediment excluded from paleomagnetic determinations as determined from inspection of X-radiographs and core section photographs, Hole U1537A. [Download table in CSV format.](#)

Table T13. Intervals of disturbed sediment excluded from paleomagnetic determinations as determined from inspection of X-radiographs, Hole U1537D. [Download table in CSV format.](#)

Figure F23. Representative vector endpoint diagrams showing progressive AF demagnetization behavior, Hole U1537A. Demagnetization steps: 1 = NRM, 2 = 5 mT, 3 = 10 mT, 4 = 15 mT, 5 = 20 mT, 6 = 30 mT, 7 = 35 mT, 8 = 40 mT, 9 = 50 mT. Drilling overprint is mostly removed by 10 mT. A. Normal specimen. B. Reversed specimen. C. Poorly behaved specimen.



the Seaborn Python plotting package) and then stacked from bottom to top to create density plots versus depth (Figure F29D). High densities to the left (right) of the plot indicate a preponderance of upward (downward) inclinations and can be interpreted to be normal (reversed) intervals. Our preferred correlations to the geomagnetic polarity timescale (GPTS2012) (Figure F29E) are shown as red lines, and the depths of these polarity transitions are listed in Table T15.

Hole U1537A preserves a succession of normal and reversed polarity zones that span Chrons C1n (Brunhes) to C2An.1n (late Gauss). Hole U1537D records a succession of normal and reversed polarity zones that we interpret to span Chrons C1n (Brunhes) to C2An.3n (early Gauss). Very little of the section from the slump at the base of Cores 382-U1537D-37F through 50F survived the X-ray quality control check. The surviving data in this interval suggest that Hole U1537D extends to Chron C2Ar (late Gilbert). Between these two holes, we have identified every polarity zone of the GPTS2012 since 4.19 Ma and recovered most of the polarity transitions.

An age-depth plot for the paleomagnetic tie points compared to the biostratigraphic tie points is shown in Figure F30. A third order polynomial fit through the paleomagnetic tie points does a reasonable job of fitting the data points, except at the bottom of Hole U1537D where the slump gives the appearance of very high sediment accumulation rates.

### Summary

Site U1537 APC cores preserve a well-defined succession of normal and reversed polarity zones. Paleomagnetic measurements made on archive halves were subjected to several levels of quality control tests using discrete samples, removal of intervals affected by large-scale coring-induced disturbance as determined during visual core description, and removal of intervals with centimeter-scale deformation as determined from inspection of X-rays of every core section. The combined data from 0 to 287.1 mbsf in Holes U1537A

Figure F24. A–L. Comparison of stepwise AF demagnetization of NRM and ARM for 12 discrete cube samples chosen to be representative of observed lithologies, Site U1537. All demagnetization curves are normalized by their value at 20 mT. Samples are arranged from (A) weakest ARM intensity to (L) strongest.

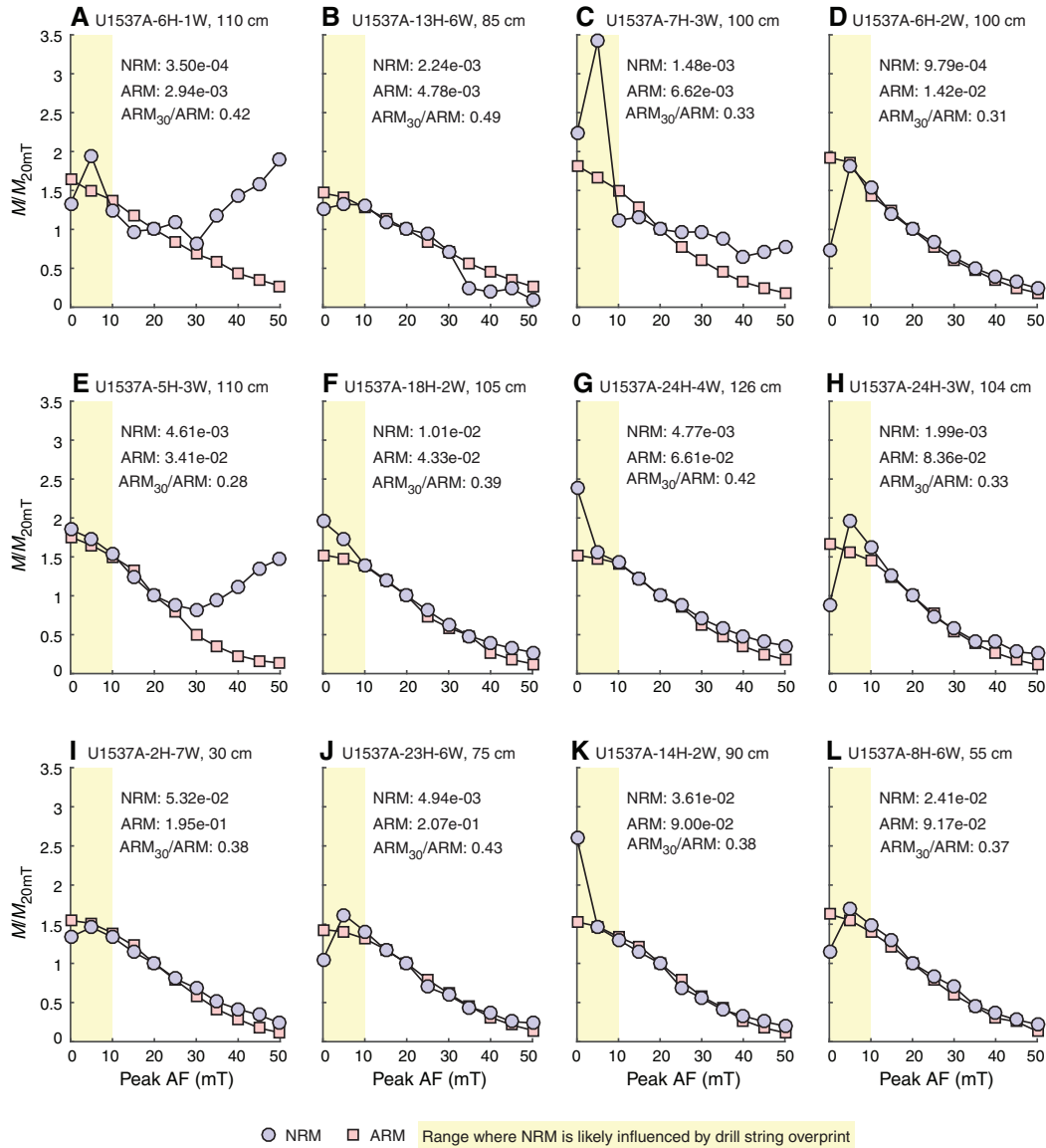


Figure F25. Frequency of inclination values (after editing) at 15 mT AF demagnetization step measured for (A) APC and (B) HLAPC cores, Site U1537. Blue curves = kernel density estimates (KDEs).

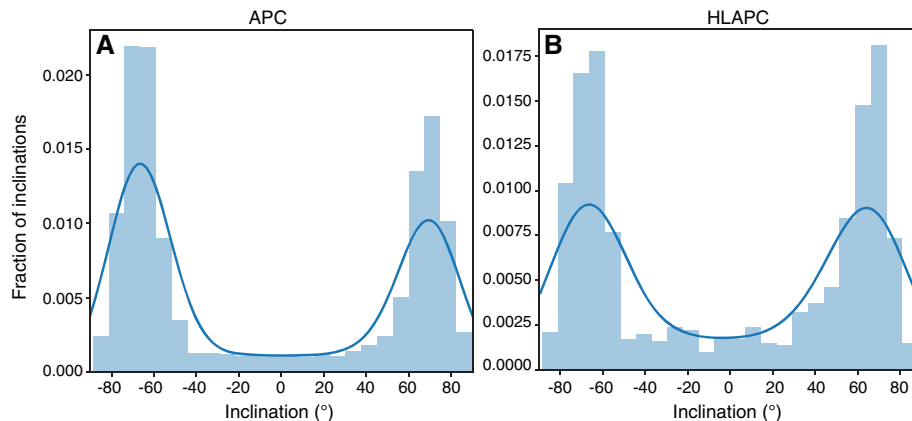


Figure F26. Declination values (after editing) at 15 mT AF demagnetization step measured for (A) APC and (B) HLAPC cores, Site U1537. C, D. Quantile-quantile plots of declinations (after editing; red) with Kolmogorov-Smirnov test results showing that a uniform distribution cannot be rejected at 95% level of confidence (Tauxe, 2010). Blue curve in D = declination data before editing that have a slightly different distribution showing that a uniform distribution can be rejected at 99% level of confidence.

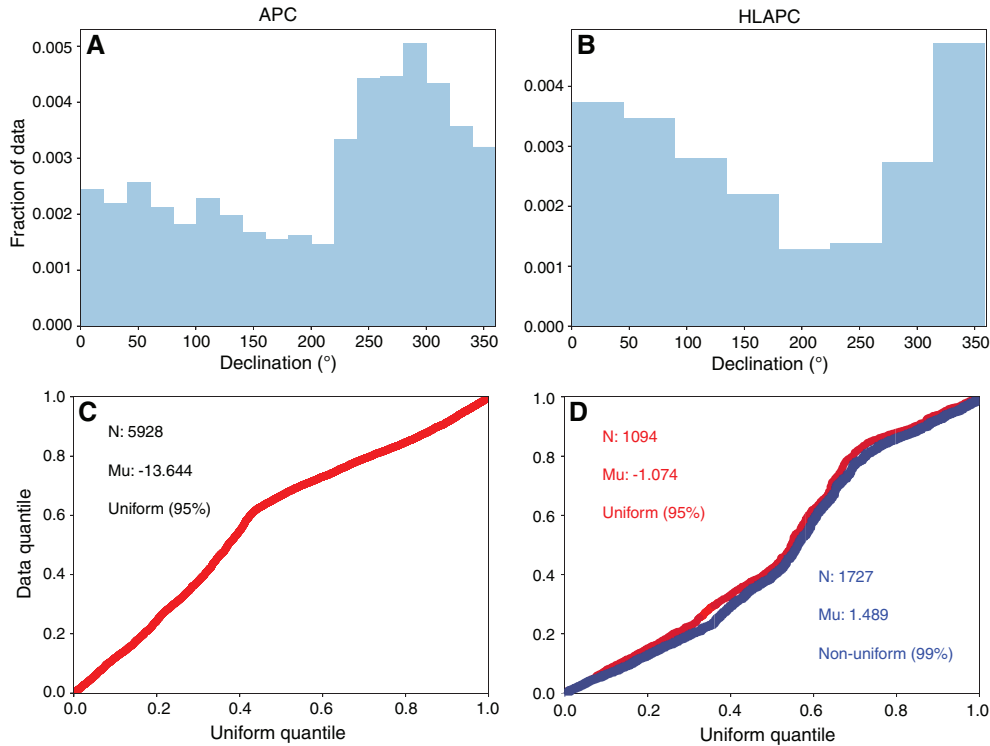


Figure F27. Test of hypothesis that uparching of sediments in archive halves leads to bias in declinations toward double line, Site U1537. A. Set of 100 directions drawn from Fisher distribution with declination of 45° and inclination of -75°. B. Set of poles to planes modeling upward bowing of sedimentary layers in archive half. C. Resulting directions after bowing.

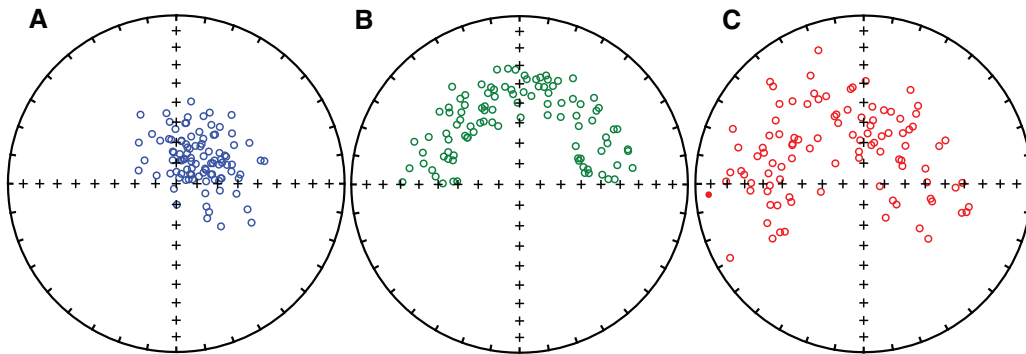


Table T14. Magnetic tool face azimuths for each oriented core, Site U1537. [Download table in CSV format.](#)

and U1537D span Chrons C1n (Brunhes) to C2An.3n (early Gauss). The 287.1–348.94 mbsf interval in Hole U1537D consists of slumped sediment with nearly continuous intervals of uparching,

inclined bedding, folds, and other centimeter-scale disturbances identified in X-ray images. Only sparse measurements from this interval survived the X-ray control check. The remaining data in this interval suggest that Hole U1537D extends to Chron C2Ar (late Gilbert). Between these two holes, we have identified every polarity zone of the GPTS2012 since 4.19 Ma and recovered most of the polarity transitions.

Figure F28. A, B. Equal-area projections of normal core mean directions before (red) and after (blue) adjustment using Icefield MI-5 tools as described in text, Holes U1537A and U1537D. All directions are in upper hemisphere.

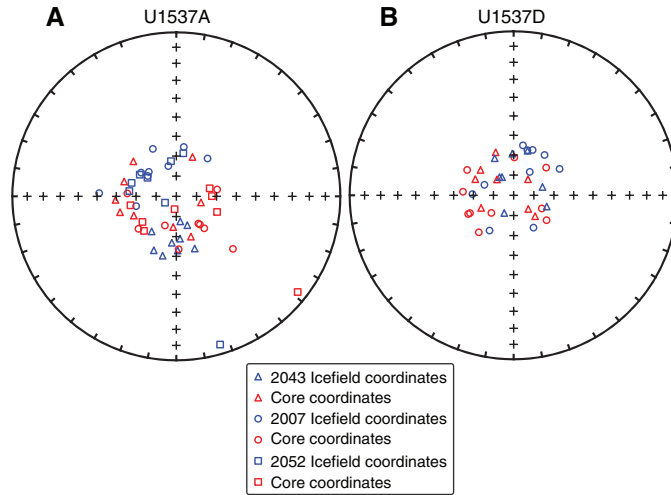


Figure F29. Magnetostratigraphic correlation. A, B. Holes U1537A and U1537D (mbsf). C. Inclination converted to CCSF-A depth using affine in Table T20. D. Data grouped in 5 m bins and plotted as KDEs. E. GPTS2012. Red lines = our ties to GPTS. Polarity: black = normal, white = reversed.

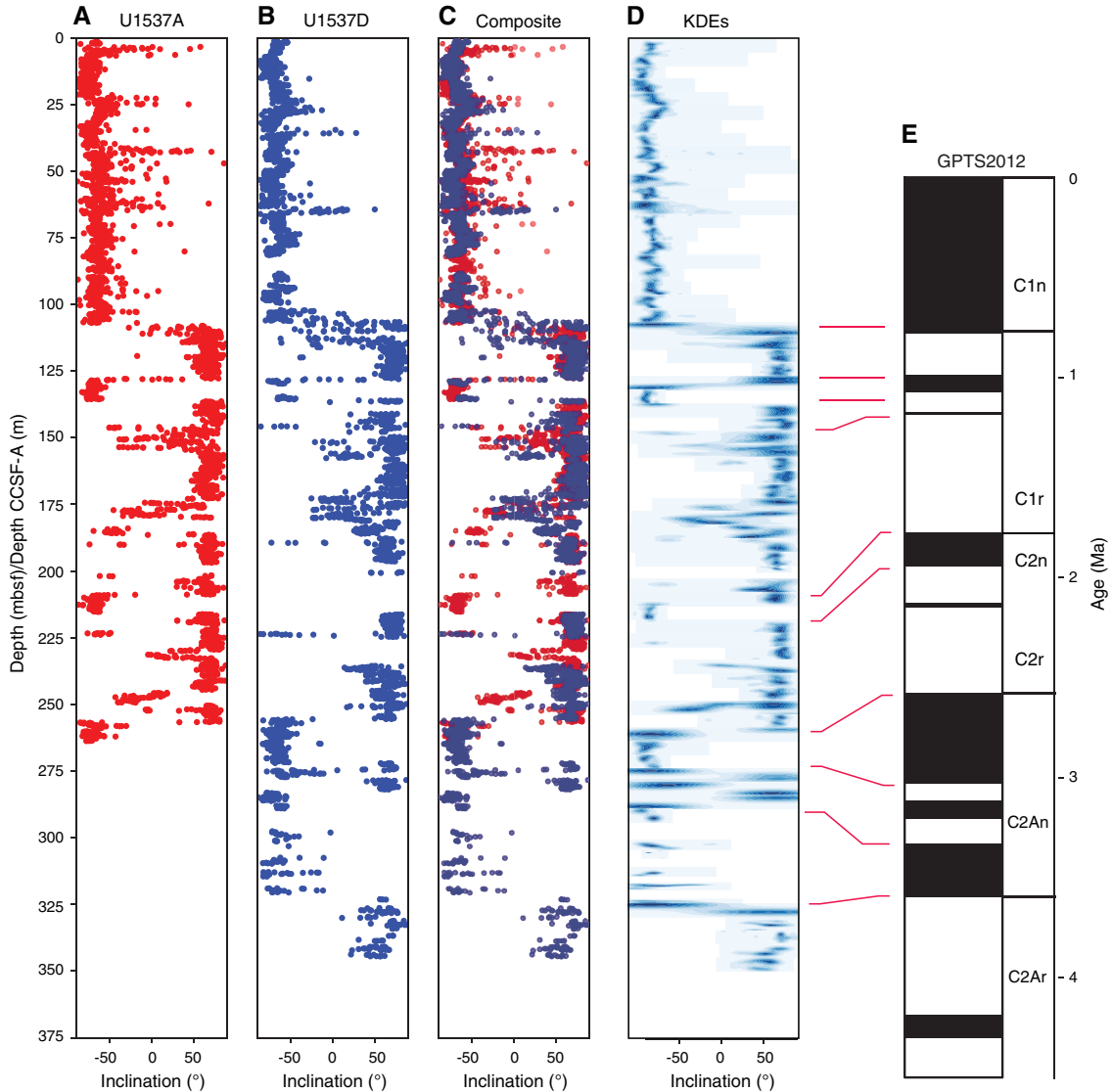
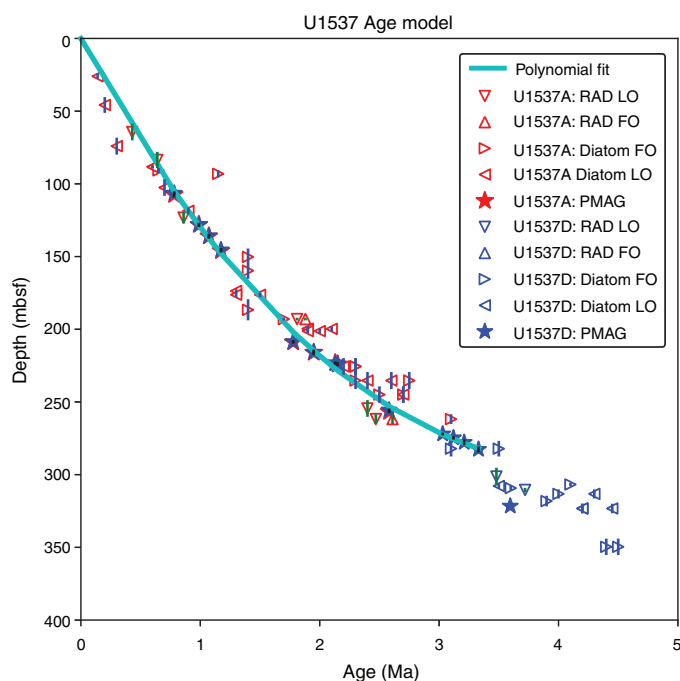


Table T15. Depth intervals of interpreted geomagnetic polarity, Holes U1537A and U1537D. o = old, y = young. [Download table in CSV format.](#)

Chron datum	Age (Ma)	Top core, section, interval (cm)	Top depth CSF-A (m)	Bottom core, section, interval (cm)	Bottom depth CSF-A (m)	Midpoint depth CSF-A (m)	Range (±) (m)
382-U1537A-							
C1n (o)	0.781	12H-7, 45	106.96	382-U1537A-13H-1, 100	108.00	107.48	1.04
C1r.1n (y)	0.988	15H-2, 35	127.87	15H-2, 70	128.22	128.05	0.35
C1r.1n (o)	1.072	15H-7, 55	135.60	16H-1, 85	136.35	135.98	0.75
C1r.2n (y)	1.173	17H-1, 95	145.95	17H-1, 120	146.20	146.08	0.25
C2n (y)	1.778	23H-5, 85	208.83	23H-5, 95	208.93	208.88	0.10
C2n (o)	1.95	24H-3, 135	215.85	24H-4, 15	216.15	216.00	0.30
C2r.1n (y)	2.13	25H-2, 65	223.15	25H-2, 70	223.20	223.18	0.05
C2r.1n (o)	2.15	25H-2, 135	223.85	25H-3, 15	224.15	224.00	0.30
C2An.1n (y)	2.581	30F-2, 75	256.64	30F-2, 85	256.74	256.69	0.10
382-U1537D-							
C1n (o)	0.781	12H-4, 45	106.23	382-U1537D-12H-4, 80	106.58	106.41	0.35
C1r.1n (y)	0.988	14H-6, 20	128.00	14H-6, 70	128.50	128.25	0.50
C1r.1n (o)	1.072	15H-4, 135	135.65	15H-5, 20	136.00	135.83	0.35
C1r.2n (y)	1.173	16H-8, 75	145.22	16H-9, 15	145.59	145.41	0.37
C2n (y)	1.778	24H-2, 115	208.47	24H-2, 125	208.57	208.52	0.10
C2n (o)	1.95	24H-7, 65	215.37	25H-1, 85	216.25	215.81	0.88
C2r.1n (y)	2.13	25H-6, 80	223.45	25H-6, 85	223.50	223.48	0.05
C2r.1n (o)	2.15	25H-6, 135	224.00	25H-7, 20	224.31	224.16	0.31
C2An.1n (y)	2.581	30F-2, 50	255.49	30F-2, 60	255.59	255.54	0.10
C2An.1n (o)	3.03	33F-4, 15	272.00	33F-4, 20	272.05	272.03	0.05
C2An.2n (y)	3.12	34F-2, 30	274.50	34F-2, 60	274.80	274.65	0.30
C2An.2n (o)	3.21	34F-4, 55	277.28	35F-1, 85	278.35	277.82	1.07
C2An.3n (y)	3.33	35F-4, 55	282.05	36F-1, 85	283.15	282.60	1.10
C2An.3n (o)	3.6	43F-4, 40	320.52	44F-2, 85	323.04	321.78	2.52

Figure F30. Age-depth plot for data in Table T15, Site U1537. RAD = radiolarian, PMAG = paleomagnetism.



## Geochemistry

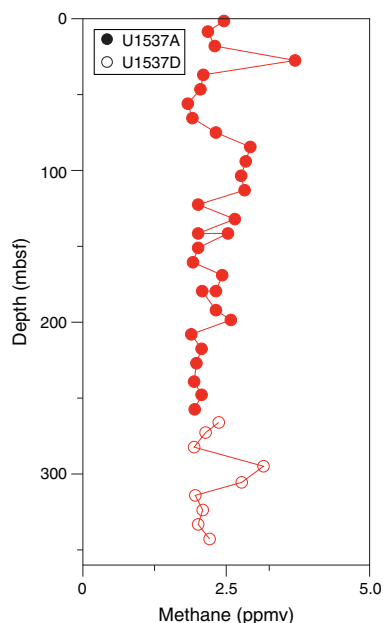
### Volatile hydrocarbons

Headspace gas analyses were conducted at a resolution of one sample per full-length core (9.6 m advance) or one sample every other core for half-length cores (4.8 m advance) throughout Holes U1537A and U1537D (Cores 382-U1537A-1H through 30F and 382-U1537D-28F through 48F) as part of the routine environmental protection and safety monitoring program. Methane (CH<sub>4</sub>) is the dominant hydrocarbon present in low concentrations (1.9–3.2 parts per million by volume [ppmv]) throughout the core. Ethane (C<sub>2</sub>H<sub>6</sub>) concentrations are below the detection limit throughout the cored interval (Figure F31; Table T16).

### Interstitial water chemistry

Shipboard chemical analysis of the IW from Site U1537 sediments followed the procedures detailed in **Geochemistry** in the Expedition 382 methods chapter (Weber et al., 2021a). Geochemical data were generated on 18 IW samples from Hole U1537A to 262 mbsf (Cores 382-U1537A-1H through 24H); one additional sample was taken at the mudline, and three samples were taken from Hole U1537D below the interval cored in Hole U1537A (Cores 382-U1537D-38F through 50F). The geochemical properties for IW from Holes U1537A and U1537D are displayed together with different symbols for better distinction of IW properties, and the main

Figure F31. Methane concentrations, Site U1537.

Table T16. Volatile hydrocarbon concentrations, Site U1537. [Download table in CSV format.](#)

results from the shipboard analyses are presented in Figures F32 and F33 and Table T17.

### Salinity, sulfate, alkalinity, ammonium, pH, phosphate, iron, and manganese

Salinity in the upper 30 m matches local salinities within error (~34.5 compared with 34.7 at the nearest seawater sampling site from the Global Ocean Data Analysis Project Version 2 (GLODAPv2; Olsen et al., 2016; Key et al., 2015) and then decreases successively by ~2.5 to 190 mbsf. Below this depth, salinity remains constant at 32 throughout the rest of the section. Hole U1537A exhibits generally reducing sedimentary conditions, as indicated by the disappearance of dissolved sulfate concentrations at ~85 mbsf, yet Site U1537 is not methanogenic at any depth. Dissolved sulfate concentrations increase again below 160 mbsf and remain constant at ~5.5 mM to the bottom of Hole U1537D at 350 mbsf.

Microbially mediated organic matter degradation is inferred to be the reason for the phosphate enrichment in the upper 85 m. High Ba concentrations are inferred to indicate where sedimentary barite is dissolved between 85 and 160 mbsf in the absence of dissolved sulfate (Figure F32). Alkalinity increases downcore from 9 mM close to the seafloor to a maximum of 29 mM at 94 mbsf. Alkalinity levels are visually correlated with dissolved ammonium concentrations (Figure F32), providing a linear correlation with  $R^2 = 0.79$ .

Dissolved Mn concentrations are highest (45  $\mu\text{M}$ ) at 9 mbsf and generally elevated in the upper 40 m. Below 40 mbsf, Mn concentrations are low throughout most of the interval recovered but rise to higher levels between 260 mbsf and the bottom of Hole U1537D. Dissolved Fe is slightly enriched (6.5  $\mu\text{M}$ ) at the uppermost sampled depth (9 mbsf); otherwise, it is below or close to the detection limit (Figure F33). Together, the IW Fe and Mn concentration patterns in the upper 200 mbsf suggest that sedimentary reductive processes do

not lead to generally elevated dissolved Fe and Mn at least at the sampled spacing, apart from elevated Mn levels in the uppermost 30 m.

### Calcium, magnesium, silicon, barium, and other major and trace elements

Calcium concentrations are similar to local seawater at the top of the site but trend down to a minimum at ~60 mbsf in the upper part of Hole U1537A. The Ca depletion in the upper 85 m is most likely a function of authigenic carbonate fluorapatite, authigenic carbonate, and/or gypsum formation. The preferential removal of Ca between 30 and 85 mbsf creates elevated Mg/Ca, B/Ca, Ba/Ca, Sr/Ca, and Si/Ca ratios in the IW around 75–105 mbsf (Figure F33). Calcium concentrations trend toward higher concentrations from ~160 mbsf to the bottom of the site.

Dissolved Mg concentrations steadily decrease downhole from typical seawater concentrations (~53 mM) to concentrations as low as ~22 mM at 352 mbsf. The trend of decreasing Mg (and K) concentration below 85 mbsf is likely a reflection of authigenic clay formation.

Dissolved Ba concentrations increase significantly in the sulfate-depleted interval between 80 and 100 mbsf, most likely resulting from barite dissolution in this interval. This process is reversed below 104 mbsf where we observed rapidly decreasing dissolved Ba. At 191 mbsf, Ba concentrations drop close to zero, coinciding with the reemergence of dissolved sulfate. Dissolved Ca remains constant throughout the barite dissolution interval seen from 85 to 160 mbsf, whereas Sr is also enriched in the interval of active barite dissolution.

Below ~103 mbsf, both dissolved K concentrations and Na/K ratios suggest preferential K removal, a phenomenon most likely reflecting early diagenetic glauconite-smectite formation at Site U1537. Increases in Sr approximately follow the Ba enrichment between 85 and 103 mbsf. Below the Ba and Sr concentration maxima, their respective concentration trends become decoupled; dissolved Sr increases again below 160 mbsf, whereas Ba concentrations decrease. The trends seen in dissolved Sr hence suggest competing reactions controlling Sr concentrations in the sulfate reduction and barite dissolution zone beneath. For example, except for the maximum that coincides with that of the Ba profile, Ca and Sr concentrations increase in concert downcore, whereas Mg decreases in concert with K. A more extended discussion surrounding potential controls over Ca, Mg, and Sr in IW is provided in [Geochemistry](#) in the Site U1536 chapter (Weber et al., 2021b).

As seen at the other Scotia Sea Sites U1536 and U1538 and despite the high biogenic silica content at these Southern Ocean sites, the key control behind dissolved Si concentrations is difficult to identify with certainty at this stage because multiple factors, including detrital mineral and biogenic silica dissolution as well as authigenic clay formation, affect Si concentrations downcore (Dixit et al., 2001). Boron also increases downcore over the uppermost ~100 m and remains at concentrations between 678 and 761  $\mu\text{M}$  shallower than 262 mbsf before increasing to the highest measured concentrations on the order of 986  $\mu\text{M}$  at 352 mbsf.

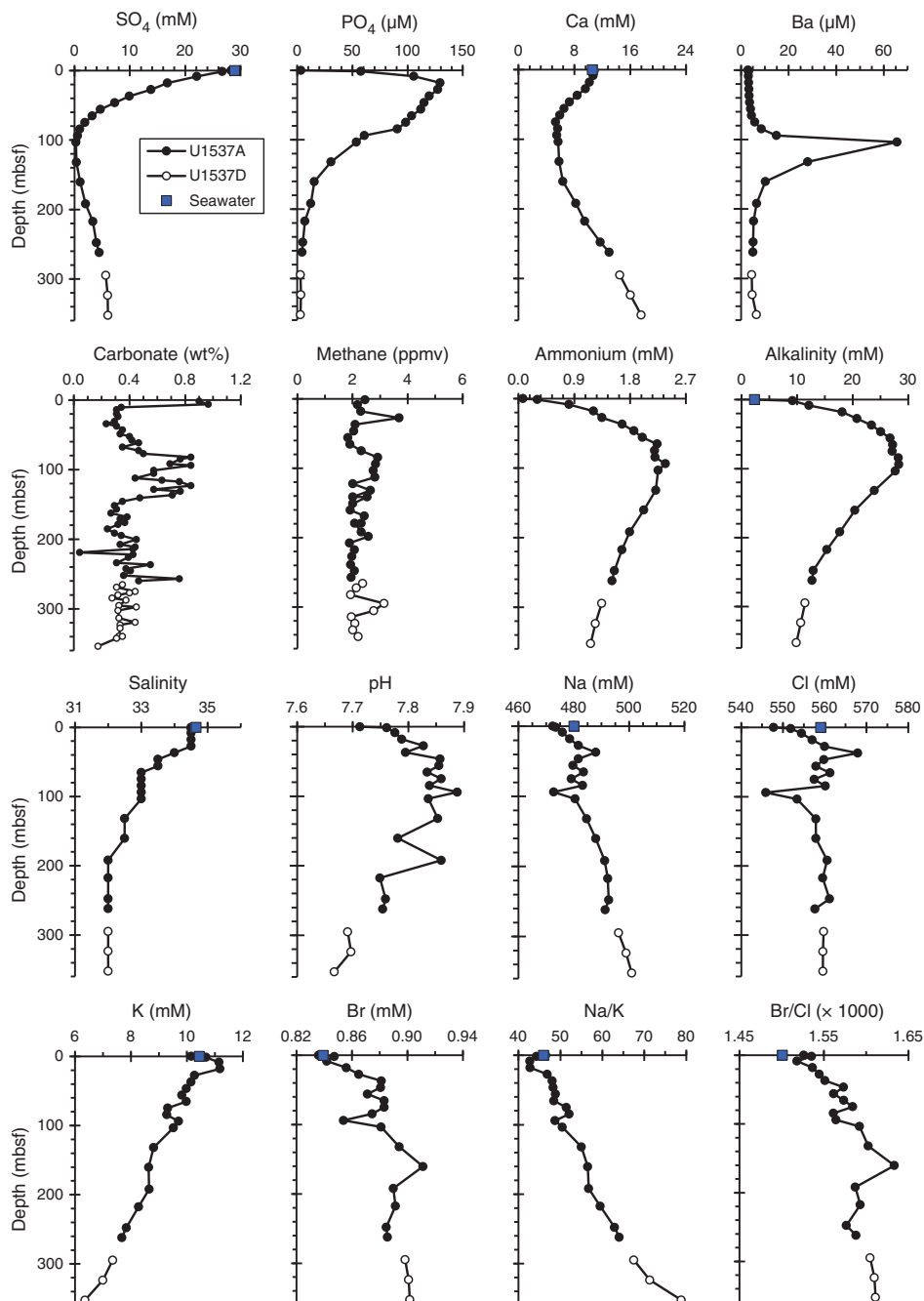
## Bulk sediment geochemistry

### Carbon, nitrogen, and carbonate

Inorganic carbon, total nitrogen (TN), and total carbon (TC) were measured on selected core samples from Site U1537. Table T18 and Figure F34 present the results of TC, total organic carbon



Figure F32. IW properties ( $\text{SO}_4$ ,  $\text{PO}_4$ , Ca, Ba, carbonate, methane, ammonium, alkalinity, salinity, pH, Na, Cl, K, Br, Na/K, and Br/Cl), Site U1537. Blue squares = seawater concentrations or elemental ratios for reference (where applicable).



(TOC), TN, and  $\text{CaCO}_3$  contents in Holes U1537A ( $N = 56$ ) and U1537D ( $N = 21$ ). Hole U1537A has relatively low contents of TOC (0.02–0.7 wt%), TN (0.01–0.09 wt%), and  $\text{CaCO}_3$  (0.04–0.97 wt%). The consistent average TOC/TN ratio of 6.4 downcore at Site U1537 indicates a predominance of marine organic material.

### Inorganic bulk sediment geochemistry

A wide range of major and trace elements were measured for Site U1537, and a selection of key elements and ratios are displayed in Figures F35 and F36. All data are presented in Table T19. Although the variability downcore is rather minor over large sections, the most notable feature of the bulk sediment signature is a change

in geochemical properties at ~90 mbsf. Below this depth,  $\text{Al}_2\text{O}_3$ , MgO,  $\text{P}_2\text{O}_5$ ,  $\text{TiO}_2$ ,  $\text{K}_2\text{O}$ ,  $\text{Fe}_2\text{O}_3$ , Ba, La, and Zr are higher, whereas other elements (e.g., CaO,  $\text{Na}_2\text{O}$ , MnO, Sr, and Cr) do not show distinct variations (Figures F35, F36). The low CaO concentrations confirm the lack of significant carbonate at the site, with the exception of one carbonate-rich layer at 296 mbsf.  $\text{SiO}_2$  contents are generally very high throughout the site, although a distinction between biogenic and terrigenous  $\text{SiO}_2$  cannot be made solely based on the geochemical records. Geochemical properties observed in IW samples have no simple correspondence to the bulk sediment geochemical data.

Figure F33. IW properties (Ca, Si, B, Sr, Mg, Fe, Mn, B/Ca, Mg/Ca, Si/Ca, Ba/Ca, Sr/Ca, Mg/Si, Mg/K, K/Ca, and Na/Cl), Site U1537. Blue squares = seawater concentrations or elemental ratios for reference (where applicable).

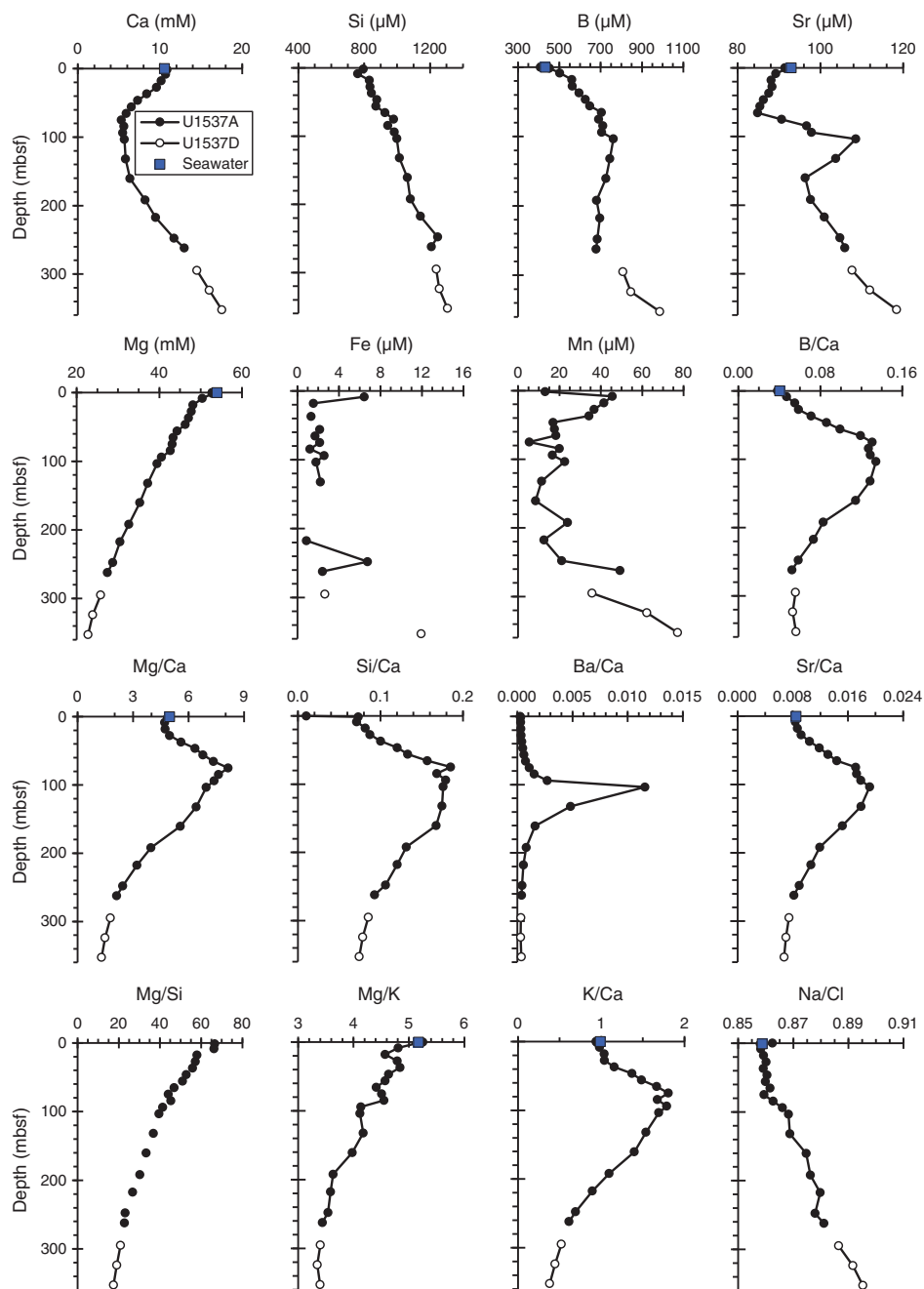


Table T17. Interstitial water geochemical data, Site U1537. [Download table in CSV format.](#)

Table T18. TOC, CaCO<sub>3</sub>, TN, and TOC/TN ratio, Site U1537. [Download table in CSV format.](#)

### Rhizon interstitial water samples

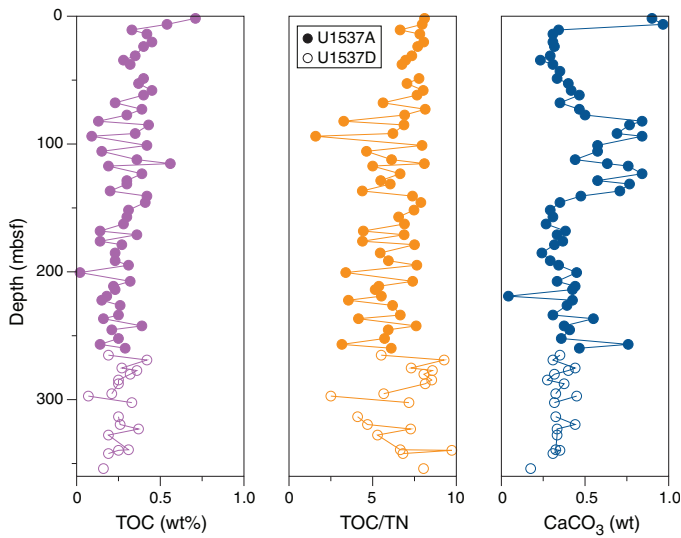
Rhizon IW samples ( $N = 23$ ) were taken from Sections 382-U1537B-1H-1 through 1H-5 (0–7 mbsf) following the IW sampling guidelines (see [Geochemistry](#) in the Expedition 382 methods chapter [Weber et al., 2021a]). The resolution for collected samples was 20 cm for the upper 3 m and 50 cm from 3 to 7 mbsf. Shore-based analyses of  $\delta^{18}\text{O}$ ,  $\delta\text{D}$ ,  $\delta^{13}\text{C}_{\text{DIC}}$ , Li isotopes ( $\delta^7\text{Li}$ ), Mg isotopes ( $\delta^{26}\text{Mg}$ ), and K isotopes ( $\delta^{41}\text{K}$ ) (~1 mL) using multicollector induc-

tively coupled plasma–mass spectrometry will be carried out at the Korea Basic Science Institute (Korea).

### Summary

Samples from Holes U1537A and U1537D were analyzed for headspace gas, IW chemistry, and bulk sediment geochemistry. Geochemical profiles at this site are similar to those at Site U1536, but individual diagenetic horizons are not developed as strongly as

Figure F34. Bulk sediment TOC, TOC/TN ratio, and CaCO<sub>3</sub>, Site U1537.



at Site U1536. Headspace methane concentrations are low (1.9–3.2 ppmv) throughout the sedimentary sequence, and ethane, propane, and higher molecular weight hydrocarbons are below the detection limit. Site U1537 is characterized by moderately reducing sedimentary conditions, as indicated by the disappearance of dissolved sulfate at ~85 mbsf and its reappearance at ~160 mbsf. Microbially mediated organic matter degradation is inferred to be the cause of the elevated phosphate concentrations and sulfate reduction in the upper section, followed by an interval of barite dissolution (85–160 mbsf), the reappearance of dissolved sulfate at depth, and tentative evidence for authigenic clay formation below 100 mbsf. Bulk sediment TOC and TN contents are generally low, varying from 0.02 to 0.7 wt% and from 0.01 to 0.09 wt%, respectively. Inorganic bulk sediment analyses were carried out on 28 samples from Hole U1537A and nine further depths from Hole U1537D for an assessment of the sediment geochemistry. The upper 90 m is distinguished from lower sections by various distinct bulk sediment major and trace element concentrations. A single sedimentary layer at 296 mbsf is classified as a pure carbonate layer. The vast majority of sediment samples have a dominantly terrigenous signature.

Figure F35. Bulk sediment major element compositions, Site U1537.

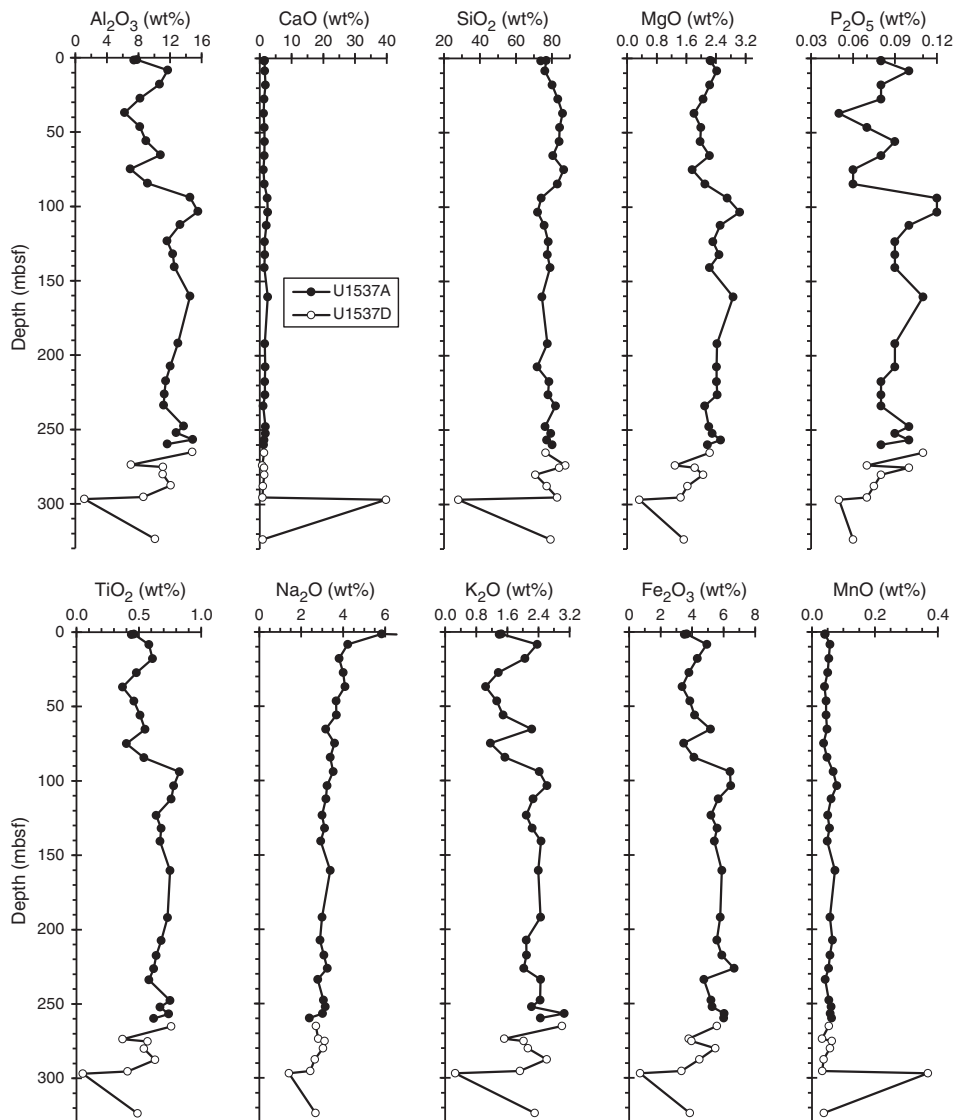


Figure F36. Selected trace element compositions and elemental ratios, Site U1537. La is a rare earth element, and Zr is a high field strength element. Note that elemental ratios shown here are weight ratios.

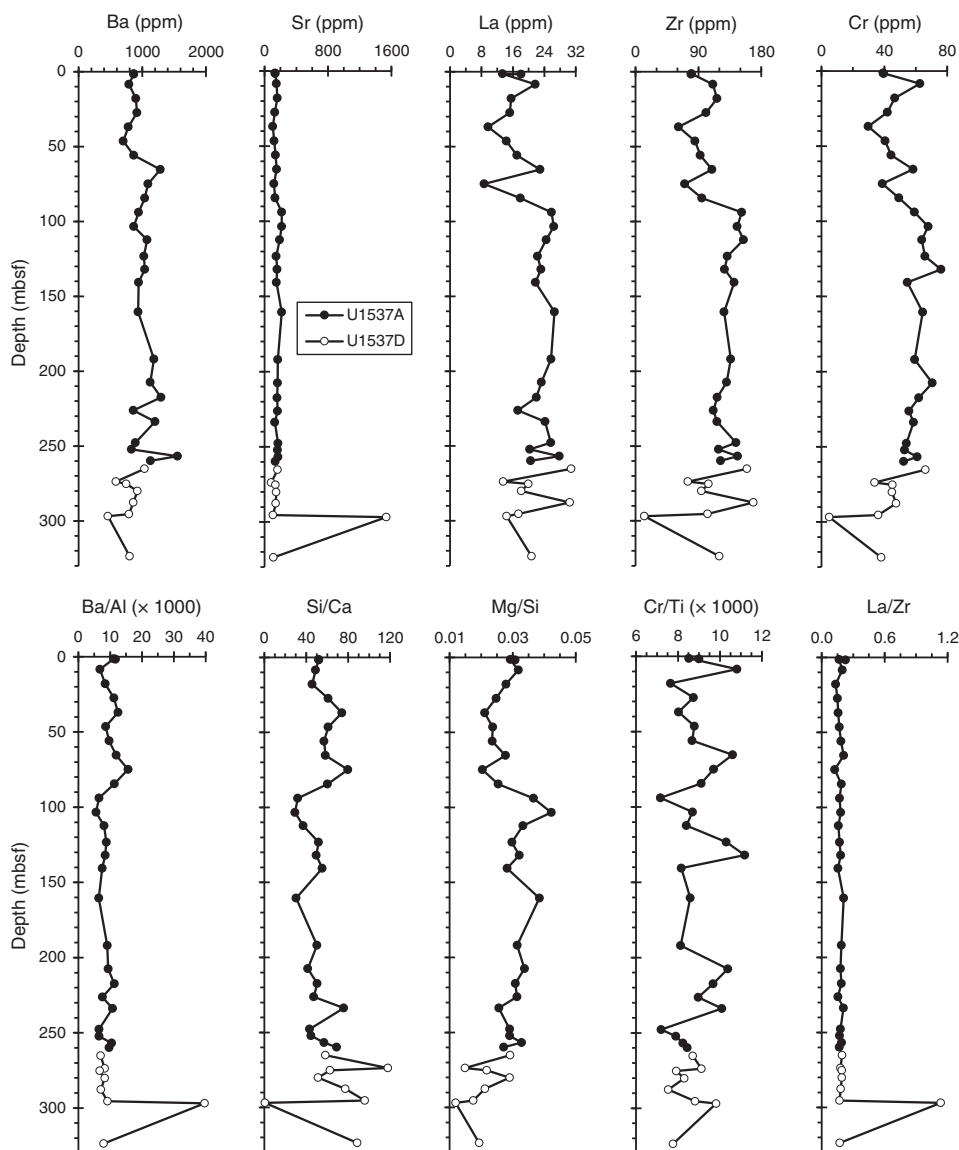


Table T19. Inductively coupled plasma–atomic emission spectroscopy sediment data, Site U1537. [Download table in CSV format.](#)

## Physical properties

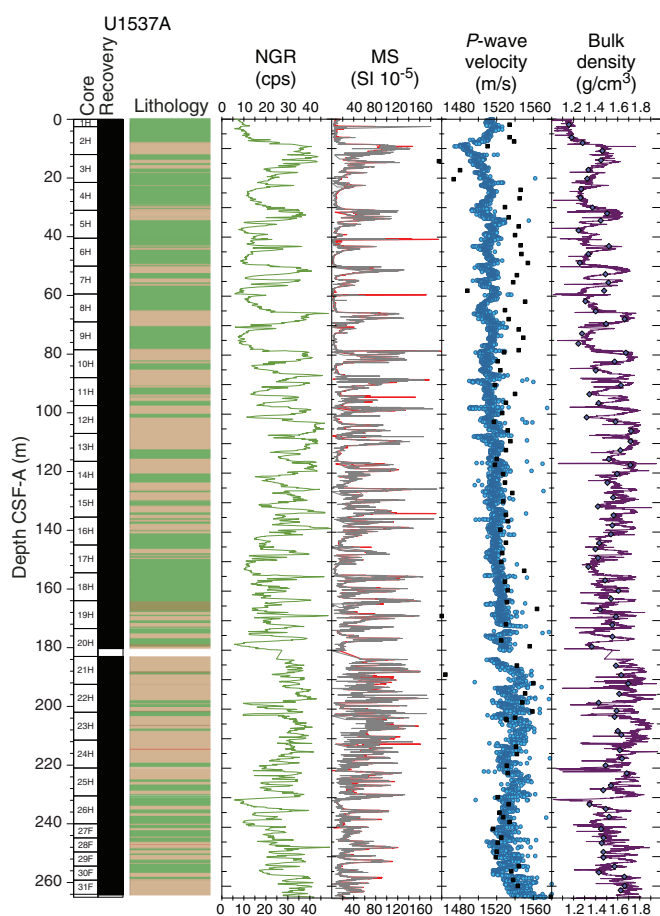
High-resolution physical property measurements were made on all cores and most core catchers from Holes U1537A–U1537D to provide basic information on sediment composition and variability. The Whole-Round Multisensor Logger (WRMSL) measured gamma ray attenuation (GRA) bulk density, MS, and compressional wave velocity on the *P*-wave logger (PWL) at 2.5 cm intervals. The PWL was used for all APC and HLAPC cores. On whole-round cores, we also measured natural gamma radiation (NGR; at 10 cm increments). Once the cores were split, the section halves were X-rayed and thermal conductivity measurements (one per core) were made for all holes. *P*-wave caliper (PWC) velocity was acquired in at least three sections per core for Holes U1537A–U1537D. For archive

halves, point magnetic susceptibility (MSP) and color reflectance were measured at 2.5 cm increments using the Section Half Multisensor Logger (SHMSL) and digital color imaging was completed with the Section Half Imaging Logger (SHIL). Additionally, we took discrete samples from Holes U1537A and U1537D for moisture and density (MAD) measurements (1–3 samples per core; ideally samples that provide an overall representation of the different lithologies) to determine water content, wet bulk density, dry bulk density, porosity, and grain density.

## Whole-Round Multisensor Logger measurements

Results from WRMSL measurements for Holes U1537A and U1537D are compiled in Figures F37 and F38. We measured high-resolution data (2.5 cm intervals) for all cores and the majority of the core catchers. All cores from Holes U1537A–U1537D rested for about 4 h to adjust to room temperature (~20°) before they were measured.

Figure F37. Physical property data, Hole U1537A. MS: red = WRMSL, gray = SHMSL (MSP). *P*-wave velocity: dots = WRMSL, squares = PWC. Wet bulk density: line = WRMSL, diamonds = discrete. cps = counts per second.



### Gamma ray attenuation bulk density

Wet bulk density values range from 1.3 to almost 2 g/cm<sup>3</sup> and have a mean value of 1.7 g/cm<sup>3</sup>. Clear and high-amplitude glacial–interglacial cyclicity is observed downhole for the GRA bulk density, especially in the upper part of the hole. Also, a more or less constant overall increase occurs downhole. Low values are found in Cores 382-U1537D-7H and 26H (~60 and 230 mbsf, respectively), and the highest values are located in Cores 12H, 22H, 35F, and 43F (Figures F37, F38). A general linear positive correlation of density and NGR is found with respect to depth, and another is found for density and MS (Figure F39). GRA bulk density values agree with calculated density values from the MAD discrete samples and hence confirm the high data quality (Figures F37, F38).

### Magnetic susceptibility

MS is sensitive to the concentration and type of magnetic minerals present in the sediments. Although it usually appears as sharp peaks of high-amplitude variability, MS also appears to follow glacial–interglacial cycles. Values range from 0 to 160 × 10<sup>-5</sup> SI. The baseline of the signal is relatively constant downhole through Core 382-U1537D-21F, and then higher frequency variability in MS is observed through Core 26H. This change also agrees with a major lithologic shift from more diatom ooze and silty clay dominant to silty clay dominant. Strong amplitude variability is observed in Cores 2H, 4H, 14H, 18H, and 21F–26H (amplitudes reaching 225 × 10<sup>-5</sup> SI).

The highest MS values are found between Cores 382-U1537D-17H and 21F (>30 × 10<sup>-5</sup> SI), and the lowest values (<10 × 10<sup>-5</sup> SI) are between Cores 5H and 9H. Generally, we observe a strong correlation in the variability with depth for all physical properties determined using the WRMSL. In addition, a linear dependence with some scattering is found for MS and NGR with depth (Figure F39).

### *P*-wave velocity

Although *P*-wave velocity values measured with the PWL are erroneous if cracks or poor contact with the liner wall occur, the measurements were generally good, and values range from 1480 to 1650 m/s. However, numerous spikes are found in the data in specific cores and especially from Core 382-U1537D-31F downhole. PWL values increase gradually and continuously downhole, reaching 1650 m/s in Core 43F. The lowest velocity values are in Cores 2H and 4H (10 and 30 mbsf, respectively), and the highest values are in Core 38F.

### Natural gamma radiation

Cyclic changes in NGR are observed throughout the hole. The highest amplitude cycles are in Cores 382-U1537D-2H through 9H. High NGR values (>40 counts/s) are observed in Cores 2H (~10 mbsf) and 11H–13H (90–120 mbsf). NGR values display significant variation, and the lowest NGR counts are observed in Cores 7H–9H, 26H, and 27H (~5–10 counts/s). High-amplitude variability is observed throughout the sediment column (e.g., in Core 9H; 35 counts/s) (Figures F37, F38).

### Thermal conductivity

Thermal conductivity varies between 0.7 and 1.4 W/(m·K) in Holes U1537A and U1537D (Figures F40, F41). A clear variability occurs downhole, and a first high is observed in Core 382-U1537D-13H (~120 mbsf). The highest thermal conductivity value is then observed in Core 43F. The average thermal conductivity is 1.1 W/(m·K), with some dependence on lithology. The lowest values were measured in Cores 9H and 35F (80 and 280 mbsf, respectively) where the greatest variety of lithologies was observed. Thermal conductivity measurements were combined with borehole temperatures to make heat flow estimates (see [Downhole measurements](#)).

### Point magnetic susceptibility

MSP measurements were performed on archive halves. Results agree with the WRMSL MS data (Figures F37, F38). MSP measurements were mostly acquired at 2.5 cm, the same resolution as the WRMSL. In some cases, higher variability is observed with this instrument because of the smaller integration volume of the sensor (~1 cm depth resolution; 1σ) compared with the loop sensor (~18 cm depth resolution; 1σ) used on the WRMSL (Weber et al., 1997).

### Discrete compressional wave velocity

Discrete *P*-wave measurements were made using the PWC (see [Physical properties](#) in the Expedition 382 methods chapter [Weber et al., 2021a]). Measurements were taken from Holes U1537A and U1537D. Two to three samples per APC core were measured for *P*-wave using the PWC to provide a correlation for PWL values measured on the whole-round cores. One to two *P*-wave measurements were made per HLAPC core in deeper intervals in both Holes U1537A (Core 382-U1537A-27F and deeper) and U1537D (Cores 382-U1537D-20F through 21F and 30F and deeper). An automated algorithm determined PWC values unless a weak signal or poor

Figure F38. Physical property data, Hole U1537D. MS: red = WRMSL, gray = SHMSL (MSP). *P*-wave velocity: dots = WRMSL, squares = PWC. Wet bulk density: line = WRMSL, diamonds = discrete.

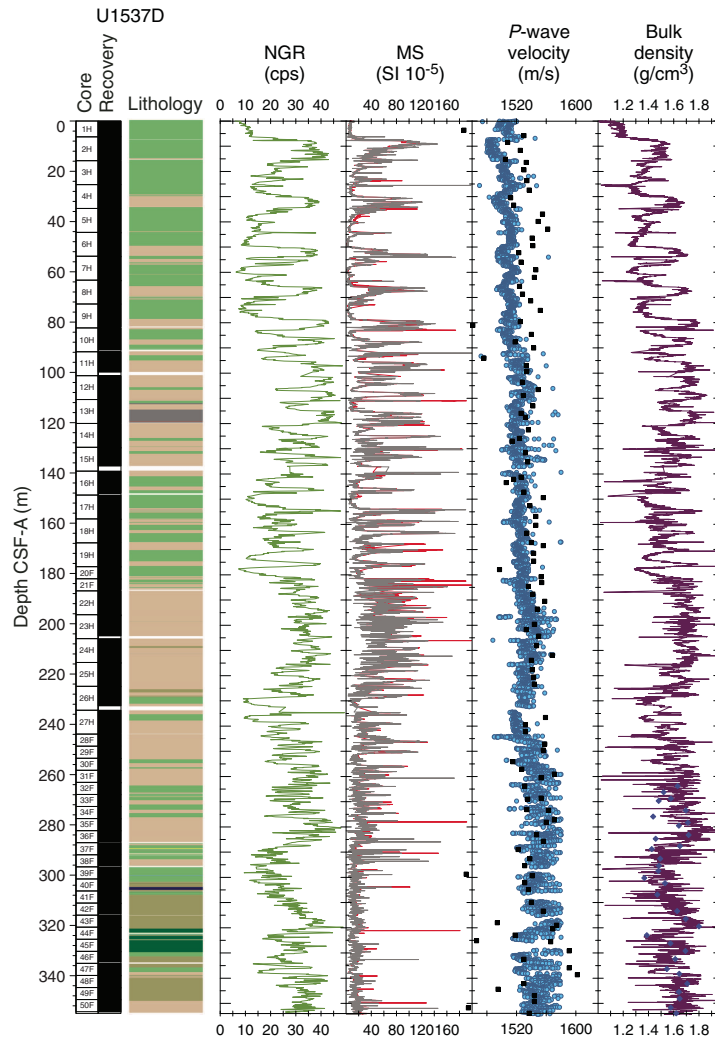
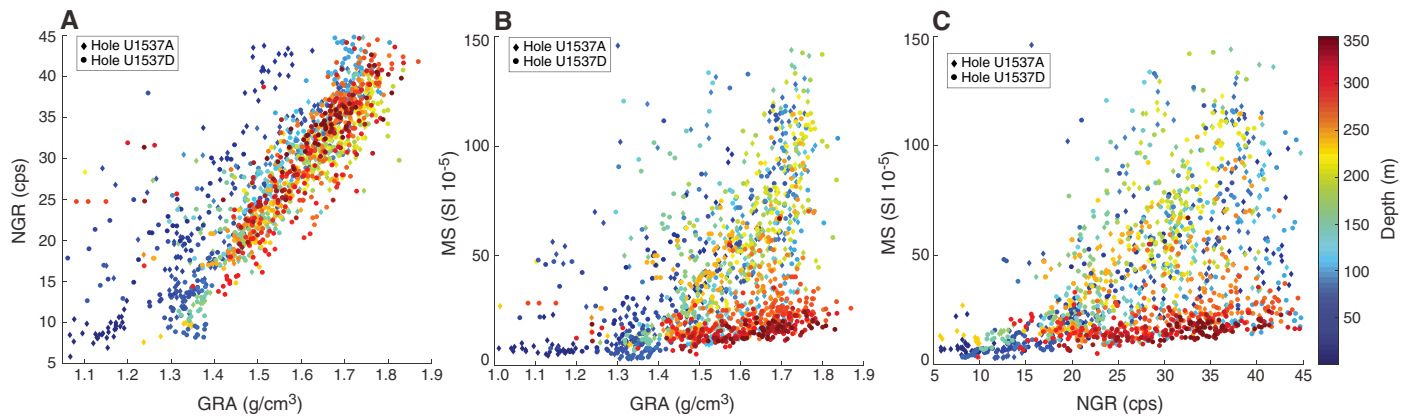


Figure F39. Crossplots and linear relationships of NGR, GRA, and MS, Holes U1537A and U1537D.

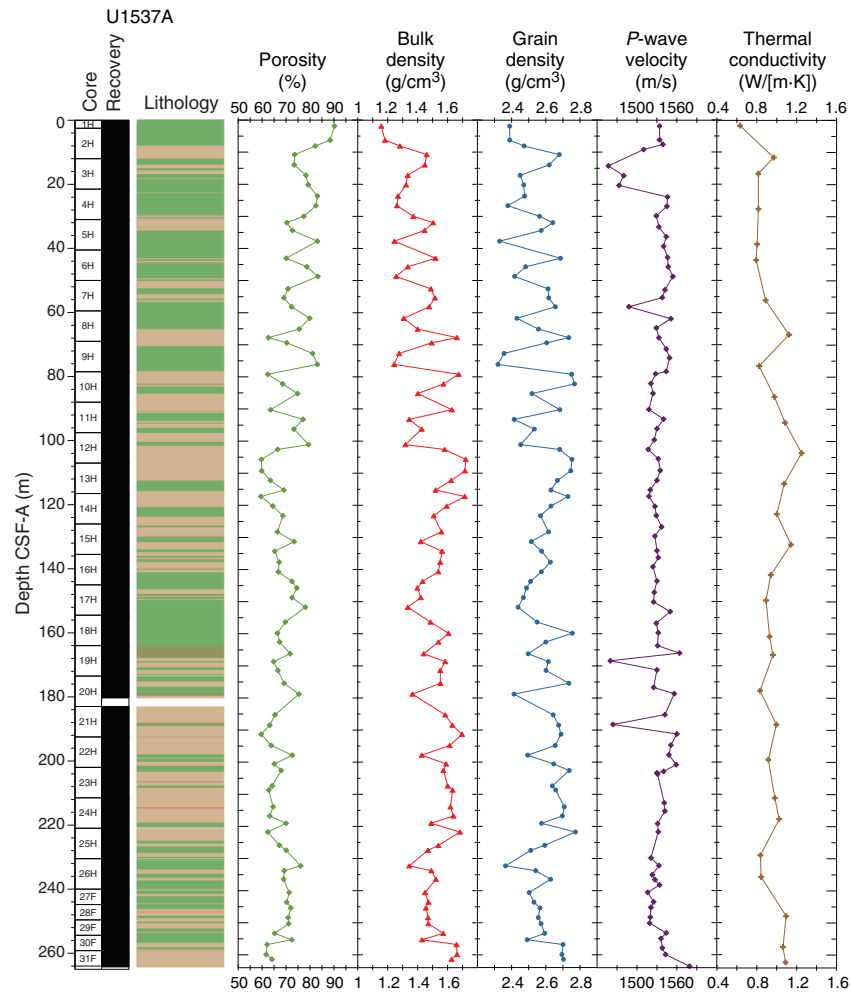


coupling required the instrument operator to manually determine a PWC value.

Downhole PWC measurements from Holes U1537A and U1537D are not consistent with WRMSL PWL values (Figures F37, F38). From the top of Hole U1537A to ~175 mbsf, *P*-wave values

measured with the PWC are ~10 to 40 m/s higher than those from the PWL. We observe a similar offset between 0 and ~200 mbsf in Hole U1537D. The reason for this inconsistency is unclear. Hole U1537D PWC measurements made between 4 and 263 mbsf are mostly consistent with Hole U1537A PWC measurements made at



Figure F40. MAD results, Hole U1537A. *P*-wave velocity = caliper velocity measurements with automatic and manually picked first arrival times.

the same stratigraphic interval (6–263 mbsf). The exception is between ~210 and 250 mbsf, where average Hole U1537D *P*-wave values are higher than average Hole U1537A *P*-wave values at the same stratigraphic interval. An overall downhole increase in PWC measurements occurs for Holes U1537A and U1537D; values range from ~1500 to ~1580 m/s between the top of the each hole and 263 mbsf. Below 263 mbsf and through the remainder of Hole U1537D, *P*-wave velocity values become more variable, ranging from ~1500 to ~1600 m/s.

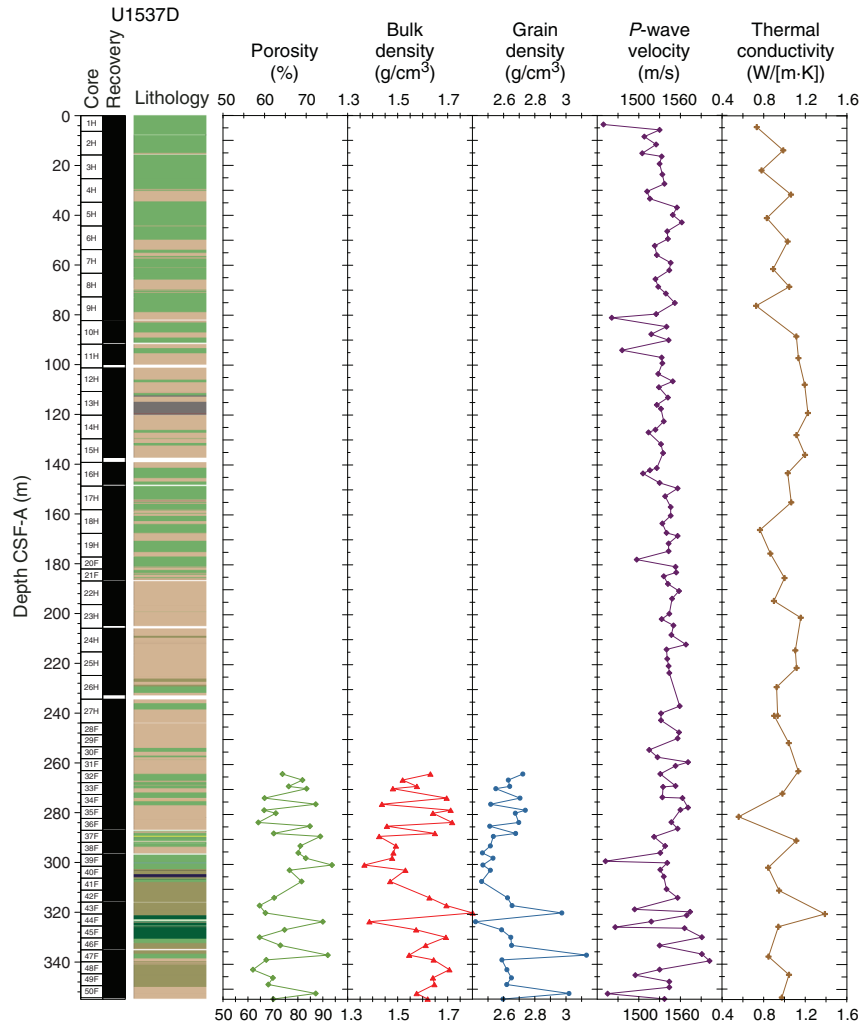
### Moisture and density

Bulk density values were calculated from moisture and volume measurements made on discrete samples taken from the working halves (see **Physical properties** in the Expedition 382 methods chapter [Weber et al., 2021a]). The sample resolution in each core varied depending on lithology, recovery, and quality, and at least three samples per APC core and two samples per HLAPC core were taken. A total of 117 samples were taken for MAD estimates: 85 from Hole U1537A and 32 from Hole U1537D.

MAD density values generally agree with GRA bulk density values measured on the WRMSL. Bulk density values for the stratigraphic sequence comprising Holes U1537A and U1537D range from ~1.2 to ~1.7 g/cm<sup>3</sup> and demonstrate an overall downhole increase. Bulk density values increase steadily through Hole U1537A,

ranging from ~1.2 g/cm<sup>3</sup> at the top of the hole to ~1.7 g/cm<sup>3</sup> at the bottom of the hole (261 mbsf). Bulk density values are variable through the entire hole, fluctuating ~0.2–0.4 g/cm<sup>3</sup> every ~10 m. Variability in bulk density is consistent with lithologic changes between silty clay and diatom ooze. Bulk density values at the top of Hole U1537D are consistent with bulk density values at the bottom of Hole U1537A. Hole U1537D bulk density values range from ~1.3 to 1.8 g/cm<sup>3</sup> and exhibit the same degree of variability observed in Hole U1537A.

The overall downhole trend in grain density values observed in Holes U1537A and U1537D (Figures F40, F41) follows that observed in the bulk density values. However, a greater degree of variability is observed in the grain density signal. Grain density values range from ~2.3 to ~2.8 g/cm<sup>3</sup>. A few individual values in the lowest part of Hole U1537D exceed 3 g/cm<sup>3</sup>. The majority of the signal observed in Hole U1537A demonstrates fluctuations of ~0.2–0.4 g/cm<sup>3</sup> every ~10 m; from ~100 to ~150 mbsf, it varies only by ~0.1 g/cm<sup>3</sup> every ~10 m. This decreased variability correlates with a zone of lower amplitude variations documented for other physical properties. Hole U1537D grain density values, only measured in the lowermost part, exhibit greater scatter, ranging from 2.4 to 3.1 g/cm<sup>3</sup>. Grain density values measured at the top of Hole U1537D are consistent with grain density values measured at the base of Hole U1537A.

Figure F41. MAD results, Hole U1537D. *P*-wave velocity = caliper velocity measurements with automatic and manually picked first arrival times.

Porosity (percent of pore space of the wet sediment volume) is included in the suite of MAD measurements and indicates a general decrease in volume percent (Figures F40, F41) due to downcore compression. Discrete porosity values range from ~60% to ~90% through the entire Site U1537 sequence. Relatively high porosity values at the top of the sequence are consistent with the presence of biosilica-rich muds. Hole U1537A porosity values decrease from ~90% near the top of the hole to ~65% at the bottom of the hole; Hole U1537D porosity values range from 90% to 65% and are consistent with porosity values observed at the bottom of Hole U1537A.

### Color reflectance

$L^*a^*b^*$  color reflectance measurements describe coordinates in a spherical system with 16.8 million possible variations (Weber, 1998; Blum, 1997). All color components show cyclic variability downcore in phase with lithologic changes. However, all signals appear to be rather noisy. The  $L^*$  axis measures the black–white color component and is known as the lightness or gray value. It is a reliable tracer for the content of biogenic carbonate in marine sediment (Weber, 1998).  $L^*$  values for Holes U1537A and U1537D increase slightly downhole (Figures F42, F43).

The  $a^*$  axis is the green–red component and is usually a tracer of changing redox conditions in the sediments. For Holes U1537A and

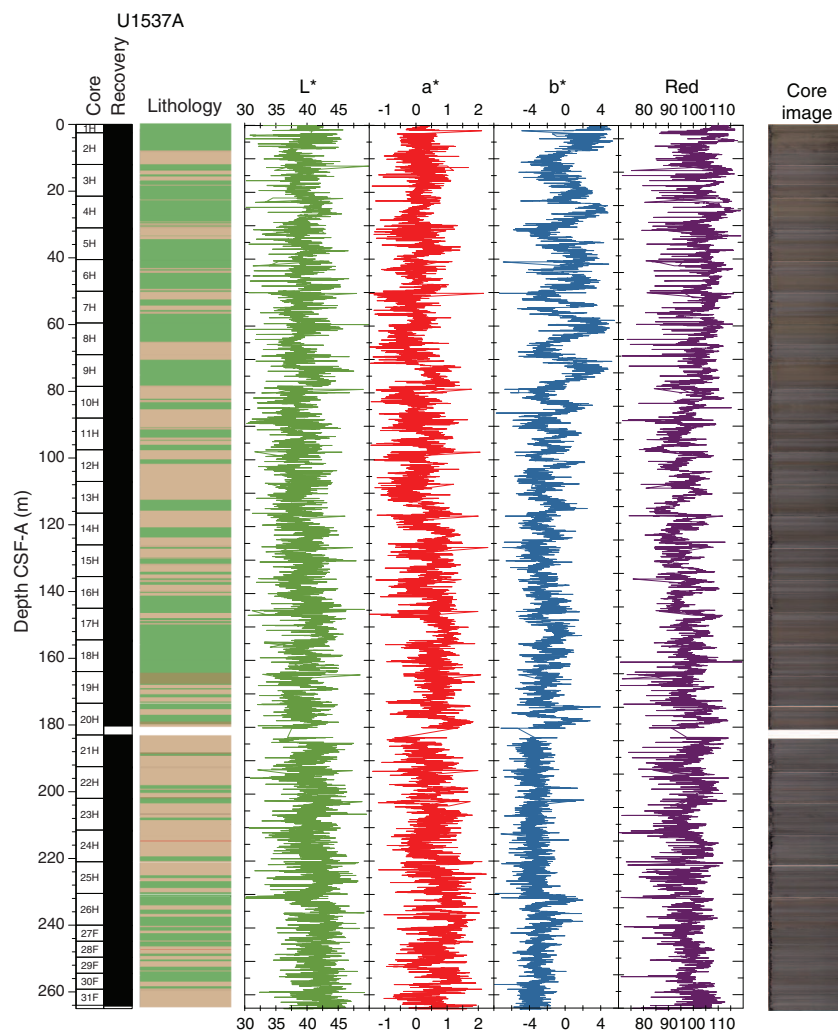
U1537D,  $a^*$  values are low and present little amplitude variation along the entire hole with a slight increasing trend.

The  $b^*$  axis is the yellow–blue component, and it is a proxy for the relative opal content in cores from the Scotia Sea (Sprenk et al., 2013). More positive values (yellowish colors) correspond to higher opal (usually diatoms) contents. The decreasing downhole trend documented for this component reaches a low in Core 382-U1537D-21F; below this core, variability is low. The highest values are found in Core 7H.

### Physical properties and relationship with facies

In general, the sediments at Site U1537 are composed of greenish gray diatom-bearing/rich silty clay and greenish gray clay-bearing diatom ooze with low carbonate and TOC contents. The silty clays are generally associated with higher MS, NGR, and density and lower *P*-wave velocity and  $b^*$  sediment color. Glauconite is present, and variations in its abundance likely play a strong role in controlling changes in sediment color and lightness.

The Pliocene–Pleistocene stratigraphy at Site U1537 is divided into two units. Lithostratigraphic Unit I (middle and late Pleistocene) spans the uppermost ~180 m and consists of interbedded silty clay and diatom ooze with highly variable MS, NGR, density, *P*-wave velocity, and  $b^*$  color. Lithostratigraphic Unit II (early Pleisto-

Figure F42. SHMSL color reflectance  $L^*$ ,  $a^*$ , and  $b^*$  and color component R, Hole U1537A.

cene) spans ~180–348 mbsf and consists largely of diatom-bearing/rich silty clay. Unit II is characterized by higher baseline MS values from ~180 to 288 mbsf, and between ~288 and 348 mbsf values of MS and the amplitude of MS variability are lower. Also, at 180–235 mbsf we observe higher but more muted NGR and GRA density values and lower  $b^*$  color values.

It is most likely that changes in the physical properties of these units are a product of variations in the proportion of their biogenic components (dominantly diatom opal) and terrigenous content (mostly clay). In the case of MS, variations in these data are controlled by dilution of the terrigenous magnetic carrier by diamagnetic biogenic opal. This signal is further modulated by variations in the input of at least two distinct populations of magnetic minerals: lower coercivity magnetic minerals that appear to be associated with MS lows and higher coercivity magnetic minerals that appear to be associated with MS highs (see [Paleomagnetism](#)).

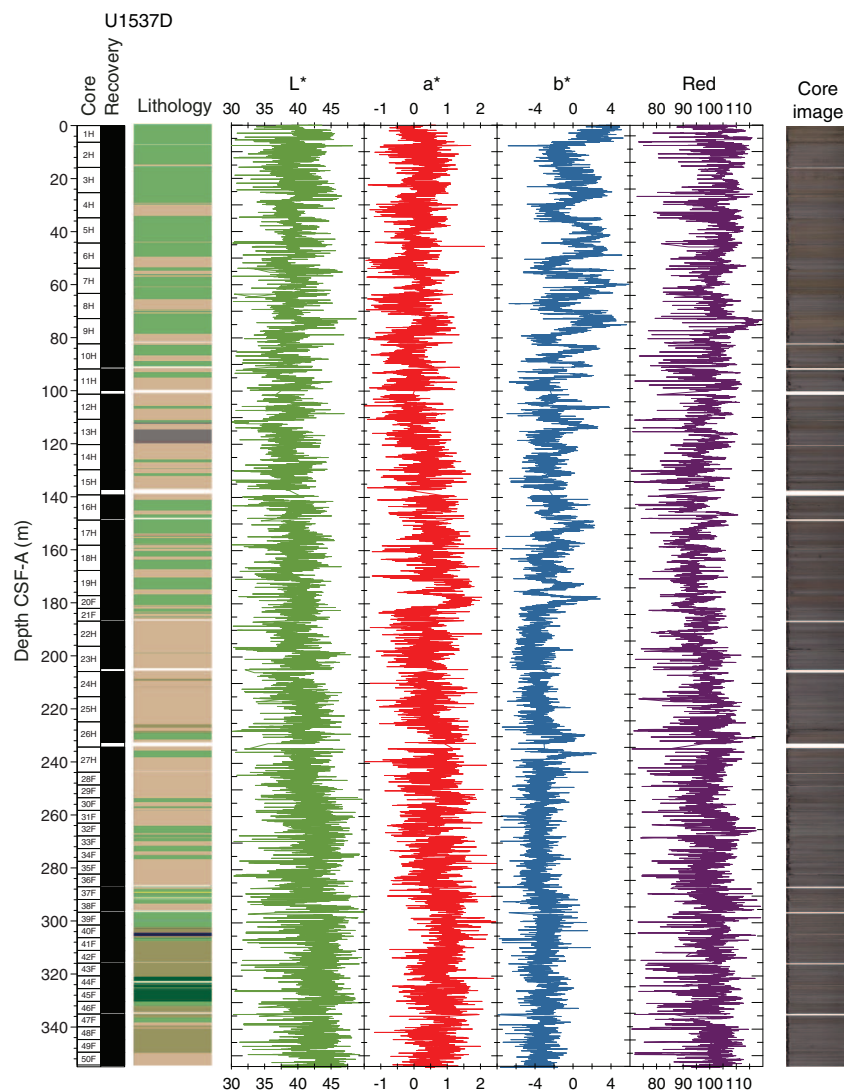
### Core disturbances and data quality

Core recovery was typically 100% in all holes at Site U1537. All physical property measurements were possible without major gaps except for Core 382-U1537A-20H and Cores 382-U1537D-15H and 26H. PWL measurements show spikes from Core 382-U1537A-21H downhole and from Core 382-U1537D-31F downhole. Hole U1537A contains a number of cores that were excluded from con-

sideration for affine ties in stratigraphic correlation because of core disturbance such as flow-in. Also, a large number of cores contain evidence of the slumped intervals observed in the seismic sections around Core 382-U1537D-37F and downhole. Core disturbances such as uparching of layers did not diminish the quality of the physical property data in a way that prevents meaningful core-seismic integration in the splice, but a few flow-in cases do.

### Summary

Physical property data were acquired on all cores from Site U1537 using the WRMSL for GRA wet bulk density, MS, and  $P$ -wave velocity (PWL). We also measured NGR in all sections longer than 50 cm. Once the whole rounds were split in two halves, we acquired X-ray imaging on all the archive halves and measured thermal conductivity in one section per core. The SHMSL was then used to measure MSP and color reflectance using the  $L^*a^*b^*$  color system, and the red-green-blue (RGB) color of the sediments was measured with digital color imaging (SHIL). In addition, we determined  $P$ -wave velocity values at discrete points on the working halves for all cores from Site U1537 and measured discrete samples for MAD of wet bulk density, dry bulk density, and grain density for Holes U1537A and U1537D. The sensors worked correctly, and the data are of good quality.

Figure F43. SHMSL color reflectance  $L^*$ ,  $a^*$ , and  $b^*$  and color component Red, Hole U1537D.

Diatom ooze and silty clay dominate the lithology for the upper 300 m, whereas interbedded silty clay and diatom ooze together with interbedded silty clay and biosiliceous ooze dominate the underlying sediment column (300–354 mbsf). Prominent variations in physical property signals are observed where the lithology varies within the core, such as in Core 382-U1537A-7H, whereas more uniform lithologies are reflected in more monotonous physical property signals. Diatom-dominated lithologies have lower NGR, density,  $P$ -wave velocity ( $V_p$ ), and MS and higher  $b^*$  values than silty clay-dominated lithologies. Accordingly, the physical properties obtained for Holes U1537A–U1537D provide valid and reproducible information on sediment composition and variability for all cores. All the physical property records show characteristic 1–10 m scale variations that are very likely to reflect the characteristic orbital-scale cyclicity of the Pleistocene and Pliocene.

## Stratigraphic correlation

Stratigraphic correlation relied on whole-round cores from Holes U1537A–U1537D. The cores were analyzed for physical properties at a 2.5 cm resolution using the WRMSL (for MS, GRA density, and  $P$ -wave velocity) and gamma ray track (for NGR intensity). They were analyzed using the SHMSL (for MS and color reflectance) after they were split into working and archive halves (see [Physical properties](#); also see [Physical properties](#) in the Expedition 382 methods chapter [Weber et al., 2021a] for details). All core physical properties were determined after the cores had warmed up to room temperature. However, to minimize coring gap alignment, the MS of many of the cores was determined at a 2.5 cm resolution on the WRMSL in near-real time in advance of their reaching room temperature because tests showed minimal difference between MS measured at the initial temperature versus room temperature.

### Correlation between holes

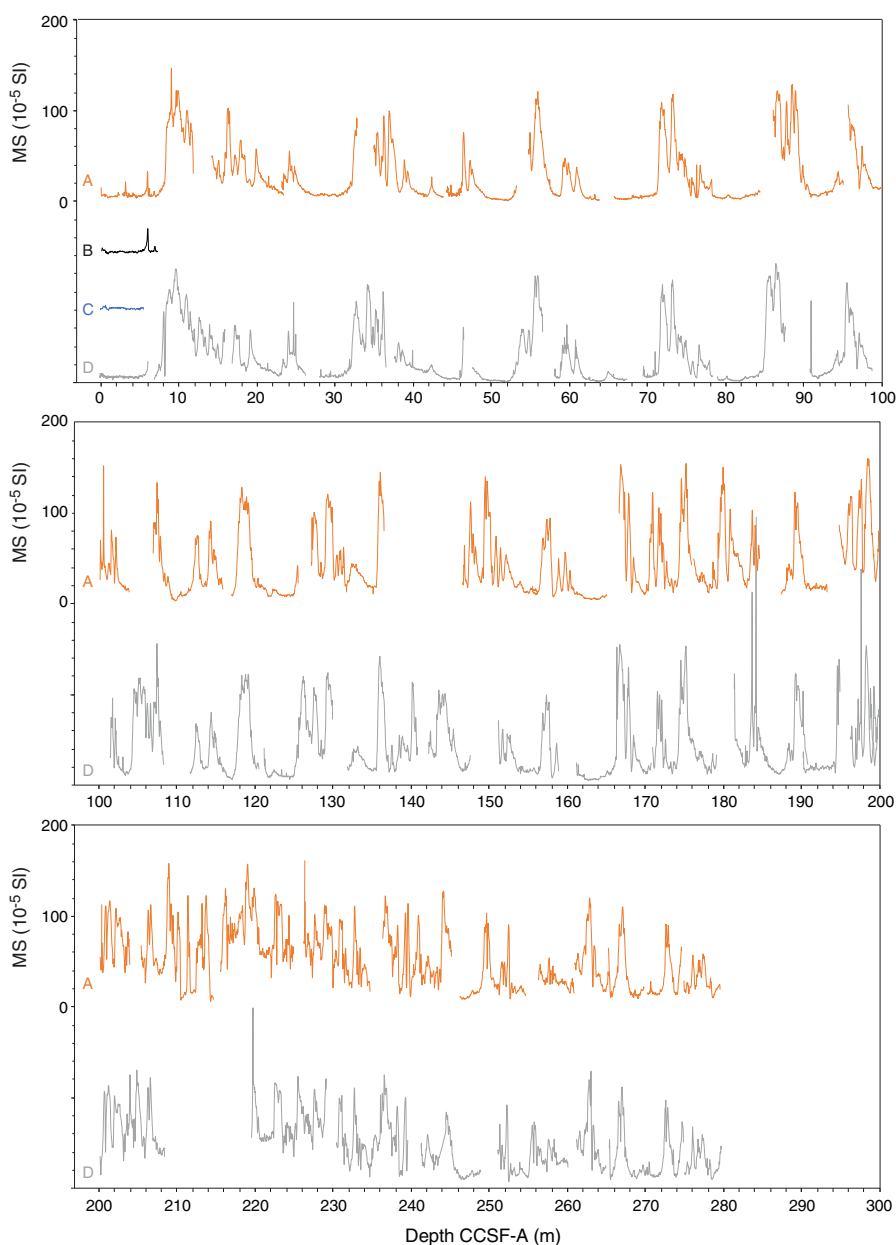
The top of Hole U1537B preserved the best mudline and was the longest first core in all four holes, so it served as the anchor (zero depth point) for generating the CCSF-A depth scale at this site (see **Stratigraphic correlation** in the Expedition 382 methods chapter [Weber et al., 2021a] for an explanation of depth scales). We attempted to establish the relative depth offset of each core from this reference by establishing affine ties between cores from Holes U1537A–U1537D based on the optimized correlation of predominantly WRMSL-derived MS and GRA density data and in one case magnetic inclination data derived following peak AF demagnetization at 15 mT (between Cores 382-U1537A-16H and 382-U1537D-15H). These depth offsets (or affine ties) are reported in Table T20,

and the resulting MS correlations are shown in Figure F44. We were able to establish two affine ties for all but three cores (382-U1537D-20F and 21F, which bridge a hardground that even the HLAPC system could not penetrate, and Core 23H, which corresponded to a sediment slump) to the CCSF-A depth scale above 244 mbsf. This success can be attributed to (1) the excellent offset maintained between APC coring depths in Holes U1537A and U1537D over this interval (to Cores 382-U1537A-27F and 382-U1537D-27H) and (2) the excellent quality of Hole U1537A cores, which were recovered during calm ocean conditions.

The affine tie between Cores 382-U1537A-16H and 382-U1537D-15H, which was established using magnetic inclination data, requires confirmation with postcruise X-ray fluorescence (XRF) core scanning. The core breaks between Holes U1537A and U1537D nearly line up at this depth in these two cores because of incomplete recovery for Core 382-U1537D-15H (only 78%). Until

Table T20. Splice offsets, Site U1537. [Download table in CSV format.](#)

Figure F44. MS data, Site U1537.





XRF core scanning is performed, this affine tie should be used with caution. Otherwise, we have high confidence in all affine ties reported here. It is also worth stating that coring artifacts (such as postcoring expansion and/or stretching and compression, in particular, of Sections 1 and 7), as well as small differences in sedimentation rates between cores, mean that single depth offsets derived from affine ties will result in inevitable misalignment of features at CCSF-A depths that can otherwise confidently be correlated visually between holes. This misalignment is an essential consideration for sampling out of the splice and for the use of age data based on, for instance, shipboard micropaleontology (nearly all of which were derived from Hole U1537A core catchers that fall out of the splice).

### Construction of the splice

Once the composite depth scale was created, selected sequences from Holes U1537A, U1537B, and U1537D were spliced together to create the most complete and representative section possible (Figure F45). We strove to have as much of Hole U1537A in our primary splice as possible because it is exceptionally well preserved. Detailed sedimentological logs and archive-half X-ray images were consulted during the process of splice construction to avoid the inclusion of any significantly disturbed intervals and/or sections with unique features (relative to the other holes). The end product is reported in Table T21.

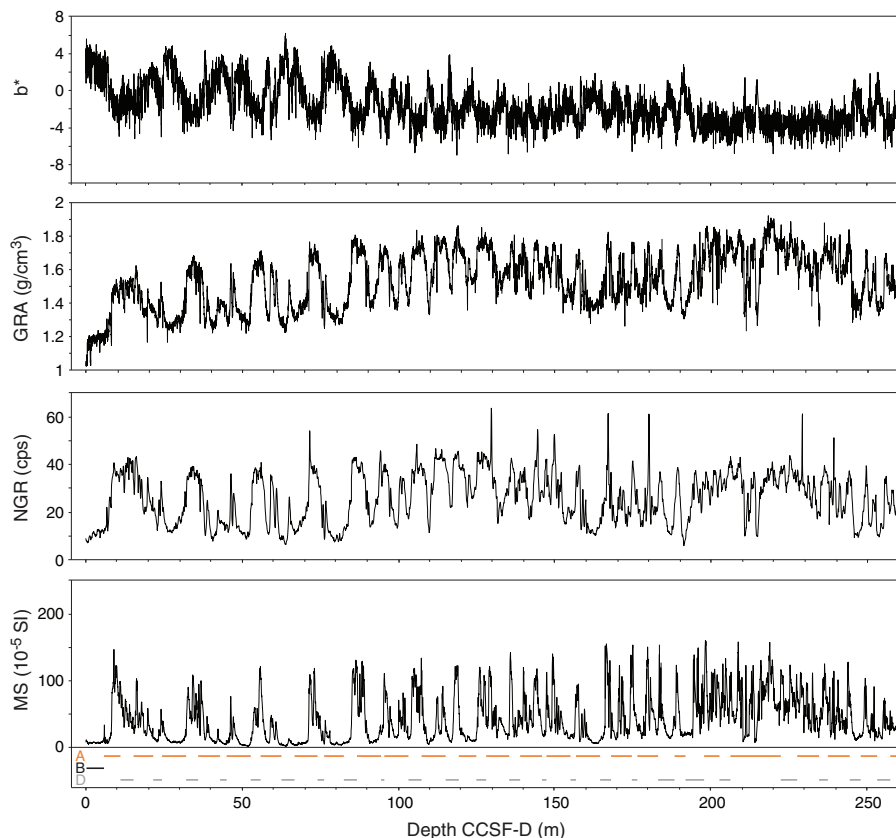
The primary splice for Site U1537 spans 0–259 m core composite depth below seafloor, Method D (CCSF-D). It is based predominantly on the correlation of sediment MS and GRA density data. Section 382-U1537D-26H-5 was reported as “pumped out of bar-

rel—possibly out of stratigraphic order.” We could not avoid including this section in our splice, but our affine tie for the core it is part of and the comparison of its physical property data to Hole U1537A suggest that the stratigraphy in this section is likely sound. Overall, Hole U1537A makes up ~66% of the splice, Hole U1537B makes up ~2% (the mudline), and Hole U1537C makes up ~32%.

The splice contains two appends: (1) one append at 194.96 m CCSF-D (Core 382-U1537D-21F onto Core 20F because of our inability to recover the hardground at ~180 mbsf; the very base of Section 20F-4 contains evidence for flow-in spanning 47–65 cm likely caused by this impenetrable barrier and should not be sampled) and (2) a second append at 214.69 m CCSF-D (Core 382-U1537A-23H onto Core 22H because of primary sedimentological slumping that could not be avoided in the splice). In both cases, the average affine-guided growth of the composite section for the top ~194 m CCSF-D of the splice (~1.07, or 7%) was used to establish the size of the affine offset for these appends. Below 259 m CCSF-D, we observed correlation between all cores in Holes U1537A and U1537D where overlap in coring depths exist, but this correlation is not sufficient to warrant constructing an additional continuous floating splice. Below 259 m CCSF-D (Core 382-U1537A-27F), we appended a small chain of cores from Holes U1537A and U1537D using these affine ties to Hole U1537D at 288.78 m CCSF-D. Those interested in working on deeper cores should append Hole U1537D cores (from Core 382-U1537D-33F) from this point to establish a working stratigraphy.

Table T21. Splice ties, Site U1537. [Download table in CSV format.](#)

Figure F45. Spliced record of color  $b^*$ , GRA density, NGR intensity, and MS, Site U1537. Sections used to construct spliced records are shown at base of figure (see Table T21).



## Comparison of stratigraphies between Sites U1536 and U1537

A comparison of the Site U1537 stratigraphy to that of nearby Site U1536 (Figure F46; Table T22) highlights four important observations:

Figure F46. Comparison of spliced stratigraphies, Sites U1537 and U1536. NGR intensity data shown on Site U1537 CCSF-D scale after manual graphic correlation of the two records (see Table T22). Site U1536 data are offset vertically from y-axis values. Gray bars = two slumped intervals in Site U1536 stratigraphy. Based on correlation shown, we infer that the lower slump adds an erroneous physical property cycle to Site U1536, whereas the upper slump appears to obstruct one physical property cycle preserved in Site U1537 stratigraphy. Black and white horizontal bars at base of figure denote GPTS2012 interpretation of Site U1537 magnetochronostratigraphy (see Paleomagnetism). B/M = Brunhes/Matuyama boundary (0.781 Ma), J = Jaramillo (0.99–10.7 Ma), O = Olduvai (1.78–1.95 Ma), R = Reunion (2.13–2.15 Ma). Annotated arrows along top of figure = depth relationships of corresponding magnetostratigraphic reversals in Site U1536 stratigraphy to Site U1537 NGR record confirming that ties established between the two stratigraphies are plausible.

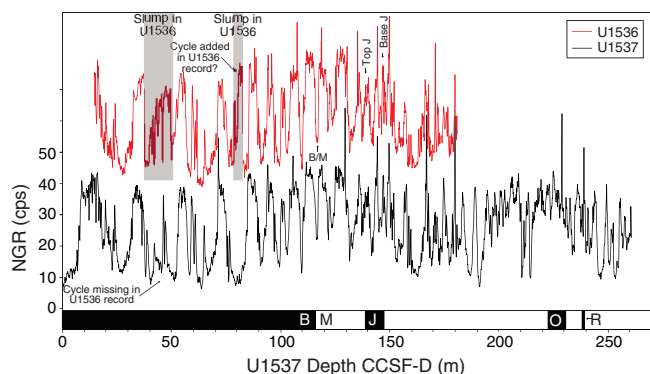


Table T22. Correlation tie points between splices, Sites U1536 and U1537. [Download table in CSV format.](#)

- Remarkable similarities exist between both records.
- Both records contain a complete high-resolution mid-Pleistocene stratigraphy.
- Sedimentation rates are higher at Site U1536 than Site U1537.
- The lower slump reported at Site U1536 (~95.90–99.31 m CCSF-D in Core 382-U1536A-11H) likely adds repeated stratigraphy to the record, whereas the uppermost slump reported at Site U1536 (~50.74–56.34 m CCSF-D in Core 382-U1536B-7H) likely eroded an interglacial–glacial cycle that is preserved in the Site U1537 stratigraphy.

The correlation between Sites U1537 and U1538 is discussed in [Stratigraphic correlation](#) in the Site U1538 chapter (Weber et al., 2021c).

## Downhole measurements

### Downhole temperature and heat flow

Advanced piston corer temperature tool (APCT-3) downhole temperature measurements were made in Holes U1537A (Cores 382-U1537A-4H, 7H, 10H, 13H, and 16H) and U1537D (Core 382-U1537D-5H). The seafloor temperature was determined to be  $-0.2^{\circ}\text{C}$  based on APCT-3 data taken while the tool was held at the mudline for 5 min during each run (Figure F47). The measurement on Core 382-U1537A-4H did not yield reliable results. The obtained temperatures range from  $2.91^{\circ}\text{C}$  at 31 mbsf to  $12^{\circ}\text{C}$  at 164 mbsf (Table T23; Figures F47, F48), giving an approximately linear temperature increase with depth and a geothermal gradient of  $69^{\circ}\text{C}/\text{km}$ .

Thermal conductivity under in situ conditions was estimated from laboratory-determined thermal conductivity for Holes U1537A and U1537D using the method of Hyndman et al. (1974) (see [Physical properties](#) in the Expedition 382 methods chapter [Weber et al., 2021a]). The calculated in situ values are within 2% of the measured laboratory values. Thermal resistance was calculated by integrating the inverse of the in situ thermal conductivity over depth. Considering all thermal conductivity measurements down the holes for Site U1537, a heat flow of  $69 \text{ mW}/\text{m}^2$  was estimated from the linear fit between temperature and thermal resistance following the method of Pribnow et al. (2000).

Figure F47. APCT-3 temperature-time series, Site U1537.

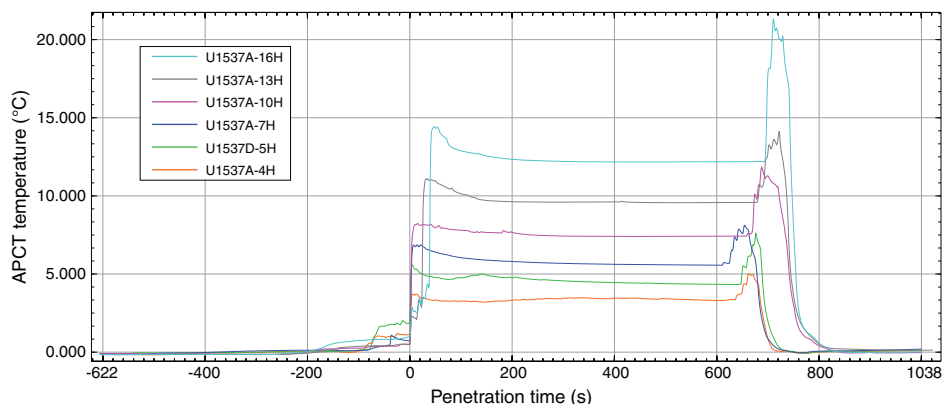
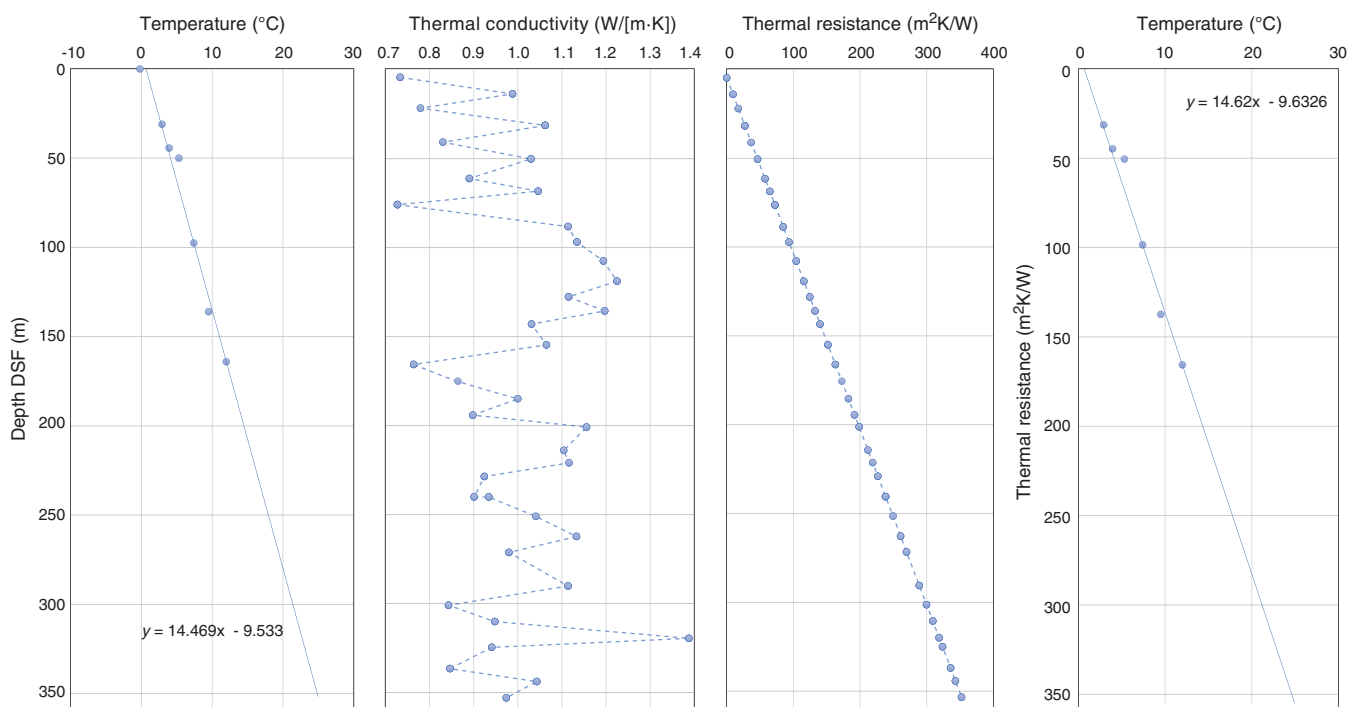


Table T23. Formation temperatures derived from APCT-3 measurements, Holes U1537A and U1537D. APCT-3 = advanced piston corer temperature tool. [Download table in CSV format.](#)

Hole, core	APCT-3 depth DSF (m)	Temperature (°C)	Quality	Comments
382-				
Seafloor	0.0	-0.2		
U1537A-4H	31.0	2.91	Bad	
U1537D-5H	44.3	3.93	Bad	
U1537A-7H	50.0	5.3	Good	
U1537A-10H	97.5	7.4	Fair	
U1537A-13H	136.0	9.5	Fair	
U1537A-16H	164.0	12	Good	Possible solutions in range 11.6–12.3

Figure F48. Heat flow calculation, Site U1537. Right panel shows Bullard plot of heat flow calculated from linear fit of temperature data. DSF = drilling depth below seafloor.



### Core-log-seismic integration

The regional sedimentary record of the Scotia Sea consists of five easily distinguishable seismic units (V–I in upward stratigraphic order). They are bounded by four stratigraphic discontinuities (Reflectors d–a from bottom to top) (e.g., Maldonado et al., 2006; Martos et al., 2013; Pérez et al., 2017). In some of the local basins of the Scotia Sea, an additional stratigraphic discontinuity has been identified in Unit I and named Reflector a' (Pérez et al., 2017). For the purposes of this report, Reflector a' divides Unit I into Subunits Ib and Ia from bottom to top. At Site U1537, we recovered the two uppermost units of the regional sedimentary record (Units II and I). The physical properties measured on the cores from Site U1537, MCS Line SCAN2004-L07, and echo sounder topographic parametric sonar (TOPAS) Profile SCAN2004-L07 are integrated in this section (Figures F49, F50, F51, F52).

Correlation of the seismic signal with depth in the hole uses a velocity model based on the discrete PWC velocity measurements. We note that some expected uncertainty occurs in the velocity

model. Velocity tends to be faster under in situ conditions compared to velocity measurements after core expansion, but the magnitude of this effect at this site is not known. If the velocity model underestimates the in situ velocity, then a seismic reflector will appear at a shallower depth than if an in situ velocity was used. The uncertainty in reflector depth assignment is likely to be small in the upper few 100 m of the hole but would increase in the deeper parts of the hole.

The physical properties and age models obtained during Expedition 382 allow us to constrain the age ranges of previously identified seismic units and develop an age model for the stratigraphic discontinuities (Table T24).

### Physical properties and relationship with multichannel seismic interpretation

MCS Line SCAN2004-L07 allows the identification of seismic units at Site U1537. APC and HLAPC coring recovered a record to 354.3 mbsf at Site U1537 that retrieves the two uppermost seismic units of the regional sedimentary record of the Scotia Sea (Units II

Figure F49. Physical property measurements and comparison with MCS Profile SCAN2004-L07, Holes U1537A and U1537D. MAD = wet bulk density, yellow line = PWL trend. MD = measured depth.

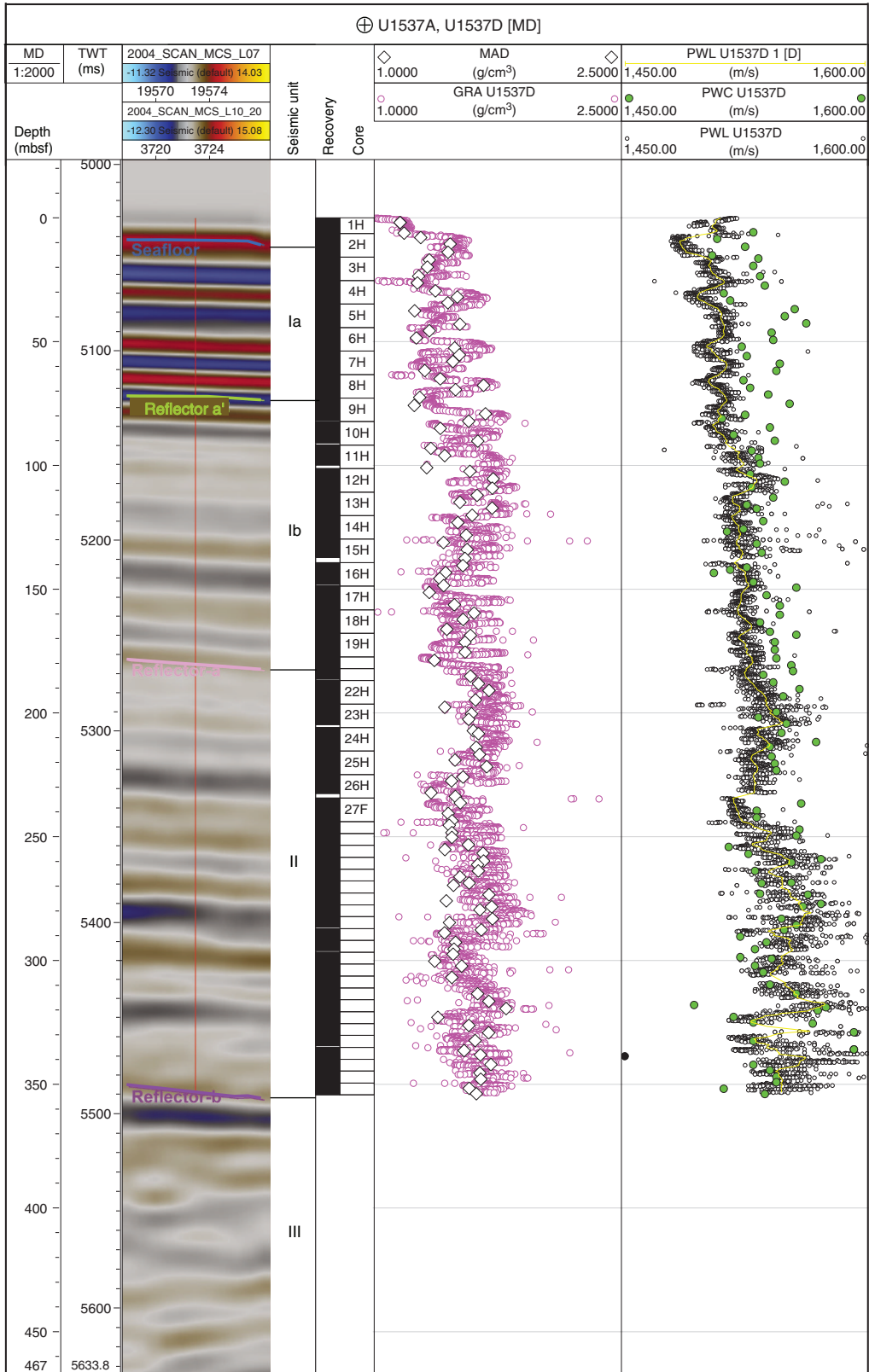
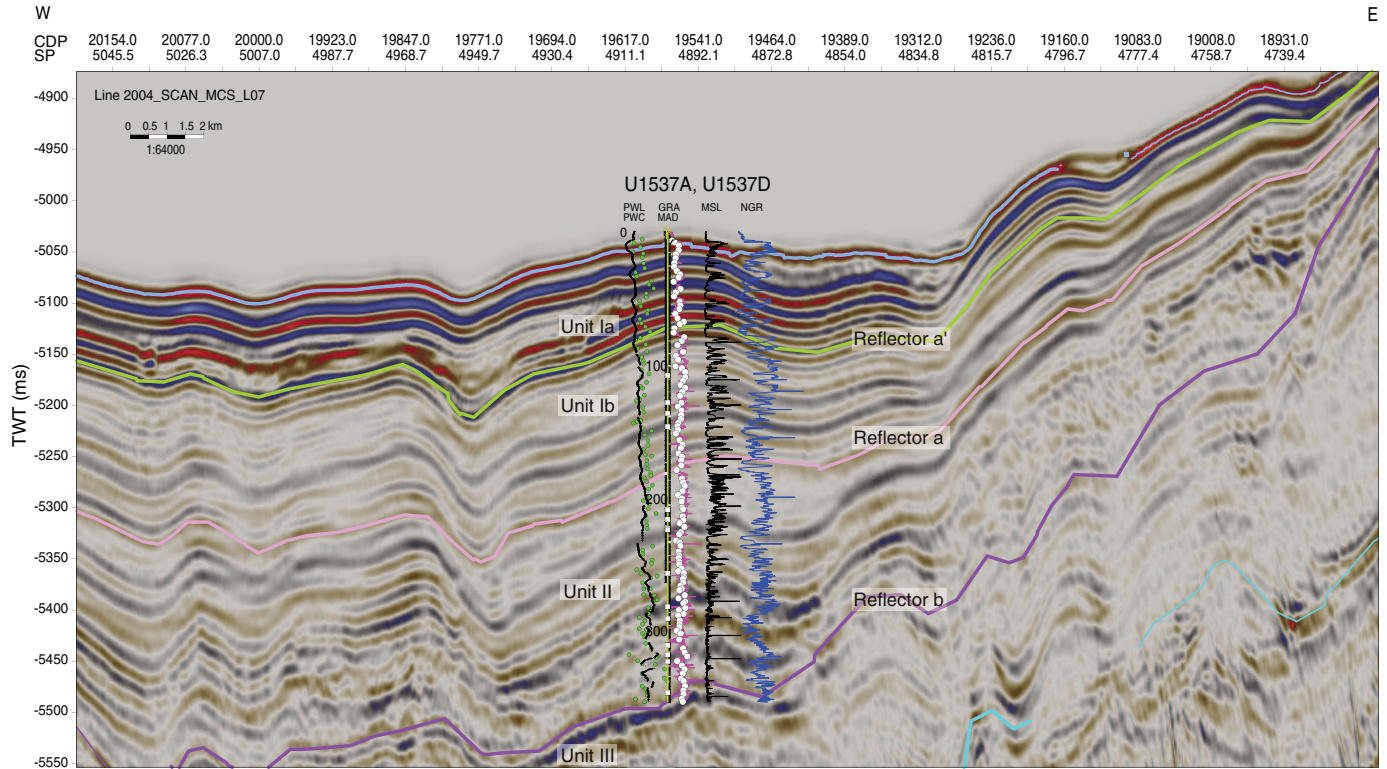




Figure F50. MCS Profile SCAN2004-L07 and physical properties, Holes U1537A and U1537D. Green dots = PWC, black line = PWL, magenta line = GRA, open dots = discrete wet bulk density (MAD), black line = MSL, blue line = NGR. CDP = common depth point, SP = shotpoint.



and I) (Maldonado et al., 2006; Martos et al., 2013; Pérez et al., 2017). Coring operations ended just above the regional stratigraphic discontinuity known as Reflector b located at 366 mbsf or 5488 ms two-way traveltime (TWT). All stratigraphic discontinuities, described here from bottom to top, represent marked changes in the seismic record and in physical properties measured on the cores in the laboratory. Details of core-log physical property variability at Site U1537 are described in detail in [Physical properties](#). Here, we focus on the comparison to seismic data and show overview figures only (Figures [F49](#), [F50](#)).

Unit II ranges from Reflector b to Reflector a (366–180 mbsf) and is divided into four zones with distinct physical property trends (from bottom to top):

- Loop magnetic susceptibility (MSL), GRA density, and NGR have relatively constant values in the deepest part of Unit II to 320 mbsf (Figure [F50](#)).
- Above 320 mbsf, MSL values remain fairly constant, although with transient peaks, whereas GRA density, and NGR show upward decreasing trends to 294 mbsf.
- Above 294 mbsf, MSL displays a narrow peak, whereas GRA density and NGR values increase for 13 m (294–281 mbsf). GRA density then decreases uphole to 229 mbsf, whereas MSL and NGR remain relatively constant uphole to 229 mbsf. An increase in the variability of the NGR signal occurs around 250 mbsf.
- In the uppermost part of Unit II (229–180 mbsf), the baselines of MSL, GRA density, and NGR are shifted toward higher values with respect to the underlying values.

The three lowest parts of Unit II correspond to high-amplitude and laterally continuous reflections (Figure [F50](#)). PWL and PWC

values decrease uphole in Unit II, with particularly higher values between the bottom of the unit and 240 mbsf. The uppermost part of Unit II corresponds to transparent chaotic seismic reflections.

The top of Unit II and bottom of Unit I is Reflector a, which is located at 180 mbsf, or 5265 ms TWT, in Core 382-U1537D-20F. Reflector a marks an increase in the amplitude of variability in MSL, NGR, and GRA density and a general decrease in *P*-wave velocity (Figure [F49](#)). Subunit Ib ranges from Reflector a to Reflector a' (180–72 mbsf). The lower part of Subunit Ib is characterized by an uphole increase in NGR values that correlates with high-amplitude lateral continuous reflections in the seismic record (see Figure [F37](#)). The upper part of Subunit Ib is characterized by a general uphole decrease in GRA density, PWL, and NGR values that coincides with low-amplitude reflections of low lateral continuity in the seismic profile.

Reflector a' is located at 72 mbsf or 5124 ms TWT between Cores 382-U1537D-8H and 9H. Above Reflector a', Subunit Ia shows a change toward higher amplitude and lower frequency variability in values of MSL, NGR, and GRA density (see Figure [F37](#)). PWL and PWC values also fluctuate within this unit, which is characterized by high-amplitude and laterally continuous reflections. However, the amplitude of PWL and PWC variation is less than that observed in Unit II.

### Physical properties and relationship with parametric echo sounder interpretation

TOPAS Profile SCAN2004-L07 at Site U1537 allows the recognition of the seismic reflections composing Subunit Ia, Reflector a', and most of Subunit Ib (Figures [F51](#), [F52](#)). However, the limited acoustic penetration does not allow the identification of Reflector a.

Figure F51. Physical property measurements and comparison with TOPAS Line SCAN2004-L07, Holes U1537A and U1537D. MAD = wet bulk density.

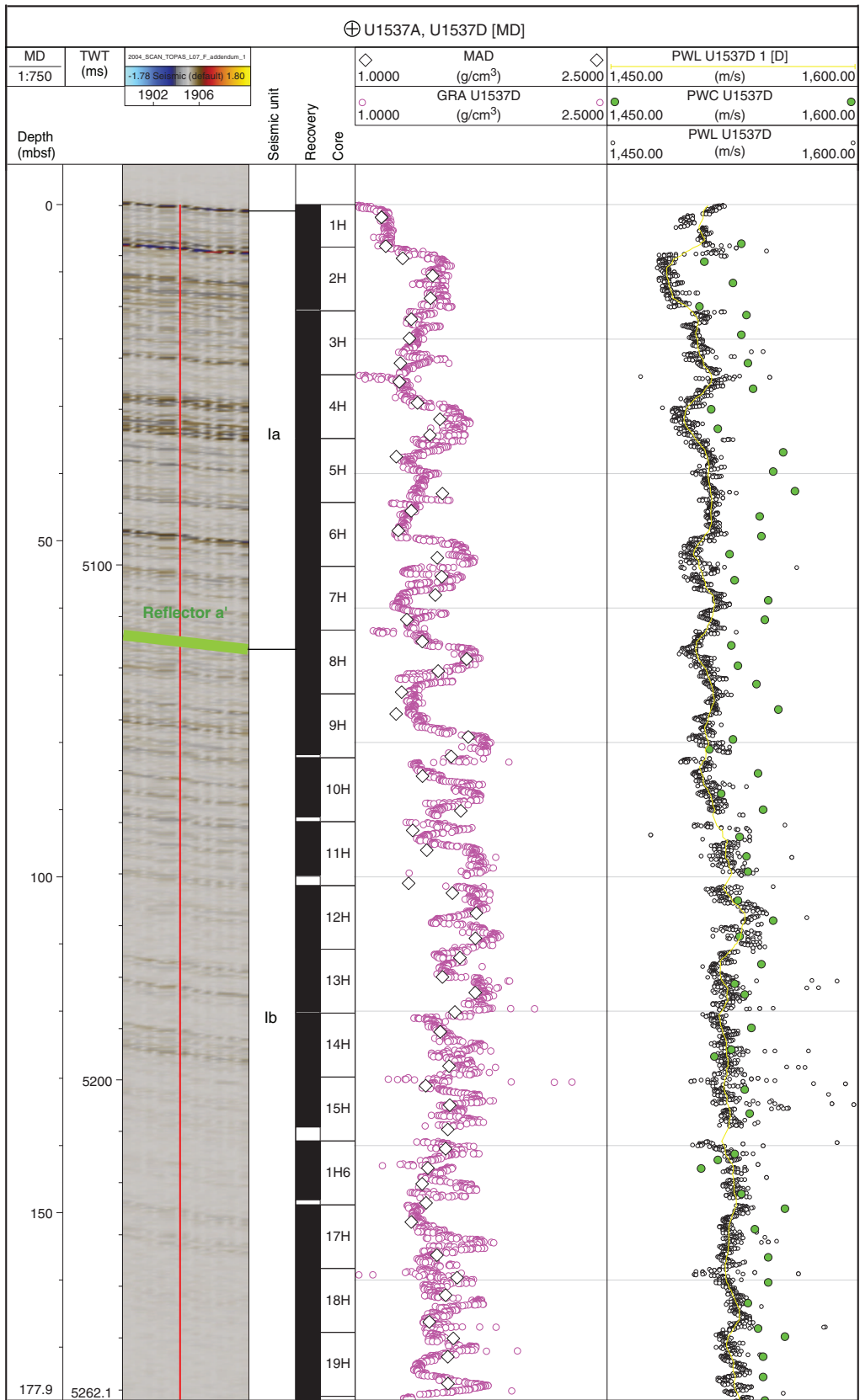


Figure F52. TOPAS Line SCAN2004-L07 and physical properties, Holes U1537A and U1537D. Green dots = PWC, black line = PWL, magenta line = GRA, open dots = discrete wet bulk density (MAD), black line = MSL, blue line = NGR.

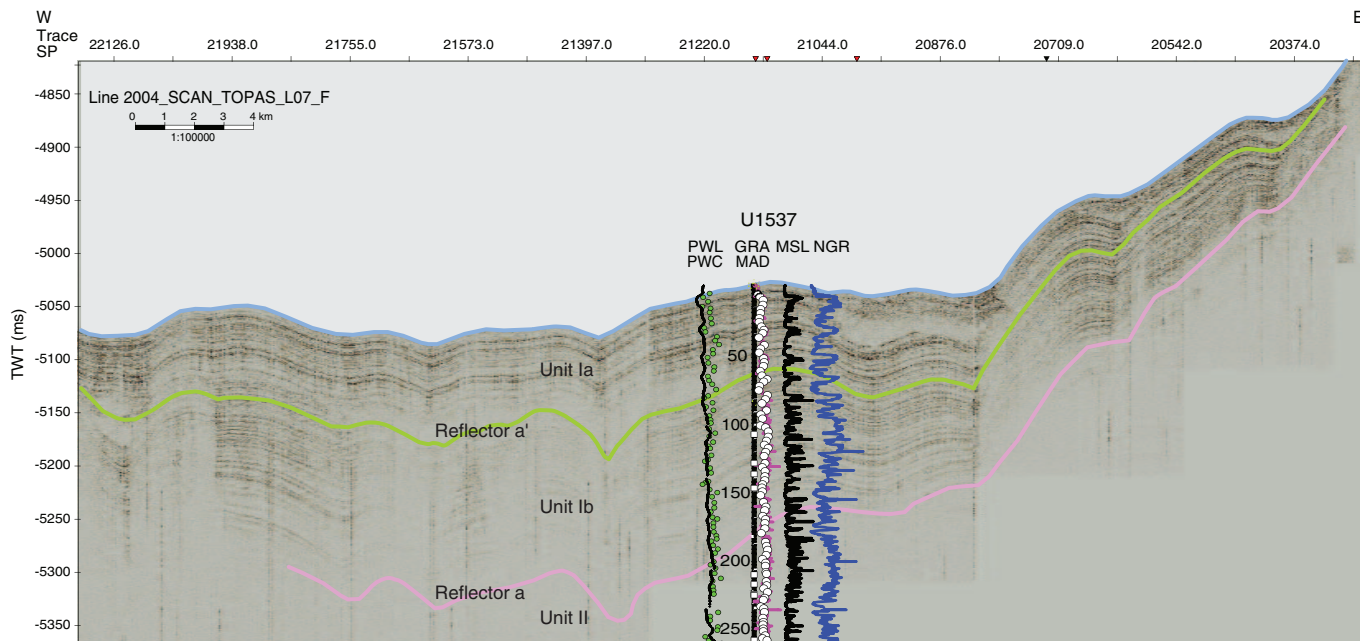


Table T24. Age model of main stratigraphic discontinuities, Site U1537. \* = determined by magnetostratigraphy, † = determined by biostratigraphy. TWT = two-way traveltime. — = not determined. [Download table in CSV format.](#)

Discontinuity	Depth TWT (ms)	Depth (m)	Core	Age (Ma)*	Age (Ma)†
Reflector a'	5124	72	382-U1537D-8H/9H	0.49	0.3
Reflector a	5265	180	20F	1.53	1.5–1.7
Reflector b	5488	—	—	—	4.5

The values of all the measured physical properties exhibit high-frequency variability in Subunit Ib with less than 10 m between the main peaks. Minimum MSL values and maximum PWL values correlate with high-frequency, medium-amplitude reflections. In Subunit Ia, all physical property values vary at a lower frequency and have a more distinct correlation with the reflections identified in the TOPAS profile. The variability identified in all physical properties corresponds to alternating patterns in the acoustic facies observed in the TOPAS record. The lows in P-wave velocity and peaks in GRA density, MSL, and NGR correspond to high-amplitude reflections in the TOPAS profile. High PWL values and low GRA density, MSL, and NGR values correspond to low-amplitude reflections in the TOPAS profile.

## References

Blum, P., 1997. *Technical Note 26: Physical Properties Handbook—A Guide to the Shipboard Measurement of Physical Properties of Deep-Sea Cores.* Ocean Drilling Program. <https://doi.org/10.2973/odp.tn.26.1997>

Dixit, S., Van Cappellen, P., and van Bennekom, A.J., 2001. Processes controlling solubility of biogenic silica and pore water build-up of silicic acid in marine sediments. *Marine Chemistry*, 73(3–4):333–352. [https://doi.org/10.1016/S0304-4203\(00\)00118-3](https://doi.org/10.1016/S0304-4203(00)00118-3)

Fisher, R., 1953. Dispersion on a sphere. *Proceedings of the Royal Society of London, Series A: Mathematical, Physical and Engineering Sciences*, 217(1130):295–305. <https://doi.org/10.1098/rspa.1953.0064>

Hyndman, R.D., Erickson, A.J., and Von Herzen, R.P., 1974. Geothermal measurements on DSDP Leg 26. *In* Davies, T.A., Luyendyk, B.P., et al., *Initial Reports of the Deep Sea Drilling Project*, 26: Washington, DC (U.S. Govt. Printing Office), 451–463. <https://doi.org/10.2973/dsdp.proc.26.113.1974>

Key, R.M., Olsen, A., van Heuven, S., Lauvset, S.K., Velo, A., Lin, X., Schirnick, C., et al., 2015. Global Ocean Data Analysis Project, Version 2 (GLODAPv2), ORNL/CDIAC-162, ND-P093. Oak Ridge, Tennessee (US Department of Energy). [https://doi.org/10.3334/CDIAC/OTG.NDP093\\_GLODAPv2](https://doi.org/10.3334/CDIAC/OTG.NDP093_GLODAPv2)

Maldonado, A., Barnolas, A., Bohoyoa, F., Galindo-Zaldívar, J., Hernández-Molina, J., Lobo, F., Rodríguez-Fernández, J., Somoza, L., and Vázquez, J.T., 2003. Contourite deposits in the central Scotia Sea: the importance of the Antarctic Circumpolar Current and the Weddell Gyre flows. *Palaeogeography, Palaeoclimatology, Palaeoecology*, 198(1–2):187–221. [https://doi.org/10.1016/S0031-0182\(03\)00401-2](https://doi.org/10.1016/S0031-0182(03)00401-2)

Maldonado, A., Bohoyo, F., Galindo-Zaldívar, J., Hernández-Molina, J., Jabañoy, A., Lobo, F.J., Rodríguez-Fernández, J., Suriñach, E., and Vázquez, J.T., 2006. Ocean basins near the Scotia–Antarctic plate boundary: influence of tectonics and paleoceanography on the Cenozoic deposits. *Marine Geophysical Researches*, 27(2):83–107. <https://doi.org/10.1007/s11001-006-9003-4>

Martos, Y.M., Maldonado, A., Lobo, F.J., Hernández-Molina, F.J., and Pérez, L.F., 2013. Tectonics and palaeoceanographic evolution recorded by contourite features in southern Drake Passage (Antarctica). *Marine Geology*, 343:76–91. <https://doi.org/10.1016/j.margeo.2013.06.015>

Olsen, A., Key, R.M., van Heuven, S., Lauvset, S.K., Velo, A., Lin, X., Schirnick, C., et al., 2016. The Global Ocean Data Analysis Project version 2 (GLODAPv2) – an internally consistent data product for the world ocean. *Earth System Science Data*, 8:2907–323. <https://doi.org/10.5194/essd-8-297-2016>

Pérez, L.F., Maldonado, A., Hernández-Molina, F.J., Lodolo, E., Bohoyo, F., and Galindo-Zaldívar, J., 2017. Tectonic and oceanographic control of sedimentary patterns in a small oceanic basin: Dove Basin (Scotia Sea, Antarctica). *Basin Research*, 29(S1):255–276. <https://doi.org/10.1111/bre.12148>



- Pribnow, D., Kinoshita, M., and Stein, C., 2000. *Thermal Data Collection and Heat Flow Recalculations for Ocean Drilling Program Legs 101–180*: Hanover, Germany (Institute for Joint Geoscientific Research, Institut für Geowissenschaftliche Gemeinschaftsaufgaben [GGA]).  
<http://www-odp.tamu.edu/publications/heatflow/ODPReprt.pdf>
- Sprenk, D., Weber, M.E., Kuhn, G., Rosén, P., Frank, M., Molina-Kescher, M., Liebetrau, V., and Röhlhng, H.-G., 2013. Southern Ocean bioproductivity during the last glacial cycle—new decadal-scale insight from the Scotia Sea. *Geological Society Special Publication*, 381(1):245–261.  
<https://doi.org/10.1144/SP381.17>
- Tauxe, L., 2010. *Essentials of Paleomagnetism*. With contributions by R.F. Butler, R. Van der Voo, and S.K. Banerjee: Berkeley, California (University of California Press).
- Weber, M.E., 1998. Estimation of biogenic carbonate and opal by continuous non-destructive measurements in deep-sea sediments: application to the eastern equatorial Pacific. *Deep-Sea Research, Part I: Oceanographic Research Papers*, 45(11):1955–1975.  
[https://doi.org/10.1016/S0967-0637\(98\)00028-4](https://doi.org/10.1016/S0967-0637(98)00028-4)
- Weber, M.E., Niessen, F., Kuhn, G., and Wiedicke, M., 1997. Calibration and application of marine sedimentary physical properties using a multi-sensor core logger. *Marine Geology*, 136(3–4):151–172.  
[https://doi.org/10.1016/S0025-3227\(96\)00071-0](https://doi.org/10.1016/S0025-3227(96)00071-0)
- Weber, M.E., Raymo, M.E., Peck, V.L., Williams, T., Armbrecht, L.H., Bailey, I., Brachfeld, S.A., Cardillo, F.G., Du, Z., Fauth, G., García, M., Glüder, A., Guitard, M.E., Gutjahr, M., Hemming, S.R., Hernández-Almeida, I., Hoem, F.S., Hwang, J.-H., Iizuka, M., Kato, Y., Kenlee, B., Martos, Y.M., O’Connell, S., Pérez, L.F., Reilly, B.T., Ronge, T.A., Seki, O., Tauxe, L., Tripathi, S., Warnock, J.P., and Zheng, X., 2021a. Expedition 382 methods. *In* Weber, M.E., Raymo, M.E., Peck, V.L., Williams, T., and the Expedition 382 Scientists, *Iceberg Alley and Subantarctic Ice and Ocean Dynamics*. Proceedings of the International Ocean Discovery Program, 382: College Station, TX (International Ocean Discovery Program).  
<https://doi.org/10.14379/iodp.proc.382.102.2021>
- Weber, M.E., Raymo, M.E., Peck, V.L., Williams, T., Armbrecht, L.H., Bailey, I., Brachfeld, S.A., Cardillo, F.G., Du, Z., Fauth, G., García, M., Glüder, A., Guitard, M.E., Gutjahr, M., Hemming, S.R., Hernández-Almeida, I., Hoem, F.S., Hwang, J.-H., Iizuka, M., Kato, Y., Kenlee, B., Martos, Y.M., O’Connell, S., Pérez, L.F., Reilly, B.T., Ronge, T.A., Seki, O., Tauxe, L., Tripathi, S., Warnock, J.P., and Zheng, X., 2021b. Site U1536. *In* Weber, M.E., Raymo, M.E., Peck, V.L., Williams, T., and the Expedition 382 Scientists, *Iceberg Alley and Subantarctic Ice and Ocean Dynamics*. Proceedings of the International Ocean Discovery Program, 382: College Station, TX (International Ocean Discovery Program).  
<https://doi.org/10.14379/iodp.proc.382.105.2021>
- Weber, M.E., Raymo, M.E., Peck, V.L., Williams, T., Armbrecht, L.H., Bailey, I., Brachfeld, S.A., Cardillo, F.G., Du, Z., Fauth, G., García, M., Glüder, A., Guitard, M.E., Gutjahr, M., Hemming, S.R., Hernández-Almeida, I., Hoem, F.S., Hwang, J.-H., Iizuka, M., Kato, Y., Kenlee, B., Martos, Y.M., O’Connell, S., Pérez, L.F., Reilly, B.T., Ronge, T.A., Seki, O., Tauxe, L., Tripathi, S., Warnock, J.P., and Zheng, X., 2021c. Site U1538. *In* Weber, M.E., Raymo, M.E., Peck, V.L., Williams, T., and the Expedition 382 Scientists, *Iceberg Alley and Subantarctic Ice and Ocean Dynamics*. Proceedings of the International Ocean Discovery Program, 382: College Station, TX (International Ocean Discovery Program).  
<https://doi.org/10.14379/iodp.proc.382.107.2021>
- Weber, M.E., Raymo, M.E., Peck, V.L., Williams, T., and the Expedition 382 Scientists, 2021d. Supplementary material,  
<https://doi.org/10.14379/iodp.proc.382supp.2021>. *Supplement to* Weber, M.E., Raymo, M.E., Peck, V.L., Williams, T., and the Expedition 382 Scientists, *Iceberg Alley and Subantarctic Ice and Ocean Dynamics*. Proceedings of the International Ocean Discovery Program, 382: College Station, TX (International Ocean Discovery Program).  
<https://doi.org/10.14379/iodp.proc.382.2021>